UNIVERSITY OF OKLAHOMA

GRADUATE COLLEGE

A COMPARATIVE CONVECTIVE STUDY BETWEEN THE ENSEMBLE KALMAN FILTER AND THE LOCAL PARTICLE FILTER USING THE GRIDPOINT STATISTICAL INTERPOLATION SYSTEM

A THESIS

SUBMITTED TO THE GRADUATE FACULTY

in partial fulfillment of the requirements for the

Degree of

MASTER OF SCIENCE IN METEOROLOGY

By

JOEL MCAULIFFE
Norman, Oklahoma
2020

A COMPARATIVE CONVECTIVE STUDY BETWEEN THE ENSEMBLE KALMAN FILTER AND THE LOCAL PARTICLE FILTER USING THE GRIDPOINT STATISTICAL INTERPOLATION SYSTEM

A THESIS APPROVED FOR THE
SCHOOL OF METEOROLOGY

BY THE COMMITTEE CONSISTING OF

Dr. Louis Wicker (Chair)

Dr. Thomas Jones

Dr. Xuguang Wang

Dr. Steven Cavallo

© Copyright by JOEL MCAULIFFE 2020
All Rights Reserved.

Acknowledgments

My experience in earning a Master's Degree has been far from easy. I have faced and overcame many challenges. I couldn't have succeeded without others, and I would like to use this section of my thesis to give thanks to those who helped. First and foremost, I thank Dr. Louis Wicker and Dr. Thomas Jones for their guidance, patience, and support throughout the project. Since the start, they have dedicated their time to build me up as a better scientist. I am honored to have been selected as their master's student. I am also grateful to my master's committee members, Dr. Steven Cavallo and Dr. Xuguang Wang, for their constructive feedback and challenging me as a student and researcher. Dr. Wang introduced me to data assimilation through her course and inspired me to pursue this field. I would like to thank the School of Meteorology (SoM) faculty and staff for being a fantastic support system. Each professor and staff member believes in the students and only wants to see them succeed. My colleagues and friends had also provided emotional support when times became difficult. I don't know how far I would have made it without my support system in Norman and back home. A special thanks goes to Elisa Murillo, Brian Greene, Briana Lynch, Matt Green, Melanie Schroers, and Amanda Burke. I am grateful for my officemates, Sijie Pan and Larissa Reames, who were explicitly helpful in clarifying small details and minor coding roadblocks. I would also like to thank my family back home. Their love and unwavering support continues to raise my spirits and kept me on track to succeed. Lastly, I want to thank Dr. Jon Poterjoy at the University of Maryland for being directly involved with this project. I appreciate his help and am pleased to have the honor of working with his algorithm.

Table of Contents

Acknowledgments **iv**

List Of Tables **vi**

List Of Figures **vii**

Abstract **xii**

1 Introduction **1**

2 Background **4**

3 Data and Methods **14**
3.1 Mathematical Description of EnKF 14
3.2 Mathematical Description of Local Particle Filter 17
3.3 WoFS Description 19
3.4 Observation Space Statistics 23
3.5 Post-Processing 25
3.6 Verification Methodology 26

4 Results **29**
4.1 1 May 2018 Case 29
4.1.1 Overview 29
4.1.2 Observation Space Diagnostics 32
4.1.3 Mesoscale and Storm-scale Evaluation 36
4.1.4 Objective Verification 47
4.2 2 May 2018 Case 50
4.2.1 Case Description 50
4.2.2 Observation Space Statistics 50
4.2.3 Storm-Scale Forecast Analysis 54
4.2.4 Verification 65
4.3 Dry Bias Diagnostics 67

5 Summary and Future Work **76**

Reference List **79**

List Of Tables

3.1 Adapted from Wheatley et al. (2015), physical parameterization schemes per each forecast ensemble member for each case are presented within the table. Planetary boundary layer (PBL) schemes include the Yonsei University (YSU), Mellor-Yamada-Janić (MYJ), and the Mellor-Yamada-Nakanashi-Niino (MYNN). Shortwave and longwave radiative models include the Dudhia, Rapid Radiative Transfer Model (RRTM) and the Radiative Transfer Model for GCMs (RRTMG). 20
3.2 Horizontal and vertical localization values applied to the listed variables. Horizontal localization in units of kilometers, and scale height units in the vertical direction. 22
3.3 Adapted from Table (1) from Pan (2017), a contingency table for skill score calculations. 28

List Of Figures

1.1 Diagram of the assimilation cycling process. The model is initialized, providing the initial state. The information of the model remains forecast (prior) data until combined with the observation information through data assimilation. The output, known as the posterior, will act as prior information for the next assimilation cycle. 3

2.1 Schematic showing how the Ensemble Kalman Filter works in solution space. Each point in the ovals is a unique solution or observation. Blue dots represent prior members, yellow represents observations, and red represents posterior members. Black arrows represent the propagation of ensemble members through time with the model. Grey arrows represent the data assimilation process whereby the prior forecast solution for each member is updated to the new posterior solution for each member. . . 7

2.2 Adapted from Figure 1 of Yi and Song (2018), a visualization of the assimilation cycling process for the particle filter. The top distribution represents the prior distribution. 1) Sample particles are drawn from the prior distribution, weights are distributed equally per each member. 2) Particles propagate through time, and 3) importance weights are assigned to particles. 4) Resampling occurs, duplicating particles with greater weights and replacing particles with small weights. 5) The resulting distribution of particles represents the posterior distribution which serves as the prior distribution for the next assimilation cycle. . . 9

2.3 Adapted from Figure 3 in Poterjoy 2016. Each dot represents the number of ensemble members (N_e)required for the LPF to produce posterior mean errors smaller than the prior or observations for the simple forecast model having spatial degrees of freedom N_x and N_y Different localization radii r are plotted, as well as a second-degree polynomial fit to the given dots. 11

4.1 Hourly storm evolution for 1 May 2018, from 2000 UTC to 0000 UTC (2200 UTC is omitted). Color plots are the MRMS composite reflectivity and the gray shaded regions depict regions of significant azimuthal shear over the last 5 minutes. The black box roughly outlines region of the Saline/Ottawa EF-3 tornado. 30

4.2 1900 UTC Skew-T diagrams for 1 May 2018 for (a) Topeka, Kansas and (b) Omaha, Nebraska. Red line represents temperature, green line represents dewpoint temperature, and the thin red dashed line represents the parcel path used to compute the CAPE. 31

4.3 Domain of study for 1 May 2018 case. Green square indicates the region of study and blue dots indicate radar locations. The 150-km range rings around each radar depict the maximum range of observations used in the assimilation. 33
4.4 Observation-space diagnostic statistics for assimilated WSR-88D reflectivity for (a) the ensemble Kalman filter and (b) the local particle filter. Red line represents the bias, blue line represents the RMSE, and black line represents the total spread. 34
4.5 Observation-space diagnostic statistics for assimilated WSR-88D radial velocity for (a) the ensemble Kalman filter and (b) the local particle filter. Red line represents the bias, blue line represents the RMSE, and black line represents the total spread. 35
4.6 Observation-space diagnostic statistics for assimilated Oklahoma Mesonet temperature observations for (a) the ensemble Kalman filter and (b) the local particle filter. Red line represents the bias, blue line represents the RMSE, and black line represents the total spread. 37
4.7 Observation-space diagnostic statistics for assimilated Oklahoma Mesonet dewpoint temperature observations for (a) the ensemble Kalman filter and (b) the local particle filter. Red line represents the bias, blue line represents the RMSE, and black line represents the total spread. . . . 38
4.8 Ensemble forecast Skew-T plots of Chanute, Kansas from the 2100 UTC analysis. Left column represents 30 minute forecast soundings and right column represents 1 hour forecasted soundings. Top (Bottom) row is respectively associated with the EnKF (LPF) model. Thick lines resemble the ensemble mean and the thin lines resemble individual ensemble. . 40
4.9 Ensemble forecast Skew-T plots of Kansas City, Kansas initialized from the 2100 UTC analysis. Left column represents thirty minute forecast soundings and right column represents sixty minute forecast soundings. Top (Bottom) row is respectively associated with the EnKF (LPF) model. Thick lines resemble the ensemble mean and the thin lines resemble individual ensemble members. 41
4.10 Forecasted hodograph plots of Chanute Kansas initialized at 2100 UTC. Left column represents thirty minute forecasted hodograph and right column represents sixty minute forecasted hodograph. Top (Bottom) row is respectively associated with the EnKF (LPF) model. Colors represent magnitude of winds at different heights, orange (lowest) and red (highest). 42

4.11 Forecast ensemble spread plots from the Chanute Kansas soundings initialized at 2100 UTC. Mean-layer CAPE is plotted the abscissa and 0-1 km storm-relative helicity is plotted on the ordinate. The left column represents thirty minute forecast spread plots and right column represents sixty minute forecasted spread plots. Top (Bottom) row is respectively associated with the EnKF (LPF) model. Dots represent spread of a given planetary boundary layer scheme. Orange indicates YSU, green indicates MYJ and purple for MYNN. 43
4.12 Top row is MRMS composites of reflectivity and thirty minute aimuthal shear. Center and bottom rows are forecasts of the probability of 2-5 km helicity exceeding 60 m^2s^2 and mean ensemble reflectivity shown with two black contours (25 and 45 dBZ, respectively). Forecasts are initialized at 2100 UTC. Left column represents one hour forecasts, center column represents two hour forecast and right column represents three hour forecasts. Blue dot (e) shows the forecast sounding location of Chanute Kansas and the red dot (e) shows the forecast sounding location of Kansas City. 45
4.13 Plots of total column precipitable water content after 10 minutes of integration initialized at 2200 UTC for 1 May 2018. Left image resembles forecasted precipitable water plots of the EnKF model and right represents the LPF model. 46
4.14 Plots of mean layer CAPE after 10 minutes of integration initialized at 2200 UTC for 1 May 2018. Left image resembles forecasted precipitable water plots of EnKF model, and right represents the LPF model. . . . 47
4.15 Performance diagrams of 30/60/120 minute forecasts for the 1 May case starting at 2100 UTC for reflectivity objects using the methodology from Skinner et al. (2018). Green dots represent the EnKF experiment and orange dots represent the LPF. Large dots are the ensemble mean, and small dots are the scores of the individual members. 49
4.16 Domain of study for 2 May 2018 case. Green square indicates the region of study and blue dots indicate radar locations. The 150-km range rings around each radar depict the maximum range of observations used in the assimilation. 51
4.17 Hourly storm evolution for 2 May 2018, from 1900 UTC to 2200 UTC. Color plots are the MRMS composite reflectivity and the gray shaded regions depict regions of significant azimuthal shear during previous 5 minutes. 52
4.18 1900 UTC Skew-T diagram at Norman, Oklahoma for 2 May 2018. Red line represents temperature, green line represents dewpoint temperature, and thin red dashed line represents the parcel path used to compute the CAPE. 53

4.19 Observation-space diagnostic statistics for assimilated WSR-88D reflectivity for (a) the ensemble Kalman filter and (b) the local particle filter. Red line represents the bias, blue line represents the RMSE, and black line represents the total spread. 55
4.20 Observation-space diagnostic statistics for assimilated WSR-88D radial wind observations for (a) the ensemble Kalman filter and (b) the local particle filter. Red line represents the bias, blue line represents the RMSE, and black line represents the total spread. 56
4.21 Observation-space diagnostic statistics for assimilated GOES-16 cloud water path observations for (a) the ensemble Kalman filter and (b) the local particle filter. Red line represents the bias, blue line represents the RMSE, and black line represents the total spread. 57
4.22 Skew-T plots of the forecast Norman, Oklahoma sounding initialized at 2100 UTC. Left column represents thirty minute forecast soundings and right column represents one hour forecasted soundings. Top (Bottom) row is respectively associated with the EnKF (LPF) model. Thick lines resemble the ensemble mean and the thin lines resemble individual ensemble members. 58
4.23 Forecasted hodograph plots of Norman, Oklahoma initialized at 2100 UTC. Left column represents thirty minute forecasted hodograph and right column represents one hour forecasted hodograph. Top (Bottom) row is respectively associated with the EnKF (LPF) model. Colors represent magnitude of winds at different heights, orange (lowest) and red (highest). 60
4.24 Forecast ensemble spread plots of Norman, Oklahoma soundings initialized at 2100 UTC. Mean-layer CAPE is plotted the abscissa and 0-1 km storm-relative helicity is plotted on the ordinate. The top (Bottom) row is respectively associated with the EnKF (LPF) model. Dots represent spread of a given planetary boundary layer scheme. Orange indicates YSU, green indicates MYJ and purple for MYNN. 61
4.25 Top row is MRMS composites of reflectivity and thirty minute azimuthal shear. Center and bottom rows are forecasts of the probability of 2 – 5 km helicity exceeding 60 m^2s^2 and mean ensemble reflectivity shown with two black contours (25 and 45 dBZ, respectively). Forecasts are initialized at 2100 UTC. Left column represents one hour forecasts, center represents two hour forecasts and right column represents three hour forecasts. Blue dot is the Norman OK sounding location. 63
4.26 Plots of total column precipitable water content after 10 minutes of integration initialized at 2200 UTC for 2 May 2018. Left image resembles forecasted precipitable water plots of EnKF model, and right represents the LPF model. 64

4.27 Plots of mean layer CAPE after 10 minutes of integration initialized at 2200 UTC for 2 May 2018. Left image resembles forecasted precipitable water plots of EnKF model, and right represents the LPF model. . . . 65
4.28 Performance diagrams of 30/60/120 minute forecasts for the 2 May case starting at 2100 UTC for reflectivity objects using the methodology from Skinner et al. (2018). Green dots represent the EnKF model and orange dots represent the LPF. Large dots are the ensemble mean, and small dots are the scores of the individual members. 66
4.29 Panel of precipitable water information at 1800 UTC. Left column contains plots of precipitable water content (in) after observations are assimilated. Right column displays the increments of precipitable water after assimilation. 70
4.30 Panel of precipitable water information at 1830 UTC. Left column contains plots of precipitable water content (in) after observations are assimilated. Right column displays the increments of precipitable water after assimilation. 71
4.31 Panel of precipitable water information at 1900 UTC. Left column contains plots of precipitable water content (in) after observations are assimilated. Right column displays the increments of precipitable water after assimilation. 72
4.32 Panel of precipitable water information at 1800 UTC centered at Clinton, OK. Top row contains overlaid histograms of precipitable water content (in) before assimilation (red) and after assimilation (blue). Bottom row displays histograms of the increments in precipitable water content after assimilation. 73
4.33 Panel of precipitable water information at 1830 UTC centered at Clinton, OK. Top row contains overlaid histograms of precipitable water content (in) before assimilation (red) and after assimilation (blue). Bottom row displays histograms of the increments in precipitable water content after assimilation. 74
4.34 Panel of precipitable water information at 1900 UTC centered at Clinton, OK. Top row contains overlaid histograms of precipitable water content (in) before assimilation (red) and after assimilation (blue). Bottom row displays histograms of the increments in precipitable water content after assimilation. 75

Abstract

The localized particle filter (LPF) is a recent advance in ensemble data assimilation for numerical weather prediction. Derived from the original particle filter used for highly nonlinear state variables, the LPF incorporates a localization function to reduce the influence of distant observations. Particle filters are an effective data assimilation method for higher order variables and is widely used in the geoscience community for its ability to maintain nonlinear properties through cycling. The LPF has been proven to be successful in idealized cases. This work seeks to evaluate the LPF for real-data convective-scale weather predictions.

This study compares the performance of storm-scale analyses and predictions generated from the LPF method compared to the classic ensemble Kalman filter (EnKF) which is commonly used in atmospheric data assimilation weather prediction systems. Since the LPF does not contain many of the underlying assumptions that the EnKF does, it is hypothesized that the LPF may be useful for convective-scale data assimilation in generating accurate analyses and forecasts. This research project uses NSSL's Warn-on-Forecast System (WoFS) to compare the performance of the two data assimilation schemes.

The use of the LPF provides some benefits over the EnKF when producing smaller posterior and prior root-mean-square-errors (RMSE) for non-Gaussian variables, such as reflectivity. More linear variables, such as radial wind, are assimilated at a similar efficacy. Ensemble members of the LPF create more spread of dewpoint temperature than the EnKF within the mid-levels of the atmosphere. Overall, the LPF tends to create a dry bias within the environment, leading to premature decay of the storms.

Chapter 1

Introduction

Numerical weather prediction (NWP) is an important tool used by forecasters to predict severe weather events, such as tornados, flash flooding, hail, and severe winds. Based on Doppler weather radar observations, current tornado warning lead time range between 10-13 minutes annually (Brooks, 2004; Stensrud et al., 2009). The National Severe Storms Laboratory (NSSL) Warn on Forecast (WoF) project goal is to increase warning lead times using numerical model output in a probabilistic manner. Increasing warning lead times will enable various stakeholders in local communities to prepare appropriately (Stensrud et al., 2009, 2013). For example, emergency managers, police, and fire departments could use warnings with larger lead times to move resources needed for disaster recovery out of the tornado's path. Hospitals and nursing homes require at least 30 minutes of warning to move patients away from windows. Residents of areas prone to flooding can also evacuate earlier when an increase in the flash flood risk is predicted. The goal of WoF is to increase warning lead times from its current 10 minutes to hour(s) via NWP using a probabilistic approach to the warning process.

After almost 30 years using Doppler radar information, the evidence is fairly clear that human forecasters using radar observations are unable to provide more than 15 minutes of warning for tornadoes (Bieringer and Ray, 1996; Brooks, 2004), particularly warnings for the first tornado threats of the day or in mesoscale environments which are challenging (e.g. low instability with high shear or high instability with low shear). The highly nonlinear characteristics of these mesoscale systems and storm cells suggest

that NWP is essential in determining the time and location of these high-risk events beyond the Doppler radar warning time limit. To use NWP for storm-scale weather prediction, an accurate model and an accurate initial state are needed. This requires the use of a process called data assimilation (Fig. 1.1[1]) which optimally combines model predictions and observations to estimate the true state of the atmosphere (Bouttier and Courtier, 2002; Wang et al., 2000; Kalnay, 2003). This method of correcting the model incorporates a wide variety of surface observations, e.g. surface automated surface observing systems (ASOS) measurements and state-run mesonet data (Fujita et al., 2007; Sobash and Stensrud, 2015); data from aloft such as rawinsonde or commercial aircraft data (Cardinali et al., 2003), radar data (Snyder and Zhang, 2003), and satellite data (Miyoshi and Kunii, 2012; Jones et al., 2015, 2016). All of these measurements are irregularly distributed in space and time. A storm-scale prediction system requires frequent intermittent use of the available observations and a data assimilation algorithm to generate the new initial conditions for forecasts on an hourly or sub-hourly basis.

The purpose of this research is to determine if the storm-scale forecasts and analyses improve from implementing a new data assimilation algorithm, called the local particle filter (Poterjoy et al., 2019), when compared to the traditional ensemble Kalman filter that has already shown success in predicting high-impact weather. NSSL's Warn on Forecast System (WoFS) will be used as the control forecast for the experiments. Wheatley et al. (2015) and Skinner et al. (2018) describe the forecast and verification system used in WoFS. Poterjoy et al. (2017) demonstrated that the local particle filter has been proven to outperform the EnKF in assimilating hydrometeor variables for idealized convective cases, and the ability to provide accurate probabilistic analyses of a squall line within the observing system simulation experiment (OSSE). Ensemble forecasts using the LPF analyses are more accurate than the ensemble adjustment

[1]https://kiss.caltech.edu/workshops/carbon/presentations/liu.pdf

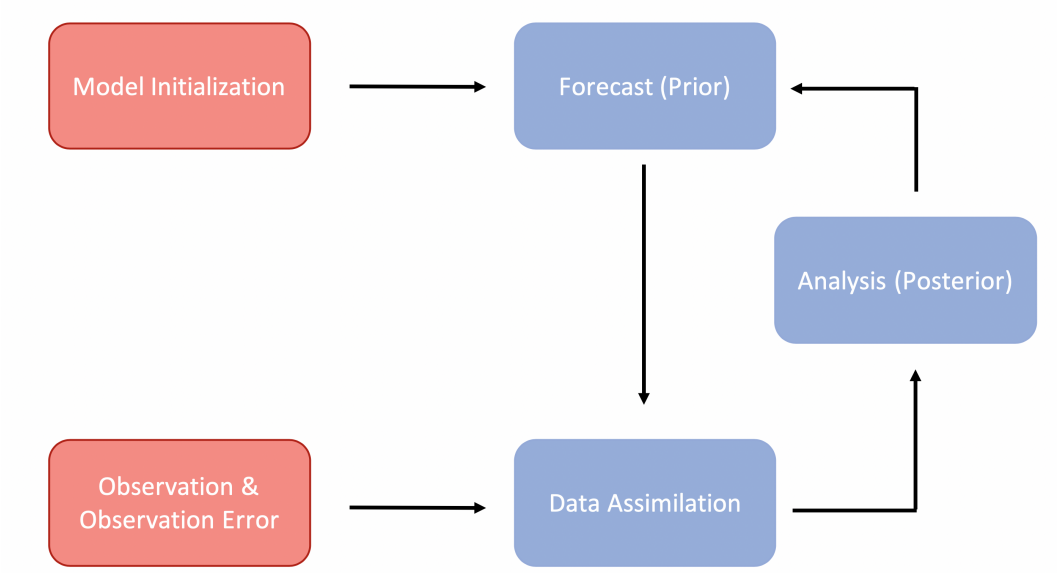

Figure 1.1: Diagram of the assimilation cycling process. The model is initialized, providing the initial state. The information of the model remains forecast (prior) data until combined with the observation information through data assimilation. The output, known as the posterior, will act as prior information for the next assimilation cycle.

Kalman filter after 10-20 minutes of integration (EAKF; Anderson 2001). In Poterjoy et al. (2019), the local particle filter is implemented into the WoFS, and tested for the tornadic event of 24 May 2016 in western Kansas. Results conclude that the local particle filter analyses, after tuning the configurations, did produce lower root-mean square differences than the EAKF for radar winds. Based off this research, it is hypothesized that the local particle filter could help improve real-world applications such as the WoFS. The ensemble Kalman filter used in WoFS will be replaced by the local particle filter and a series of retrospective cases are run to assess its performance relative to the current ensemble Kalman filter data assimilation method which is widely used in atmospheric prediction systems (Houtekamer et al., 2005; Tong, 2006; Zhang et al., 2009; Hamill et al., 2011).

Chapter 2

Background

The ensemble Kalman filter (EnKF; Evensen 1994) was developed from the classical Kalman filter theory (Kalman, 1960) and Monte Carlo estimation methods. Monte Carlo methods use repeated random sampling techniques to make estimations of unknown parameters, while the Kalman filter was developed as a best least squares estimator for linear ordinary differential equations that needed to incorporate observational inputs (Kalman and Bucy, 1961). This assimilation method has been implemented in various geophysical systems (Evensen, 1994; Houtekamer and Mitchell, 1998), most commonly for oceanic and atmospheric systems.

The original Kalman filter (Kalman, 1960) was a method developed to estimate the true state of a system using a simple linear evolution equation and observations of location and speed from a noisy set of measurements, such as those obtained from a missile or rocket guidance system. The Kalman method is optimal in the sense that for an unbiased model and a series of observations, it always finds the "best" estimate (e.g. minimizes the mean square error) of the state of the system. For linear low-rank dynamic systems it is an efficient method of data assimilation. Because it is low-rank and the evolution equations are linear, the covariances and state variable information can be both propagated using linear models. Unfortunately, most dynamical systems are nonlinear in nature; thus, a linear approximation of the model generates errors for these systems. The extended Kalman filter (Jazwinski, 1970) reduces these additional errors, as it does not require a linear model when propagating information between

assimilation cycles. However, the covariance model requires a linearized propagation model and forward operator. The forward operator converts the background fields into observation space and often is nonlinear. Linearizing the propagation model requires multivariate Taylor series expansions, which has proved to be computationally expensive (Evensen, 1994).

The EnKF is a Monte Carlo implementation of the extended Kalman filter. There are two types of EnKF algorithms: stochastic and deterministic. In the stochastic approach, the EnKF applies additive noise to observations per each ensemble member, removing non-Gaussian higher moments created from nonlinear error growth (Houtekamer and Zhang, 2016). Deterministic filters do not perturb observations; instead, the optimal Kalman gain is used to obtain the analysis error covariance. Overall, the EnKF is more cost-efficient than the extended Kalman filter, as the system is less sensitive to nonlinear forward operators. There are advantages and disadvantages to each of the two EnKF methods. The stochastic approach has the ability to identify major sources of error (i.e. data assimilation and model error) and can appropriately sample the errors in the Monte Carlo framework. However it is computationally expensive and often requires a large ensemble to maintain accuracy. The objective of deterministic filters, including the ensemble square root filter (EnSRF; Whitaker and Hamill 2002) used in this study, is to obtain the best analysis estimate using a minimal ensemble size. The benefit of using the EnSRF in contrast to a stochastic filter is the reduction of computational cost.

There are a number of assumptions needed to be satisfied for EnKF to obtain the optimal analysis. First, one needs accurate knowledge of the forecast errors in the ensemble forecasts and the observation errors associated with each observational platform. These errors are assumed to have Gaussian statistics, are unbiased, and uncorrelated (Evensen, 1994). Large ensembles have better statistics, but due to the cost

of integrating the forecast model in NWP applications, the use of very large ensemble sizes is prohibitive in most cases. However, numerous experiments and tests show that an ensemble size of O(100) is sufficient for realistic atmospheric background statistics (Houtekamer and Zhang, 2016). In order to represent non-Gaussian probability distributions functions, an ensemble size of O(1000) is needed (Miyoshi et al., 2014). The computational cost and data storage for such a large ensemble size for full physics NWP model prohibits this approach.

The procedure for the ensemble Kalman filter is shown in Fig. 2.1. Ensemble members are initialized with the model and propagated through time with the numerical model until an observation is spotted. The prior members are optimally combined with the observation to output posterior members, which will then propagate forward in time to then serve as prior members for the next assimilation cycle.

Many studies have incorporated the EnKF into their convective-scale work (Zhang et al., 2004; Jung et al., 2008; Jones et al., 2015; Snook et al., 2015; Sobash and Stensrud, 2015; Wheatley et al., 2015; Zhang et al., 2018). Dowell et al. (2011) studied how radar observations affect forecasts and analyses for the May 8, 2003, Oklahoma City event. The experiment showed the assimilated radar observations lead to rapid development of storms when compared to the control model run (Snyder and Zhang, 2003). Yussouf et al. (2015) tested the ability of a multiscale ensemble-based assimilation system using the Advanced Weather and Research Forecasting (WRF-ARW) model and the Data Assimilation Research Testbed (DART; Anderson et al. 2009) assimilation system. In this case, the DART assimilation system uses the ensemble adjustment Kalman filter, a deterministic version of the EnKF. Observations, including Doppler radar and radial velocity, were assimilated to evaluate analyses and forecasts of the April 27, 2011, severe weather outbreak in Alabama. The study concluded that the

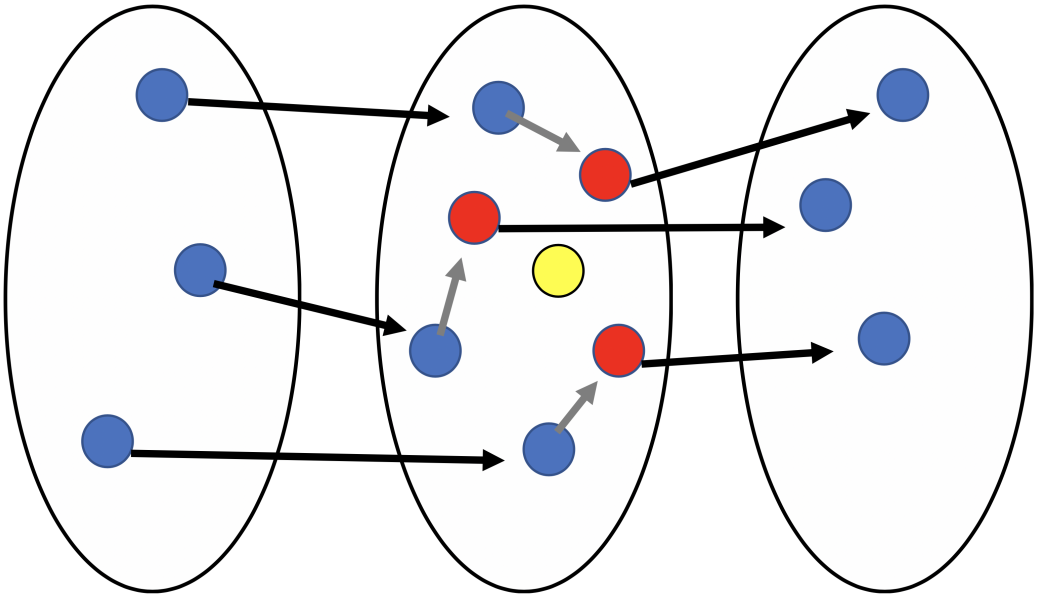

Figure 2.1: Schematic showing how the Ensemble Kalman Filter works in solution space. Each point in the ovals is a unique solution or observation. Blue dots represent prior members, yellow represents observations, and red represents posterior members. Black arrows represent the propagation of ensemble members through time with the model. Grey arrows represent the data assimilation process whereby the prior forecast solution for each member is updated to the new posterior solution for each member.

ensembles located the observed storms and preserved the supercell structures during the first-hour forecasts.

Though the EnKF has proven to be a successful algorithm for atmospheric prediction, it can still benefit from computational improvements. First, the quality of the analysis is limited to ensemble size and resolution. However, the computational cost to increase these characteristics restricts the ability to do so. In order for the background covariance matrix to have a full rank, the model must be integrated of $O(10^8)$ at each coordinate (Houtekamer and Zhang, 2016). Since the optimal assimilation with the EnKF system requires Nens O(100), the typical Nobs $N(10^6)$ will be projected onto a reduced space, Nens – 1 (Lorenc, 2003). This is known as the rank problem. This problem is caused by the large decrease in degrees of freedom and leads to spurious

correlations. To mitigate this issue, a localization function is applied to the background error covariance to reduce the influence of distant spurious correlations. Another disadvantage of the EnKF are the assumption of linearity and Gaussian error statistics. Since the model does not require linearization between assimilation cycles, nonlinearities are accounted for in the ensemble forecast. However, nonlinear distributions of state variables' perturbation statistics are often smoothed out during the analysis step due to the underlying Gaussian assumptions.

The EnKF is widely used and has clearly led to improved numerical weather prediction, however there are known limitations associated with the assumption that the forecast background and observational errors should have Gaussian statistics. To address these issues, many investigators have tried to relax the Gaussian assumption by developing what are called particle filters (hereafter, PF; Carpenter et al. 2000; Doucet et al. 2001; Chen 2003; van Leeuwen 2009). Particle filters are known to be useful for data assimilation within systems having non-Gaussian statistics.

Ensemble members in the PF are called particles. Posterior weights are applied to the particles, reflecting the likelihood of observations given to each member (Poterjoy, 2016). A resulting posterior probability density function is obtained, and this posterior distribution is independent of the prior error distribution. Those particles with lesser weights will be removed and resampled, whereas the particles associated with a greater likelihood relative to the observations will be duplicated using the bootstrap filter. See Fig. 2.2 for an illustration (Gordon et al., 1993).

Ensemble size constrains the performance of the particle filter. In theory, the ensemble size should increase exponentially with dimension size (Snyder et al., 2008). Particle solutions are known to collapse onto one solution if the ensemble size is too small; this is also known as filter degeneracy (Bengtsson et al., 2008). Typical PF sizes,

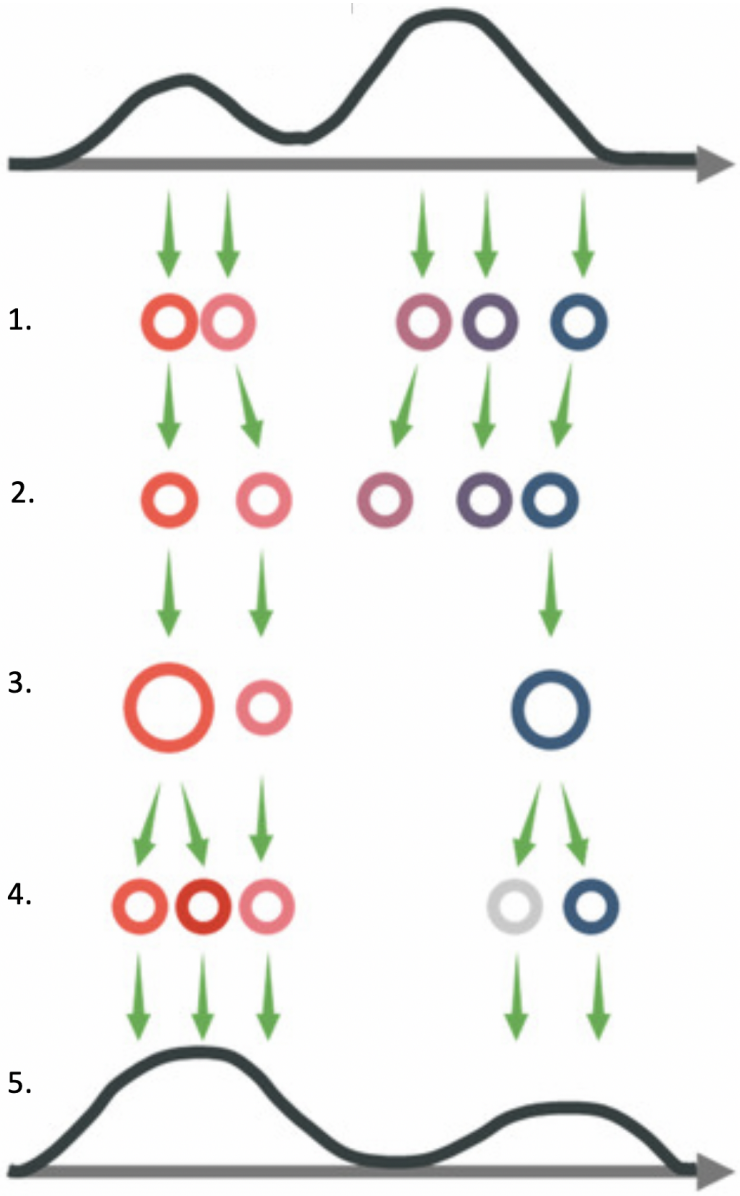

Figure 2.2: Adapted from Figure 1 of Yi and Song (2018), a visualization of the assimilation cycling process for the particle filter. The top distribution represents the prior distribution. 1) Sample particles are drawn from the prior distribution, weights are distributed equally per each member. 2) Particles propagate through time, and 3) importance weights are assigned to particles. 4) Resampling occurs, duplicating particles with greater weights and replacing particles with small weights. 5) The resulting distribution of particles represents the posterior distribution which serves as the prior distribution for the next assimilation cycle.

even for lower-rank nonlinear systems require an ensemble size of O(1000). Particle filters also suffer from sampling error since its difficult to adjust prior particles toward the true state if a particle is outside the span of the distribution. Therefore, practical assimilation using particle filters for high dimensional systems such as numerical weather prediction are far more costly than conventional EnKF.

The local particle filter (LPF; Poterjoy 2016) utilizes a localization weighting function, differentiating this filter from the original particle filter. The main goal of localization is to reduce the influence of distant observations. When a localization radius is given, observations beyond that distance will have no impact. For the local particle filter, localization is used to prevent filter degeneracy as it removes the required exponential increase of ensemble size with dimension size. Fig. 2.3 derived from Poterjoy (2016) shows how a decrease in localization radius will result in a reduced number of required particles to produce posterior mean RMSE smaller than the prior. This happens because the weights depend on fewer observations when smaller radii are used in the spatial localization.

The LPF approaches the resampling process differently due to the complexity of the localization function. At each timestep, observations are processed serially while repeatedly updating the particles. This method entails a two-step process. First, a bootstrap filter is applied for each observation. Resampled particles are merged with prior particles to create samples of the first and second-order moments. The goal of this step is to maintain sampled particles near the observations, thus adjusting the updated particles towards the observations. The last step is adjusting the new particles using the kernel density distribution mapping (McGinnis et al., 2015) approach. This process adjusts new particles to be consistent with the probabilities given by the posterior weights.

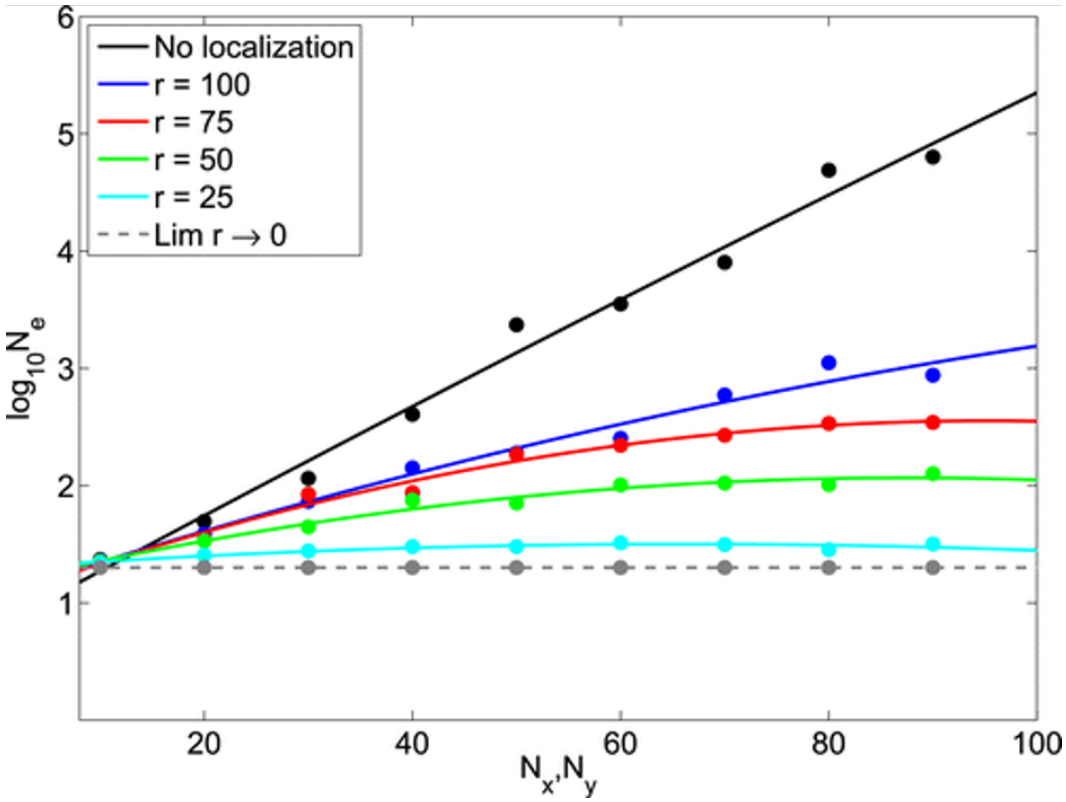

Figure 2.3: Adapted from Figure 3 in Poterjoy 2016. Each dot represents the number of ensemble members (N_e)required for the LPF to produce posterior mean errors smaller than the prior or observations for the simple forecast model having spatial degrees of freedom N_x and N_y Different localization radii r are plotted, as well as a second-degree polynomial fit to the given dots.

The LPF data assimilation method has been previously tested in several low- and high-dimensional systems. Poterjoy (2016) applied the local particle filter to the 40-variable Lorenz (1995) model. The goal of this experiment was to test the localization and particle update scheme, and the performance of the LPF was compared to the EAKF within the NCAR DART software package (Anderson et al., 2009). Results showed that the LPF required at least five particles to prevent particle collapse for this 10,000-cycle data assimilation experiment. Moreover, the LPF generated lower prior mean RMSEs than the DART EAKF. Lastly, the LPF outperforms the EAKF in regions of dense, nonlinear observations. Poterjoy et al. (2017) also examined the performance of the LPF at the convective scale in comparison to the EAKF using an observing systems simulation experiment. After generating a truth solution with the Advanced Regional Weather Research and Forecast model (i.e., the WRF-ARW model), one hundred particles were used in the LPF to assimilate observations from simulated radar reflectivity and velocity. Though near-Gaussian prior error distributions led to lower posterior RMSEs from the EAKF, the LPF developed accurate analyses of the squall-line simulations. However, forecasts of the LPF were more accurate than the EAKF after 10-20 mins. The greatest benefit from using the LPF is updating nonlinear hydrometeor state variables. More time between assimilation cycles is shown to be more efficient for LPF since the errors are able to grow more nonlinearly through time.

Though the discussion above explains the benefits of the local particle filter for idealized cases, the benefits from using the local particle filter remains uncertain for full-physics numerical weather prediction, such as convective storm prediction using Doppler radar data.

This research compares the performance of the LPF to the current WoFS EnKF system. The local particle filter has only been tested in limited ways at the convective

scale (Poterjoy et al., 2017, 2019). Based off the previous idealized studies, the LPF has great potential to produce accurate forecasts and analyses for this realtime case study. As such, the research will focus on the following question: How will the forecasts and analyses of the local particle filter compare to the ensemble Kalman filter for convective systems?

Here the local particle filter is used as the data assimilation algorithm in the WoFS in place of the EnKF. A statistical analysis is performed on the assimilation diagnostics to determine the efficacy of the assimilation system. A comparative analysis between the two systems is done to assess the differences in the mesoscale environment, followed by the verification of storm objects between observations and model forecasts.

Chapter 2 covers the data assimilation cycling information, post-processing, and verification of this study. Chapter 3 discusses research results, and the conclusion and discussion are presented in Chapter 4.

Chapter 3

Data and Methods

3.1 Mathematical Description of EnKF

Houtekamer and Zhang (2016) outlines the theoretical formulation of the EnKF. Common terminology includes background ensemble information $\boldsymbol{x^b}(t)$ at a given timestep, the observation value $\boldsymbol{y}$, updated analysis $\boldsymbol{x^a}(t)$ at a given timestep, the Kalman gain $\boldsymbol{K}$, the observation error covariance matrix $\boldsymbol{R}$, and the background error covariance $\boldsymbol{P^b}$. In our system, the background information is the model forecast prior to assimilation, and the resulting analysis is the posterior after assimilation. The analysis is propagated using the forecast model to the next assimilation time. Calculating the analysis requires knowledge of the observations and the background ensemble forecast, such that:

$$\boldsymbol{x^a}(t) = \boldsymbol{x^b}(t) + \boldsymbol{K}[\boldsymbol{y} - \boldsymbol{H}\boldsymbol{x^b}(t)]. \tag{3.1}$$

$\boldsymbol{H}$ is the forward operator which translates the model's state vector into observation space. The Kalman gain is a weighting function for the innovation term ($\boldsymbol{y}$–$\boldsymbol{H}\boldsymbol{x^b}(t)$), and can be solved as,

$$\boldsymbol{K} = \boldsymbol{P^b}\boldsymbol{H^T}(\boldsymbol{H}\boldsymbol{P^b}\boldsymbol{H^T} + \boldsymbol{R})^{-1}. \tag{3.2}$$

The Kalman gain is a function which weights the background errors ($\boldsymbol{HP^bH^T}$) and observation errors ($\boldsymbol{R}$). The Kalman gain provides the optimal weight to be applied to the innovation, [$\boldsymbol{y}$–$\boldsymbol{Hx^b}(t)$]. If the observations errors are smaller than the background errors from the ensemble, the Kalman gain will be larger, adjusting the analysis toward the observations. If the observation errors are larger than the background errors from the ensemble, the impact of the observations is smaller on the ensemble. If the background errors become too small, the Kalman gain will have little impact. This is often called filter divergence and indicates that the assimilation essentially has failed.

The analysis state vector is propagated with the nonlinear model $\boldsymbol{M}$ until it reaches the next timestep, which these ensemble members will then serve as prior members before the assimilation cycle:

$$\boldsymbol{x^b}(t) = \boldsymbol{M}[\boldsymbol{x^a}(t-1)]. \tag{3.3}$$

For the EnSRF, an ensemble system of the state vector is created. Eqs. 1.1 can be written to solve for the ensemble mean:

$$\bar{\boldsymbol{x}}^{\boldsymbol{a}}(t) = \bar{\boldsymbol{x}}^{\boldsymbol{b}}(t) + \boldsymbol{K}[y - \boldsymbol{H}\bar{\boldsymbol{x}}^{\boldsymbol{b}}(t)]. \tag{3.4}$$

The analysis of each ensemble member can be solved for by combining the mean and the member's perturbation from the mean:

$$x_k^a = \bar{x}^a + x_k'^a. \tag{3.5}$$

$x_k'^a$ is the ensemble member's perturbation and can be solved as:

$$x'^{a}_{k} = x'^{b}_{k} - \widetilde{\boldsymbol{K}}[\boldsymbol{H}(x^{b}_{k} - \bar{\boldsymbol{x}}^{\boldsymbol{b}})]. \tag{3.6}$$

$\widetilde{\boldsymbol{K}}$ is the reduced Kalman gain, used to update the perturbations and provide a true estimate of the analysis error covariance matrix. This modified weighting matrix ensures a more accurate representation of the ensemble spread and can be calculated:

$$\widetilde{\boldsymbol{K}} = \left(1 + \sqrt{\frac{\boldsymbol{R}}{\boldsymbol{H}\boldsymbol{P}^{\boldsymbol{b}}\boldsymbol{H}^{\boldsymbol{T}} + \boldsymbol{R}}}\right)^{-1} \boldsymbol{K}. \tag{3.7}$$

When updated deviations with the reduced Kalman gain, the analysis-error covariance will be equal to:

$$\boldsymbol{P}^{\boldsymbol{a}} = (I - \boldsymbol{K}\boldsymbol{H})\boldsymbol{P}^{\boldsymbol{b}}, \tag{3.8}$$

where I represents the identity matrix. $\widetilde{\boldsymbol{K}}$ involves the square root of measurement error-covariance matrices, which basically infers a Monte Carlo implementation of a square root filter (Maybeck, 1979). Observations are assimilated serially since the operating cost of calculating matrix square roots in batches is too large.

3.2 Mathematical Description of Local Particle Filter

Poterjoy (2016) outlines the mathematical theory behind the local particle filter. Terminology includes state vector $\boldsymbol{x}$ of length N_x, observation vector $\boldsymbol{y}$ of length N_y, the true state $\boldsymbol{x^t}$ of length N_x, and the forward operator $\boldsymbol{H}$. A relationship is established between the observation and the true state in which:

$$\boldsymbol{y} = \boldsymbol{H}(x^t) + \varepsilon, \tag{3.9}$$

where ε represents the observation error. The posterior particles are updated using Bayes' theorem:

$$p(\boldsymbol{x}|\boldsymbol{y}) = \frac{p(\boldsymbol{y}|\boldsymbol{x})p(\boldsymbol{x})}{\int p(\boldsymbol{y}|\boldsymbol{x})p(\boldsymbol{x})dx}. \tag{3.10}$$

To do so, there must be accurate knowledge of the prior distribution of particles $p(\boldsymbol{x})$ and the likelihood distribution of the observations given the prior distribution $p(\boldsymbol{y}|\boldsymbol{x})$. The resulting distribution represents the posterior probability density function, which will then serve as the prior distribution for the next period of ensemble integration. To obtain $p(\boldsymbol{x}|\boldsymbol{y})$, a Monte Carlo approximation is applied to $p(\boldsymbol{x})$ and $p(\boldsymbol{y}|\boldsymbol{x})$. Therefore:

$$p(\boldsymbol{x}) \approx \frac{1}{N_e} \sum_{n=1}^{N_e} \delta(\boldsymbol{x} - \boldsymbol{x}_n). \tag{3.11}$$

Normalized weights, $\boldsymbol{w}_n/\boldsymbol{W}$, are used to reflect the likelihood distribution, $p(\boldsymbol{y}|\boldsymbol{x})$, such that:

$$\boldsymbol{w}_n = p(\boldsymbol{y}|\boldsymbol{x}_n) \tag{3.12}$$

$$\boldsymbol{W} = \sum_{k=1}^{N_e} w_k \tag{3.13}$$

These weights are normalized to estimate the integral in the denominator in eq. 3.10. The combination of the weights and the approximation of the prior distribution, eq. 3.11, result in the calculation of the posterior distribution $p(\boldsymbol{x}|\boldsymbol{y})$:

$$p(\boldsymbol{x}|\boldsymbol{y}) \approx \frac{1}{N_e} \sum_{n=1}^{N_e} \frac{w_n}{W} \delta(\boldsymbol{x} - \boldsymbol{x}_n). \tag{3.14}$$

Weights from the previous filtering time are assumed to be equal if new particles are resampled from the posterior for each filtering time. The distribution of sampled particles are conditioned on the current observations, which will later be chosen as the prior probability density (Doucet et al., 2001).

Similar to the EnKF, localization is applied to the particle filter to prevent destabilization and filter degeneracy. In this case, the original weights are extended from scalars to vectors, w_n, to form a N_x by N_e weighting matrix. The vectors reflect the local influence of observations on the estimated posterior distribution. The jth element of w_n per each ensemble member can be calculated as:

$$\omega_(n, j) = [p(y|x_{n,j}) - 1]\, l[y, x_j, r] + 1. \tag{3.15}$$

The localization function, $l[y, x_j, r]$, is maximum when the distance between y and x_j is 0, and decreases as the distance between y and x_j increases. The benefit of using Eq. 1.15 is the ability to spatially localize information.

3.3 WoFS Description

The NSSL Experimental Warn-on-Forecast System for ensembles is used for this project. WoFS uses the ARW version 3.8.1 with 36 members for cycled analysis system. These ensemble members are integrated forward in time using the ARW model until it reaches the next assimilation cycle, which occurs every 15 minutes from 1800 UTC to 0300 UTC. Observations assimilated include the Oklahoma state mesonet surface observations and the WSR-88D radar reflectivity and radial velocity. The national network of Automated Surface Observing Stations (ASOS) are assimilated once per hour. Storms generally begin around 2000 UTC in both cases and the data assimilation cycling is started at 1800 UTC to allow enough time to spin up the model from the initial conditions.

The WRF model grid is nested within the domain of the experimental High-Resolution Rapid Refresh Ensemble (HRRRE; Dowell et al. 2016). HRRRE provides the boundary and initial conditions along the perimeter of the region. The domain encompasses a 750 km by 750 km regional grid with 3 km horizontal gridspacing. To create and maintain ensemble spread, multiphysics planetary boundary layer schemes (MYNN, MYA, and YSU) and radiation transfer schemes (Dudhia, Rapid Radiative Transfer Model (RRTM), the Radiative Transfer Model for GCMs (RRTMG)) are used. A single microphysics scheme is used: the NSSL double moment cloud microphysics (Mansell et al., 2010). This scheme is used for all members to provide unbiased reflectivity fields for the radar analysis. Refer to Table 1 for more details.

The gridpoint statistical interpolation (GSI; Wu et al. 2002) system provides the forward operator code to convert the model state variables into the observational priors used in the data assimilation. An EnKF component (Whitaker et al., 2008) then assimilates the data and generates observation diagnostics based on the prior and

Member	PBL	Shortwave Radiation	Longwave Radiation
1	YSU	Dudhia	RRTM
2	YSU	RRTMG	RRTMG
3	MYJ	Dudhia	RRTM
4	MYJ	RRTMG	RRTMG
5	MYNN	Dudhia	RRTM
6	MYNN	RRTMG	RRTMG
7	YSU	Dudhia	RRTM
8	YSU	RRTMG	RRTMG
9	MYJ	Dudhia	RRTM
10	MYJ	RRTMG	RRTMG
11	MYNN	Dudhia	RRTM
12	MYNN	RRTMG	RRTMG
13	YSU	Dudhia	RRTM
14	YSU	RRTMG	RRTMG
15	MYJ	Dudhia	RRTM
16	MYJ	RRTMG	RRTMG
17	MYNN	Dudhia	RRTM
18	MYNN	RRTMG	RRTMG

Table 3.1: Adapted from Wheatley et al. (2015), physical parameterization schemes per each forecast ensemble member for each case are presented within the table. Planetary boundary layer (PBL) schemes include the Yonsei University (YSU), Mellor-Yamada-Janić (MYJ), and the Mellor-Yamada-Nakanashi-Niino (MYNN). Shortwave and longwave radiative models include the Dudhia, Rapid Radiative Transfer Model (RRTM) and the Radiative Transfer Model for GCMs (RRTMG).

posterior information, updating the forecast files with new information. Calculations of bias (observation – model), prior and posterior spread, and root mean square error (RMSE) are also computed at each cycle. These diagnostics provide an estimate of the efficacy of the assimilation process. Continuously cycling the available observations should help drive the ensemble toward the observed true state, which is represented by lower RMSE and bias in the time series of prior and posterior diagnostics.

Localization is aimed to ameliorate sampling error of small ensembles by reducing the influence of distant observations (Anderson, 2007), limiting the generation spurious correlations. For this study, localization is applied in the horizontal and vertical direction, and these distances vary depending on the observed source. Table 2 displays the localization radii given for each variable. Furthermore, the additive-noise method proposed in Dowell and Wicker (2009) is applied to maintain ensemble spread within convective storms throughout extensive periods of data assimilation. This method has previously been proven to preserve the ensemble spread within the convective storm while the environment remained relatively undisturbed. With this technique, one selects which model variables are perturbed and the magnitude of the perturbations.

Forecasts use the first 18 ensemble members which reduces the computational cost by half while providing sufficient ensemble spread for probabilistic forecasts. The forecast ensemble is first generated at 1900 UTC, and three-hour forecasts are run for this study. Output from the forecast ensemble provide a variety of environmental and severe parameters and fields. Forecast composite reflectivity and 2-5 km layer updraft helicity is used to determine the intensity of the initiated storms when compared to the Multi-Radar/Multi-Sensor (MRMS; Lakshmanan et al. 2007) composite of reflectivity and azimuthal shear. The MRMS fields are used as proxies in the objective evaluation described below. Swaths of updraft helicity in the 0-2 km layer can also be used

Variable	Horizontal Localization (km)	Vertical Localization (scale height)
Radial Wind (rw)	14.0	0.60
Reflectivity (dBZ)	14.0	0.60
Temperature (T)	45.0	0.68
Dewpoint (T_d)	45.0	0.64
Water Vapor Mixing Ratio (q_v)	45.0	0.64
u-Directional Wind (u)	45.0	0.64
v-Directional Wind (v)	45.0	0.64
Surface Pressure (ps)	45.0	0.64

Table 3.2: Horizontal and vertical localization values applied to the listed variables. Horizontal localization in units of kilometers, and scale height units in the vertical direction.

to detect low-level mesocyclones. These near-surface mesocyclones indicate tornado potential (Trapp et al., 2005). However, due to the radar horizon, it is difficult to objectively use azimuthal shear at the lowest tilts to verify the low-level updraft helicity in the forecasts, therefore objective verification in this study focuses on mid-level updraft helicity. Composite reflectivity is used to measure the skill of the forecasts across all thunderstorms (Skinner et al., 2018). All radar derived verification fields are created by the MRMS system.

3.4 Observation Space Statistics

Observation-space diagnostic statistics (Dowell and Wicker, 2009) are used to analyze the ability of each data assimilation system to create analyses that closely match the observed surface, radar, and other assimilated mesoscale information. Analyses are created every 15 minutes over a nine hour period for the prediction system from 1800 – 0300 UTC. These statistical calculations include bias (observation – model), root-mean square error, total ensemble spread (standard deviation), and consistency ratio (Yussouf et al., 2015). Respectively, the following equations from Yussouf et al. (2013) are used to calculate the aforementioned statistical computations:

$$d = \{y - Hx^b\} or \{y - Hx^a\}, \tag{3.16}$$

where d signifies the bias term also known as the innovation.

$$\text{RMSE} = \sqrt{\langle d^2 \rangle} \tag{3.17}$$

The brackets containing the innovation term signifies the average over all observations. RMSE measures the overall fit of the forecasts and analyses to the observations (Yussouf et al., 2013). The total ensemble spread is used to provide the degree of spread of the ensemble, and is calculated as:

$$\text{total spread} = \sqrt{\sigma_{obs}^2 + \left\langle \frac{1}{N-1} \sum_{n=1}^{N} \left[Hx_n - \overline{Hx} \right]^2 \right\rangle} \tag{3.18}$$

$$\text{consistency ratio} = \frac{\sigma_{obs}^2 + \left\langle \frac{1}{N-1} \sum_{n=1}^{N} \left[Hx_n - \overline{Hx} \right]^2 \right\rangle}{\langle d^2 \rangle} \tag{3.19}$$

σ^2_{obs} is the standard deviation of the observation error. The consistency ratio ranges between 0 and 1, which larger ratios indicate a better fit between the ensemble variance and the forecast error variance relative to the observation errors.

3.5 Post-Processing

Post-processing the forecast ensemble generates a number of quantities that describe either the mesoscale environment or the individual storm characteristics. For the environmental parameters (e.g., CAPE, 0-1 km shear, storm-relative helicity) the mean of the ensemble is used. For storm-scale characteristics, both the ensemble means, ensemble probabilities, and paths of storm-relative helicity are used (e.g., composite reflectivity, updraft magnitude, and low-level and mid-level updraft helicity).

Diagnosed environmental variables include ensemble mean surface and mid-level winds, mixing ratio, surface pressure, temperature, and storm-scale attributes such as the convective available potential energy (CAPE) and convective inhibition (CIN). Ensemble means are computed from the 18 forecast members.

Since individual storms can vary in location and timing across each member of the forecast ensemble, probabilistic information is generated via neighborhood ensemble probabilities (Theis et al., 2005). These neighborhood probabilities represent the percentage of grid points from each member forecast that exceeds a threshold (Johnson and Wang, 2012). For the WoFS system, grid points located within 9 km are used to represent a "hit" for a threshold value (e.g., values such as 45 dbz for a reflectivity core, 60 m2 s2 for updraft helicity). The percentage of members meeting these values represent the uncertainty of forecast (Skinner et al., 2018).

3.6 Verification Methodology

Skinner et al. (2018) describes the verification methodology used by the Warn-on-Forecast project. Due to the lack of detailed observations at convective scales, storm-scale verification must create proxies from the model state and the available observations in order to objectively measure differences between the model forecasts and observed weather. Proxies are generated from WSR-88D data using output from the MRMS system. Available MRMS composite reflectivity observations are selected for verification of WoFS composite reflectivity forecasts. Mesocyclone forecasts are verified using rotation tracks, a product of MRMS azimuthal wind shear data (Miller et al., 2013).

Object identification in composite reflectivity or rotation tracks defines thresholds that can be used to distinguish the object's boundaries (Skinner et al., 2018). Complications arise when defining these thresholds due to inherently different nature of the model forecasts versus the observed fields. Model and observation objects have different thresholds. Skinner et al. (2018) describes a method of calibrating model-derived objects versus observational objects. Once calibrated, the total interest score (Davis et al., 2009) evaluates how close the forecasted object's attribute (e.g. composite reflectivity objects or updraft helicity tracks) matches the verification attribute (e.g. observed reflectivity and rotation tracks), spatially and temporally. This score is computed for each pair of forecasts and observed objects and is calculated as:

$$\mathrm{TI} = \left\{ \frac{\left[\frac{cd_{max}-cd}{cd_{max}}\right] + \left[\frac{md_{max}-md}{md_{max}}\right]}{2} \right\} \left[\frac{t_{max}-t}{t_{max}}\right] \tag{3.20}$$

Where **t** is the time difference between an object pair, **md** is the minimum difference between the pair, and **cd** is the centroid difference between the pair. The maximum threshold difference is noted with the max subscript, 40 km for centroid and minimum

distances and 25 min for time placement. A forecast and observed object are identified as a matched pair if their total interest score is greater than 0.2. The forecast object with the highest total interest score will be paired with the observed, which is necessary when multiple forecast objects are paired with the observed. Forecast and verification object pairs can be classified as:

Hits: the forecast object matches the observed object

False alarms: The forecast object is present, however it is unmatched with an observed object

Misses: The verification object is present, however it is unmatched with a forecast object

The classifications above are a qualitative way of analyzing object pairs. Contingency tables (see Table 3) are a qualitative verification method, and uses the classifications to solve for these calculations:

$$POD = \frac{A}{A+C} \tag{3.21}$$

$$FAR = \frac{B}{A+B} \tag{3.22}$$

$$BIAS = \frac{A+B}{A+C} \tag{3.23}$$

$$CSI = \frac{A}{A+B+C} \tag{3.24}$$

where A indicates "hits", B indicates "false alarms", and C are "misses". Unfortunately, calculations based on the contingency table are deterministic and do not fully sample the probabilistic nature of this type of ensemble-based forecast.

Contingency Table		Event Observed	
		Yes	No
Event Forecast	Yes	A (HIT)	B (FA)
	No	C (MISS)	D (N/A)

Table 3.3: Adapted from Table (1) from Pan (2017), a contingency table for skill score calculations.

Performance diagrams are produced to compare the forecast's performance between the LPF and the EnKF through time, focusing on the probability of detection and the success ratio for storm-scale rotation and reflectivity greater than 45 dBZ. The success ratio is the complement of the false alarm rate. Diagrams are created for 30 minute, 1 hour, and 2 hour forecasts.

Chapter 4

Results

4.1 1 May 2018 Case

4.1.1 Overview

The first case tested is the 1 May 2018 tornadic event in northern Kansas and southern Nebraska during which twenty-one tornadoes were reported. The majority of the tornado and hail reports occurred from storms in north-central Kansas and along the Kansas-Nebraska border. These storms that originated in Kansas and Nebraska (Fig. 4.1) and eventually propagated into Iowa later that evening, leading to additional severe hail and wind reports. In the Nebraska region, scattered storms developed adjacent and southeast of the stationary front with hail being the dominant severe hazard.

Figure 4.2 displays observed 1900 UTC soundings and hodographs of Topeka, Kansas, and Omaha, Nebraska. The environment has veering moderate vertical wind shear and enhanced low-level moisture and large CAPE. NOAA's Storm Prediction Center's outlook for north-central KS was a moderate risk of severe weather with a 10% or greater chance for EF2 or greater tornadoes.

Northeastern Kansas experienced the more severe weather. Multiple supercells initiated in a north-south line west and southwest of Salina, Kansas around 2000 UTC. These storms generated approximately nine tornadoes. The largest tornado formed

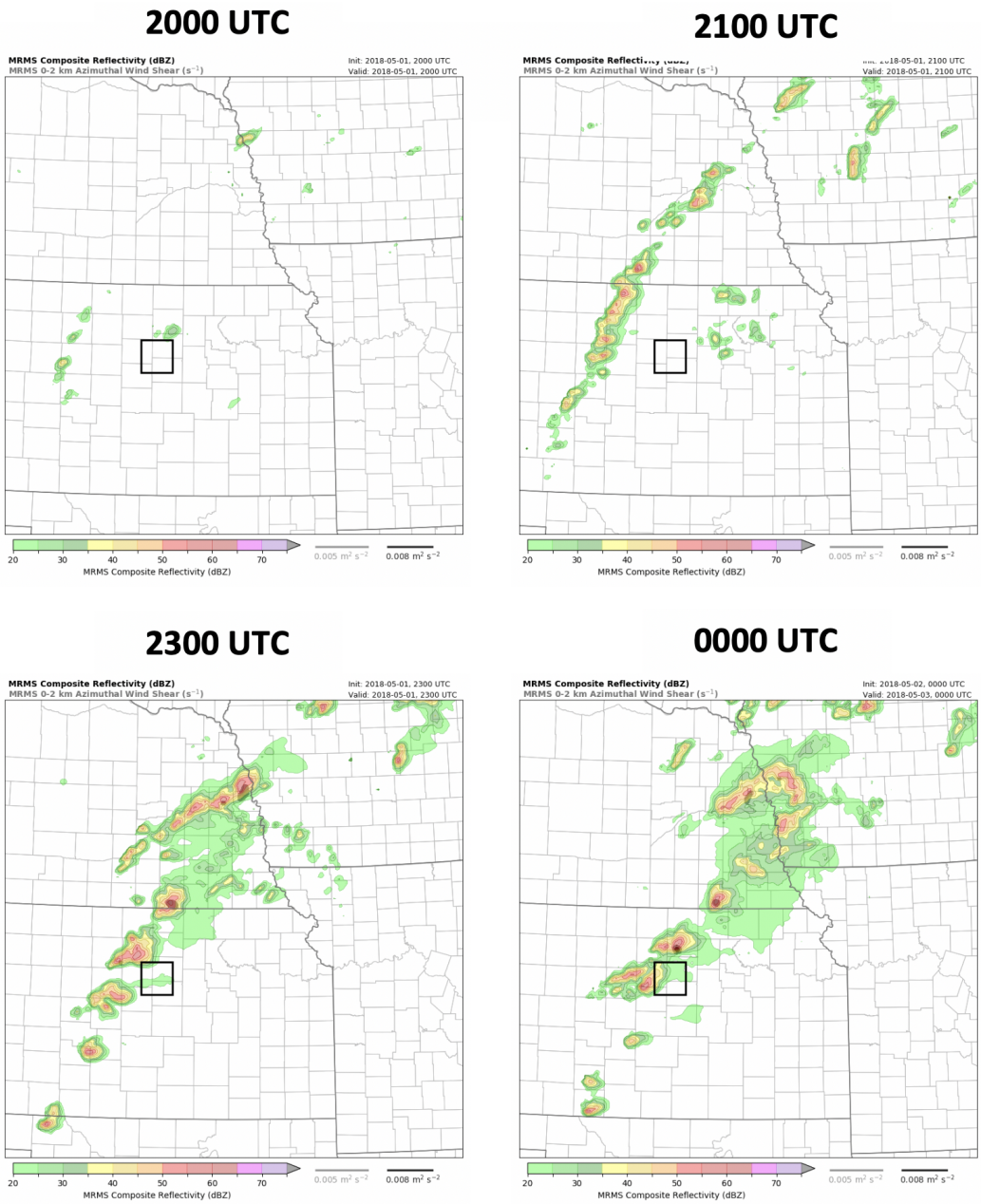

Figure 4.1: Hourly storm evolution for 1 May 2018, from 2000 UTC to 0000 UTC (2200 UTC is omitted). Color plots are the MRMS composite reflectivity and the gray shaded regions depict regions of significant azimuthal shear over the last 5 minutes. The black box roughly outlines region of the Saline/Ottawa EF-3 tornado.

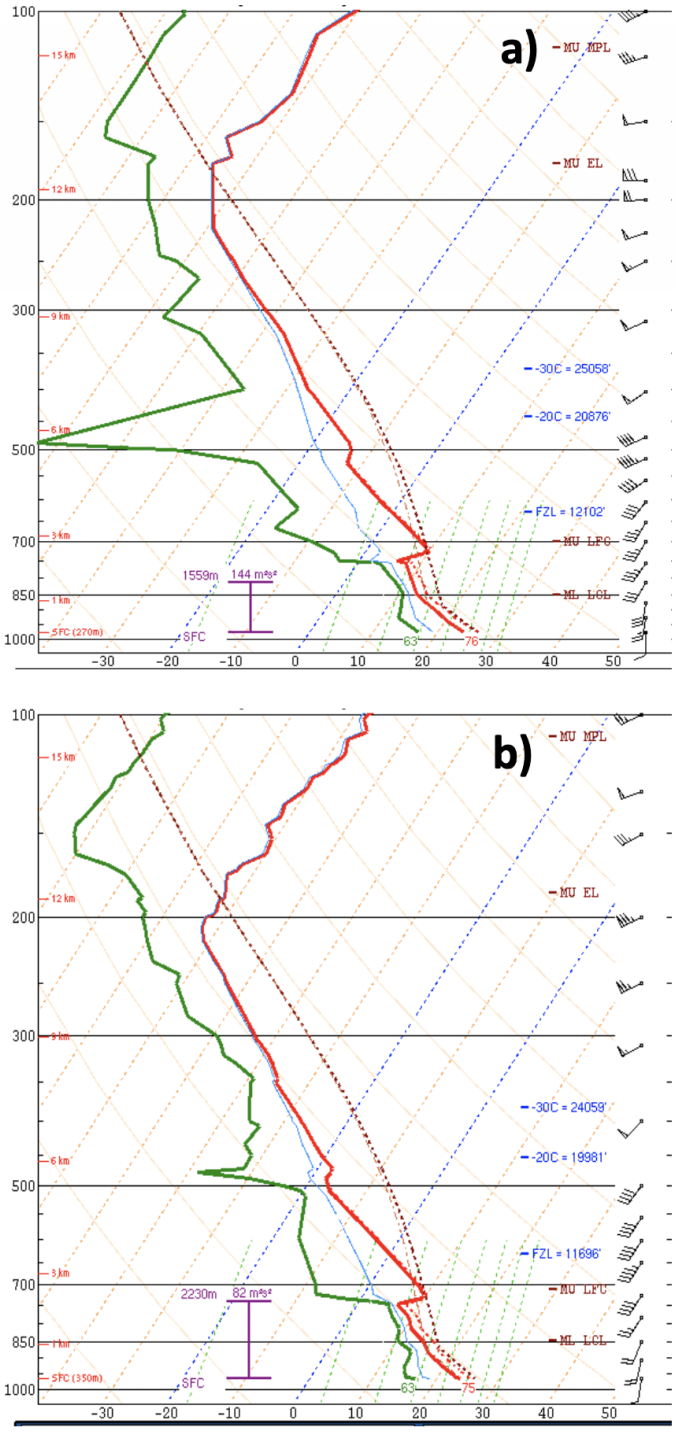

Figure 4.2: 1900 UTC Skew-T diagrams for 1 May 2018 for (a) Topeka, Kansas and (b) Omaha, Nebraska. Red line represents temperature, green line represents dewpoint temperature, and the thin red dashed line represents the parcel path used to compute the CAPE.

around 0049 UTC and occurred in Saline County and tracked northeast through Ottawa County. This tornado was rated an EF-3 with a path length of 14.5 miles. Very large hail was also observed, up to the size of softballs were associated with this supercell.

The green box in Figure 4.3 highlights the domain used by WoFS for the analyses and forecasts, spanning eat to west from eastern Kansas to central Iowa, and spanning north to south from. Oklahoma-Kansas border to the Nebraska-South Dakota border. Both the EnKF and LPF systems proceed as follows: the assimilation starts at 1800 UTC, and observations are assimilated every 15 minutes. Three-hour 18 member forecasts are initialized starting at 2000 UTC and continue every thirty minutes until 0000 UTC. Observation-space diagnostics are discussed next.

4.1.2 Observation Space Diagnostics

Diagnostics from the assimilation of WSR-88D reflectivity and radial wind observations are shown in Figures 4.4 and 4.5, respectively. The positive bias in Figure 4.4 indicates that reflectivity is underpredicted by both experiments throughout the assimilation timeframe. Bias increases for the first ten cycles of assimilation during the period of model spin-up. Convective initiation occurred around 2000 UTC (Fig. 4.1), thus numerous clear air reflectivity observations are assimilated for the first two hours to prevent storms from initiating too quickly in the model. Bias and RMSE are smaller in the EnKF than the LPF between 2000-2100 UTC. This might suggest that the EnKF is spinning the storms up faster than the LPF. Towards the end of the cycling, the local particle filter displays slightly lower posterior RMSE values than the EnKF, suggesting the LPF forecasts have somewhat smaller error growth possibly from an improved analysis. Since radial velocity has more linear error statistics than reflectivity, it is expected that the two filters will assimilate the radial wind at a comparable efficacy.

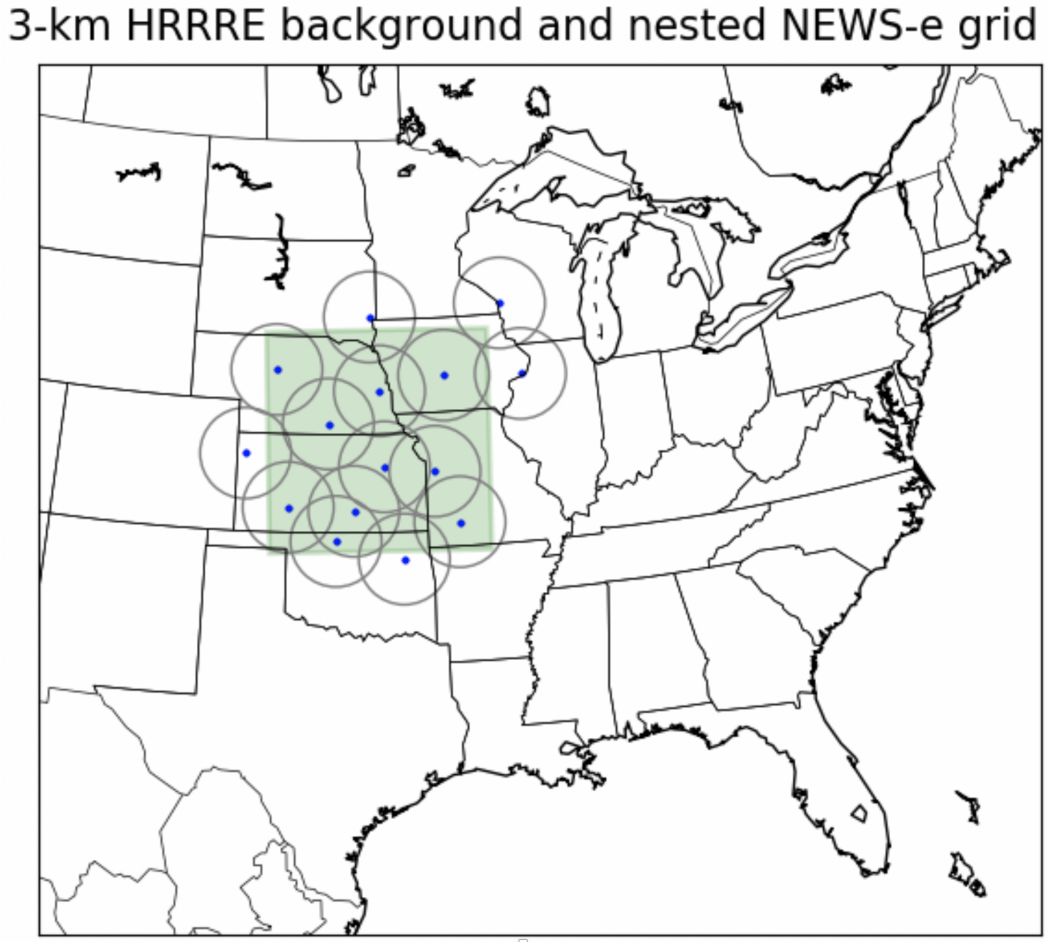

Figure 4.3: Domain of study for 1 May 2018 case. Green square indicates the region of study and blue dots indicate radar locations. The 150-km range rings around each radar depict the maximum range of observations used in the assimilation.

Figure 4.5 shows that there are no distinct differences of RMSE and bias between the two experiments.

Surface observations are included into the assimilation as well. Since the ASOS data is only assimilated every hour and mesonet data every 15 minutes, error statistics will focus only on mesonet data. As the focus for this case is centered around Kansas and Nebraska and the mesonet network is comprised of surface observing stations distributed across Oklahoma, the greatest influence of the observation network occurs

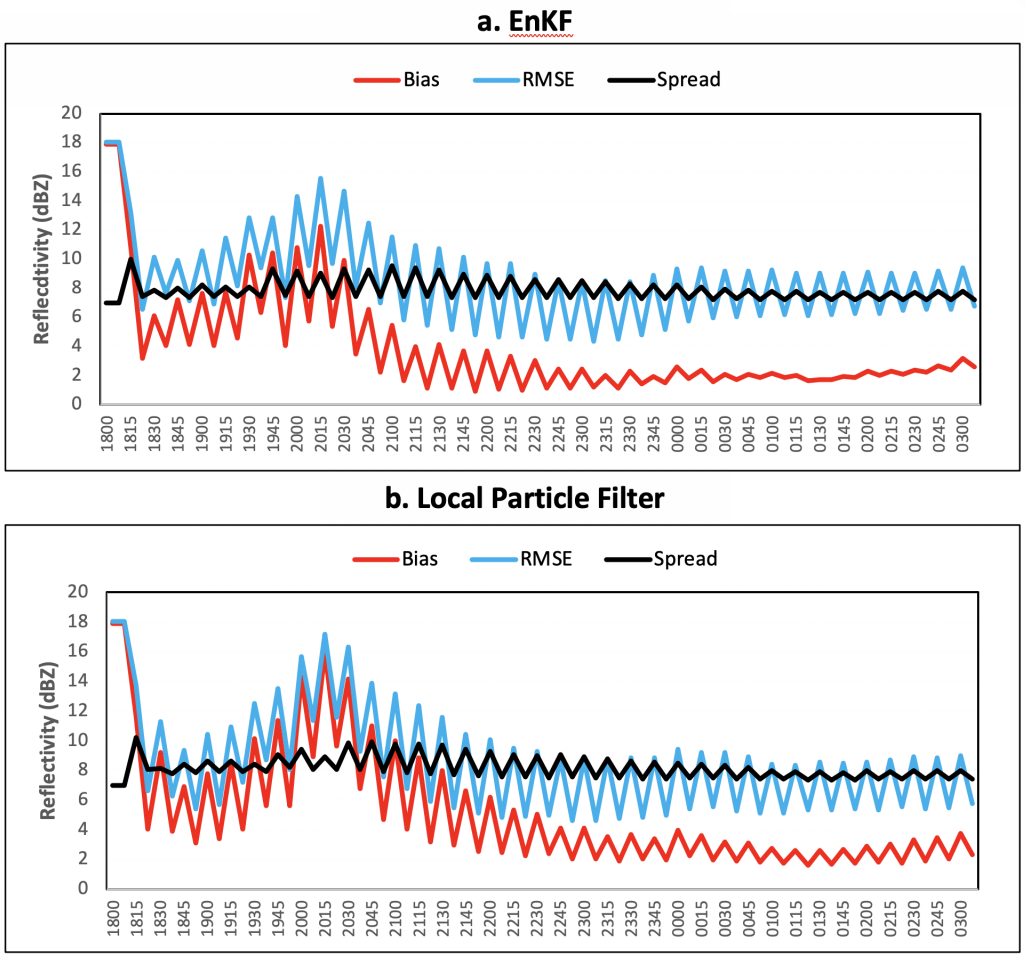

Figure 4.4: Observation-space diagnostic statistics for assimilated WSR-88D reflectivity for (a) the ensemble Kalman filter and (b) the local particle filter. Red line represents the bias, blue line represents the RMSE, and black line represents the total spread.

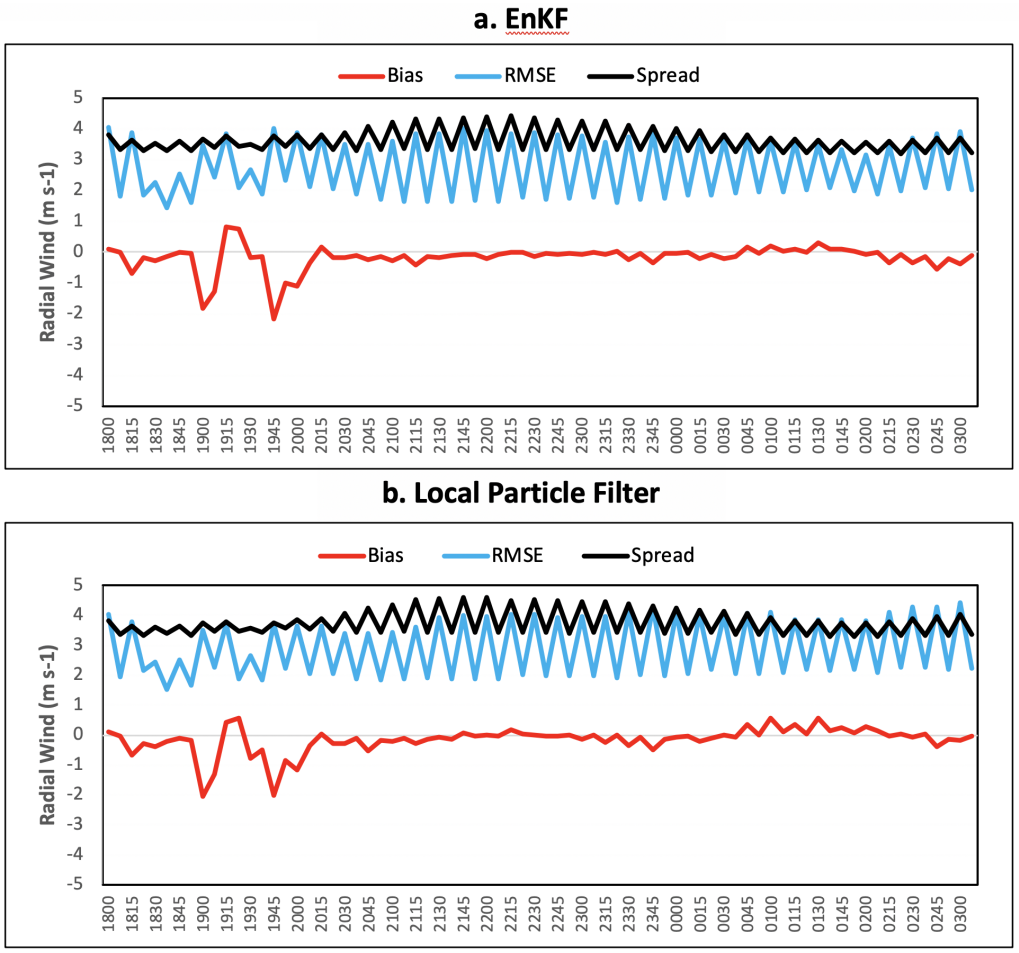

Figure 4.5: Observation-space diagnostic statistics for assimilated WSR-88D radial velocity for (a) the ensemble Kalman filter and (b) the local particle filter. Red line represents the bias, blue line represents the RMSE, and black line represents the total spread.

in the southern portion of the domain. As time progresses, the environmental properties in the south will be advected northward, leading to changes in the environment in close proximity of the storms. Similar to the assimilation of radial wind, temperature and dewpoint temperature (Figs. 4.6 and 4.7) show minimal differences in RMSE between the EnKF and the LPF experiments. Both experiments show a cool temperature bias during most of the analysis cycling. The source of this bias could not be determined, but could be possibly caused by the lateral boundary conditions being supplied by the HRRRE models near the WoFS southern boundary.

4.1.3 Mesoscale and Storm-scale Evaluation

The SHARPpy python program (Blumberg et al., 2017) is used to generate forecast soundings at a given location from the model forecasts to compare with nearby observed soundings. Ensemble forecast soundings are generated from the 2100 UTC forecasts to estimate the inflow environment ahead of the storms from the EnKF and the LPF. For 1 May Chanute, KS is chosen (Fig. 15). Chanute is located in a region of drying that occurs over time in LPF analysis, whereas the EnKF does not depict this drying. Figure 4.8 displays 30 minute (Fig. 4.8 a,c) and one hour (Fig. 4.8 b,d) ensemble forecast soundings from both experiments for Chanute. Overall, both experiments demonstrate minimal variability between ensemble members within the temperature sounding. The temperature ensemble mean for the thirty-minute forecast sounding is essentially the same between the two experiments, yet the ensemble mean in temperature is one degree greater in the LPF than the EnKF one-hour. The LPF dewpoint temperature also has a greater spread. There is increased spread at low-levels, but even larger spread is seen in the mid- and upper-levels of the atmosphere for both experiments, most prominently between 400 and 700 hPa. In general, the LPF generates more thermodynamic profile

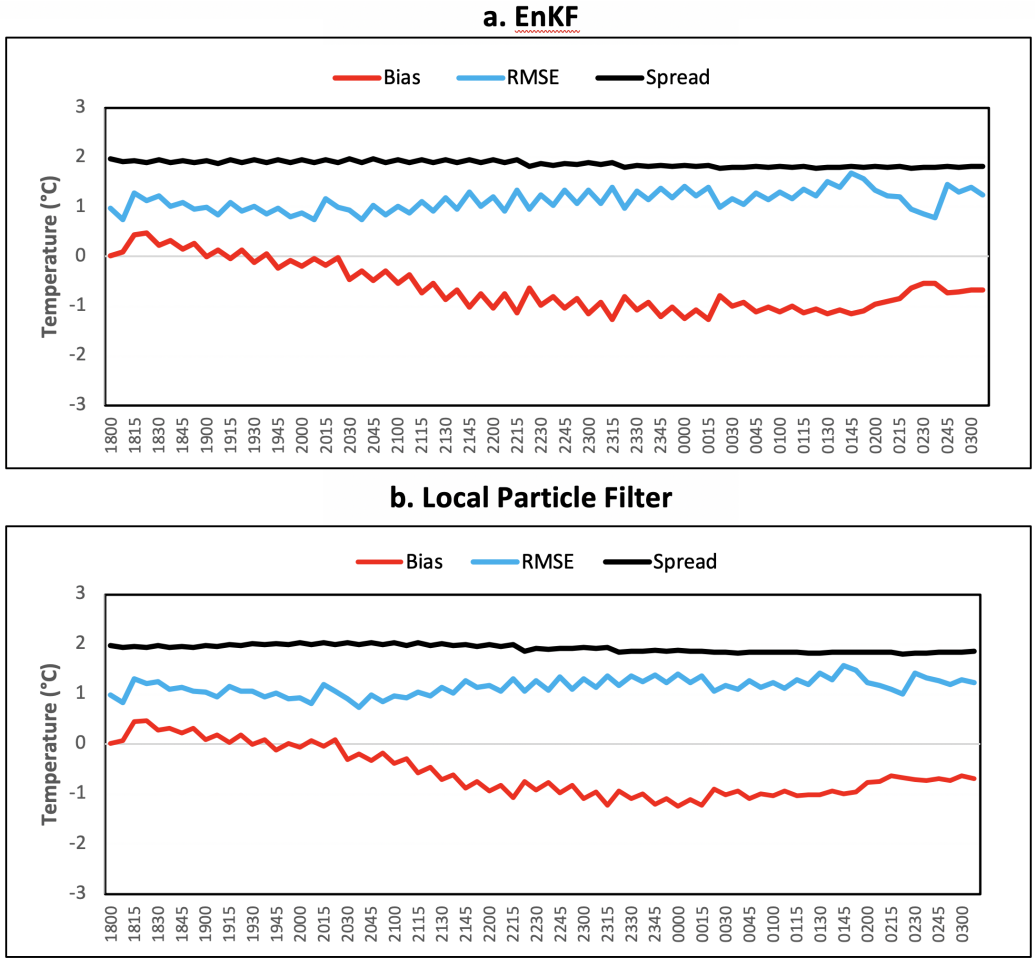

Figure 4.6: Observation-space diagnostic statistics for assimilated Oklahoma Mesonet temperature observations for (a) the ensemble Kalman filter and (b) the local particle filter. Red line represents the bias, blue line represents the RMSE, and black line represents the total spread.

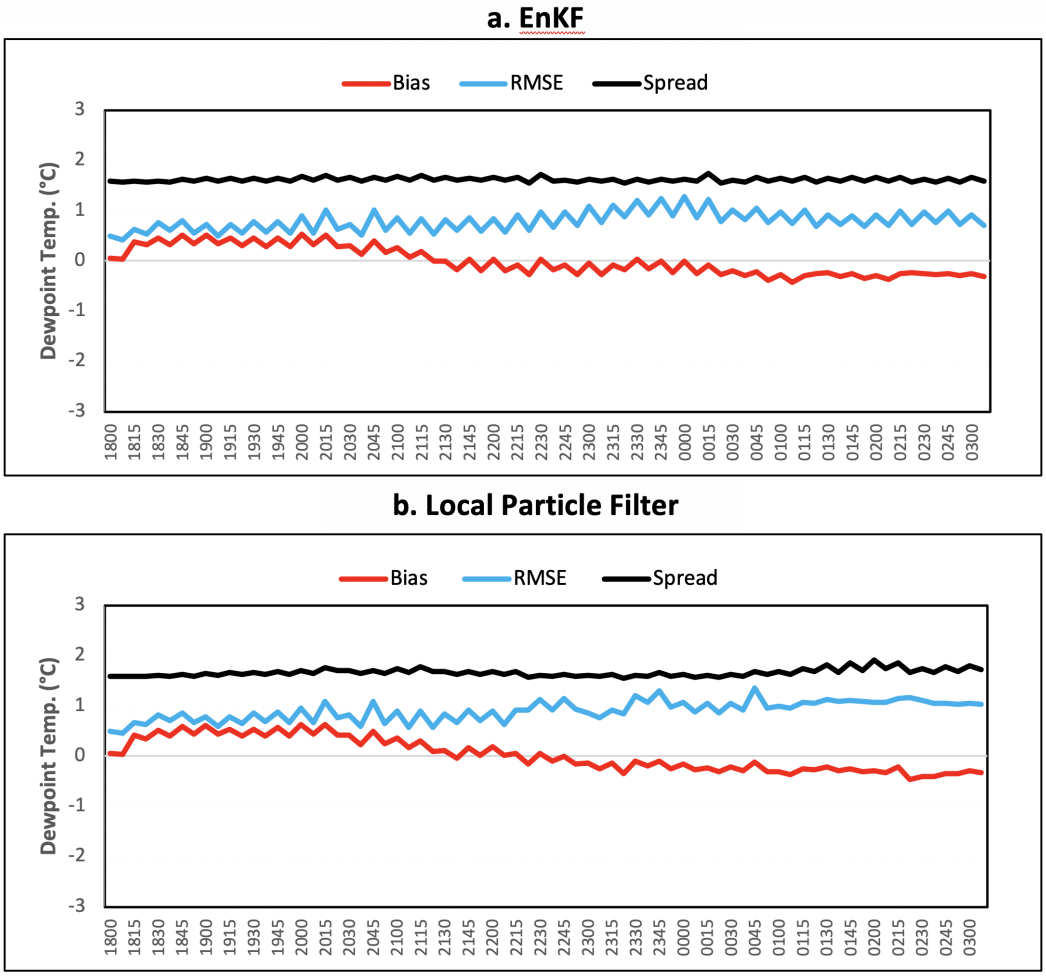

Figure 4.7: Observation-space diagnostic statistics for assimilated Oklahoma Mesonet dewpoint temperature observations for (a) the ensemble Kalman filter and (b) the local particle filter. Red line represents the bias, blue line represents the RMSE, and black line represents the total spread.

spread than the EnKF. Kansas City soundings (Fig. 4.9) portray similar features as Chanute. Though the mean temperatures are the same in both experiments, the LPF dewpoint temperature is one degree cooler than the EnKF, further suggesting that a somewhat drier environment is analyzed and forecasted by the LPF experiment.

Hodographs (Fig. 4.10) generated from the SHARPpy software represent the vertical profile of the environmental horizontal wind. Optimal supercell development requires strong, veering vertical shear. The veering shape of the hodograph is similar between the two experiments, providing enough shear to support severe thunderstorms. More variability between ensemble members is evident with the LPF (Fig. 4.10 c-d) model when compared to the EnKF (Fig. 4.10 a-b), especially above the boundary layer into the mid-levels. Figure 4.11 plots the mean-layer CAPE from the ensemble thermodynamic profiles in Figure 4.8 against the 0-1 km Storm Relative Helicity (SRH) displayed in Figure 4.10. Mean layer CAPE measures the average instability in the lowest 100 hPA of the atmosphere, and SRH measures the amount of low-level wind shear available for tornadogenesis. The output is colored by the PBL scheme used in each member. In general, there is a larger spread in CAPE (mostly toward smaller values) associated with the LPF experiment, with somewhat larger spread in the vertical shear, particularly associated with members using the MYJ scheme.

Figure 4.12 shows the MRMS composite reflectivity (colors) and azimuthal shear (dark shading) along with the probabilistic forecast of 2-5 km updraft helicity greater than in the 9 km neighborhood for the LPF and EnKF experiments. By 2200 UTC, the EnKF model shows a line of storms, albeit shorter than the observed line. The corresponding LPF forecast at one hour is similar, but has even less convection along the southern extent of the line than the EnKF forecast. The LPF forecast has almost

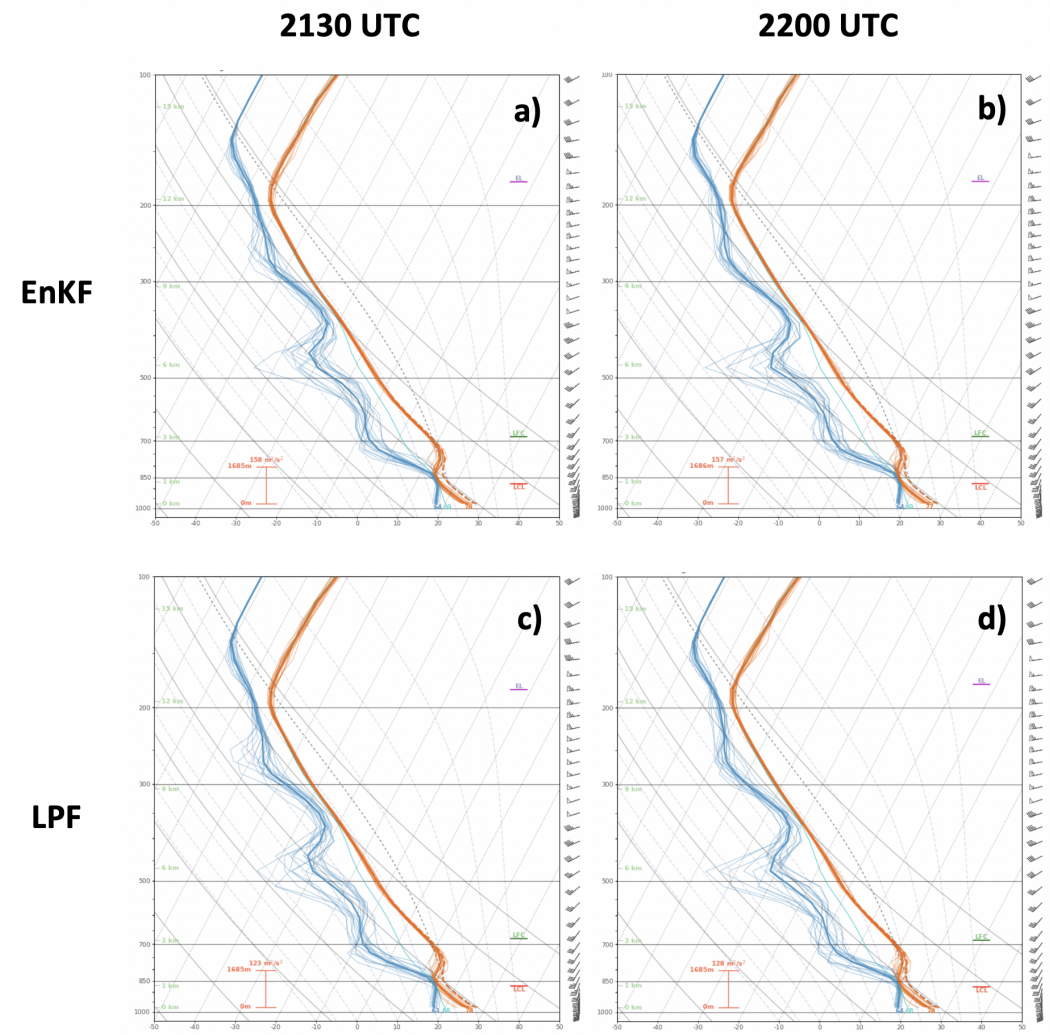

Figure 4.8: Ensemble forecast Skew-T plots of Chanute, Kansas from the 2100 UTC analysis. Left column represents 30 minute forecast soundings and right column represents 1 hour forecasted soundings. Top (Bottom) row is respectively associated with the EnKF (LPF) model. Thick lines resemble the ensemble mean and the thin lines resemble individual ensemble.

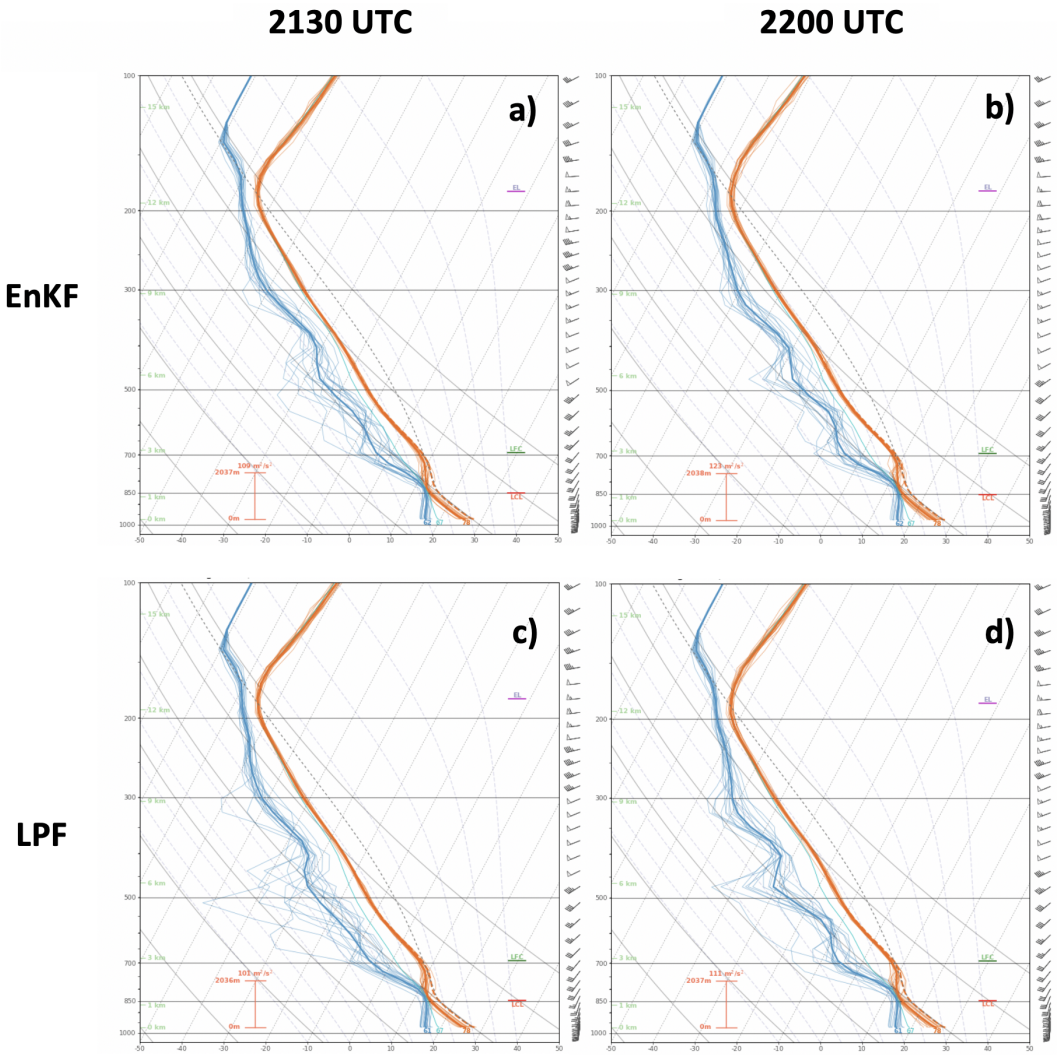

Figure 4.9: Ensemble forecast Skew-T plots of Kansas City, Kansas initialized from the 2100 UTC analysis. Left column represents thirty minute forecast soundings and right column represents sixty minute forecast soundings. Top (Bottom) row is respectively associated with the EnKF (LPF) model. Thick lines resemble the ensemble mean and the thin lines resemble individual ensemble members.

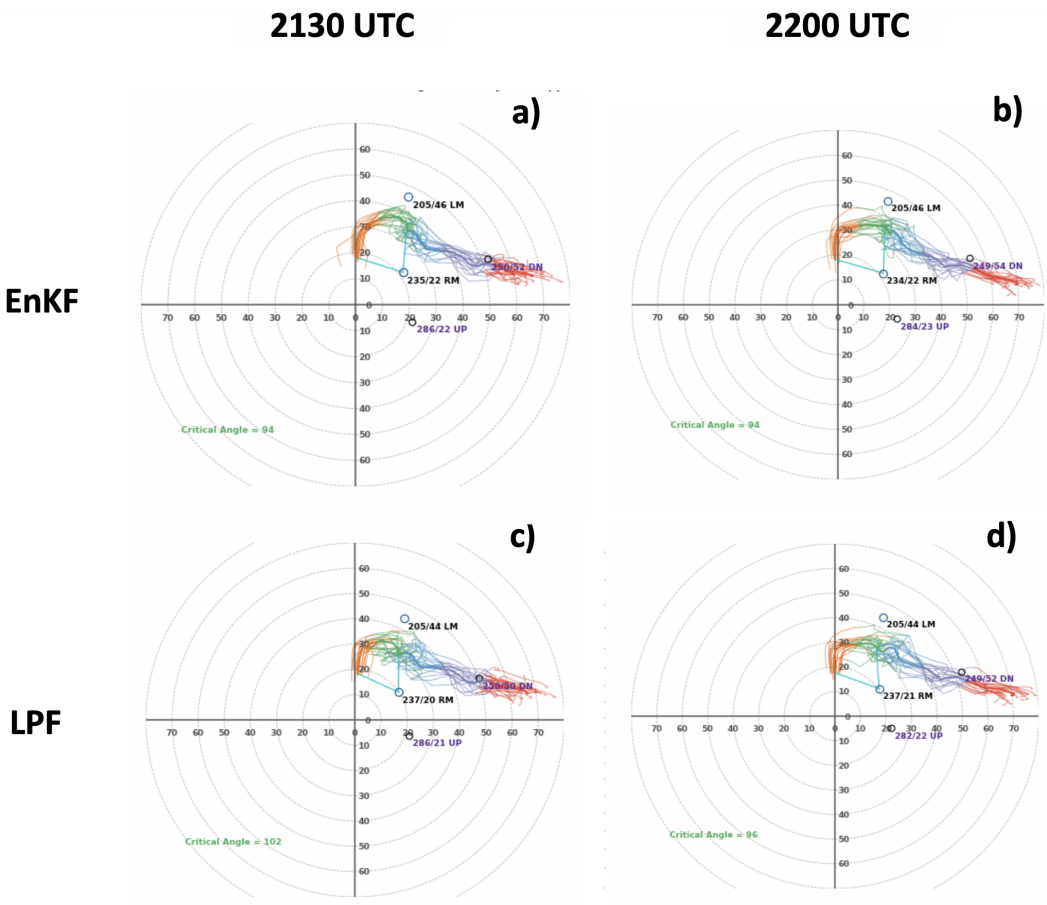

Figure 4.10: Forecasted hodograph plots of Chanute Kansas initialized at 2100 UTC. Left column represents thirty minute forecasted hodograph and right column represents sixty minute forecasted hodograph. Top (Bottom) row is respectively associated with the EnKF (LPF) model. Colors represent magnitude of winds at different heights, orange (lowest) and red (highest).

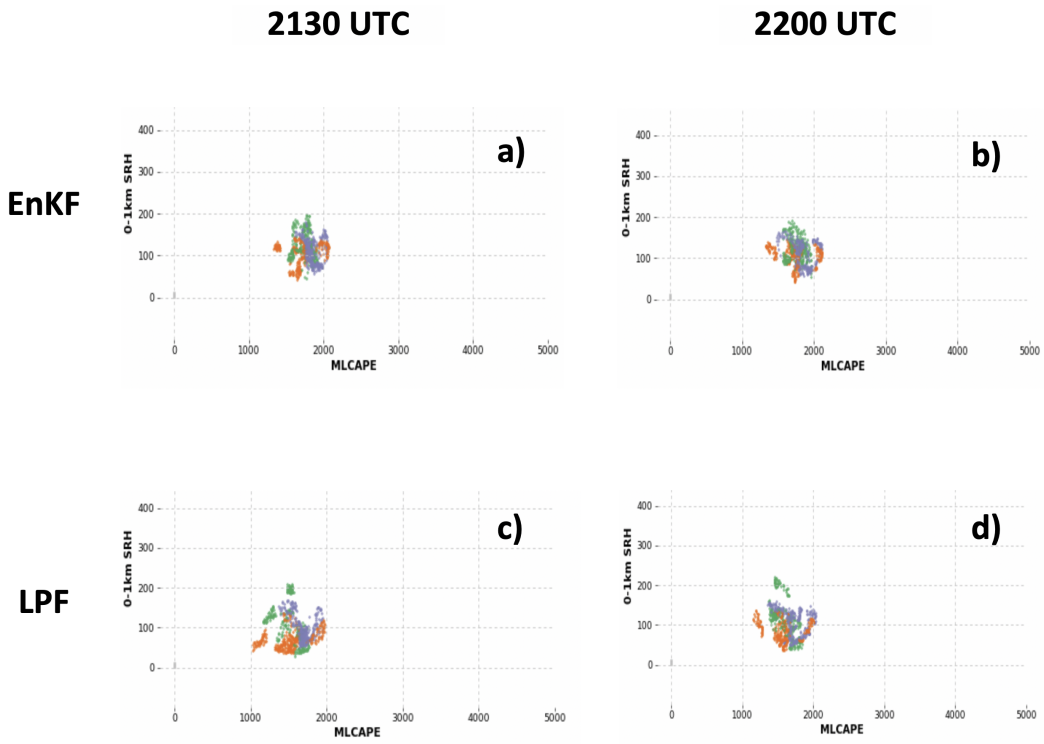

Figure 4.11: Forecast ensemble spread plots from the Chanute Kansas soundings initialized at 2100 UTC. Mean-layer CAPE is plotted the abscissa and 0-1 km storm-relative helicity is plotted on the ordinate. The left column represents thirty minute forecast spread plots and right column represents sixty minute forecasted spread plots. Top (Bottom) row is respectively associated with the EnKF (LPF) model. Dots represent spread of a given planetary boundary layer scheme. Orange indicates YSU, green indicates MYJ and purple for MYNN.

no convection in southeast Kansas or Iowa. By 2300 UTC the storms within the EnKF forecast form a more linear structure spanning from east-central Nebraska through central Kansas whereas the observed storms in Kansas were comprised of discreet cells. However, the LPF forecast fails to create any organized convection moving into southwest Iowa. By 0000 UTC the impact from the drier LPF environment can be seen. The EnKF retains numerous storms in northern Kansas, however in the LPF forecast the storms have decayed. The MRMS azimuthal shear (dark shading) indicate the strength of the observed mesocyclone. The EnKF experiment generates a number of mesocyclone swaths for each convective cell. So does the LPF forecast, but by 0000 UTC only the storms closest to the Kansas-Nebraska border have persisted.

Integrated precipitable water vapor content represents the total atmospheric water content contained within a vertical column. In order to determine the amount of moisture in the simulated environment, 10-minute forecast plots of precipitable water are created to diagnose the cause of storm decay within the LPF experiment. At 2200 UTC significant differences in moisture are present in the analyses (Fig. 4.13). The environment within the LPF experiment is significantly drier ahead of the storms, specifically in southwest Iowa, eastern Nebraska, and extending south-southwest along the dryline into Kansas. Similar to the soundings from Chanute shown in Figure 6.15, the LPF experiment is much drier above the boundary layer extending upwards to 400 hPa. The integrated effect of this drier environment is seen in Figure 6.19 and strongly suggests that the weaker convection in the LPF experiment results from this mesoscale difference.

Another method of diagnosing the cause of decay within the LPF experiment is determining the amount of mean layer CAPE ahead of the storm. A substantial amount of instability is needed in order to sustain severe convective storms. Plots of mean layer

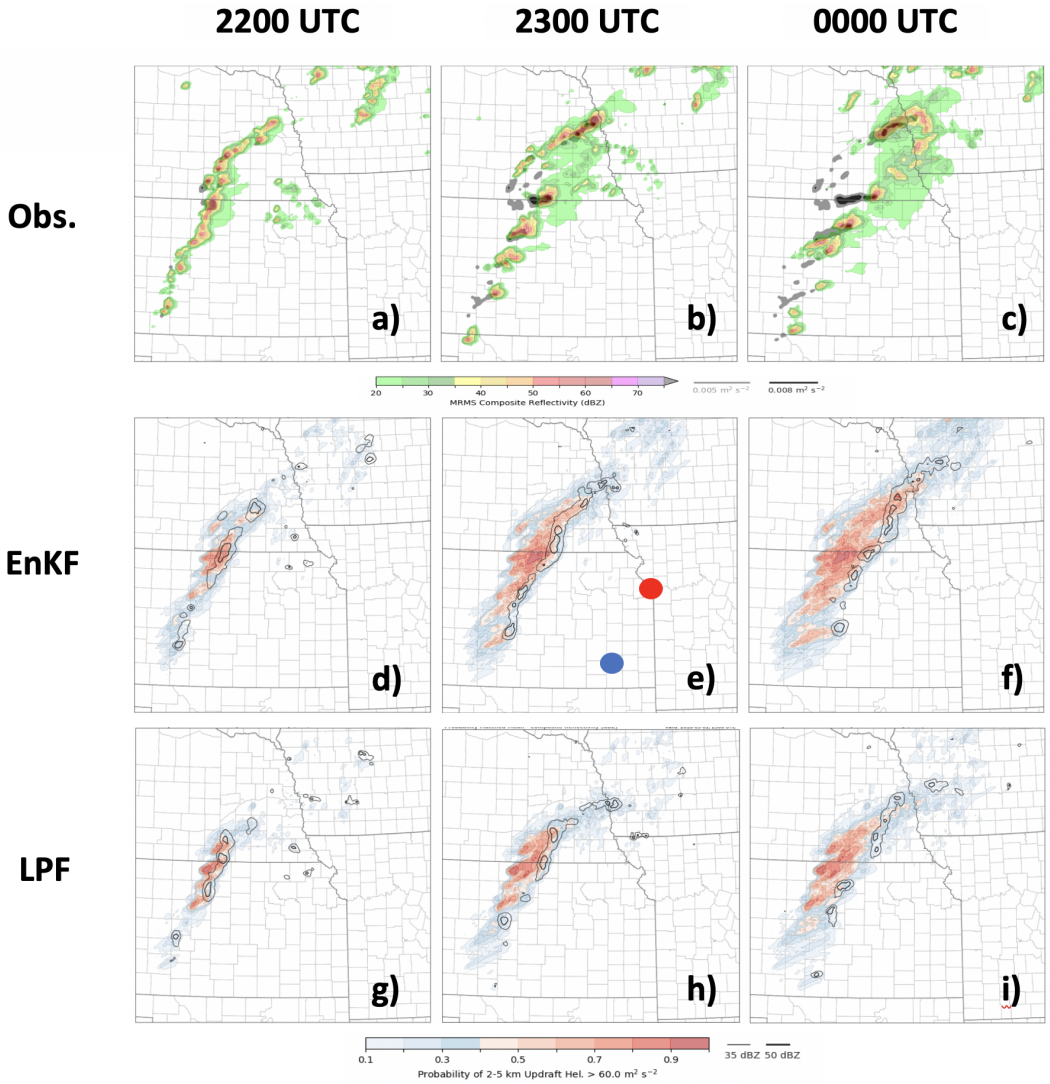

Figure 4.12: Top row is MRMS composites of reflectivity and thirty minute aimuthal shear. Center and bottom rows are forecasts of the probability of 2-5 km helicity exceeding 60 m^2s^2 and mean ensemble reflectivity shown with two black contours (25 and 45 dBZ, respectively). Forecasts are initialized at 2100 UTC. Left column represents one hour forecasts, center column represents two hour forecast and right column represents three hour forecasts. Blue dot (e) shows the forecast sounding location of Chanute Kansas and the red dot (e) shows the forecast sounding location of Kansas City.

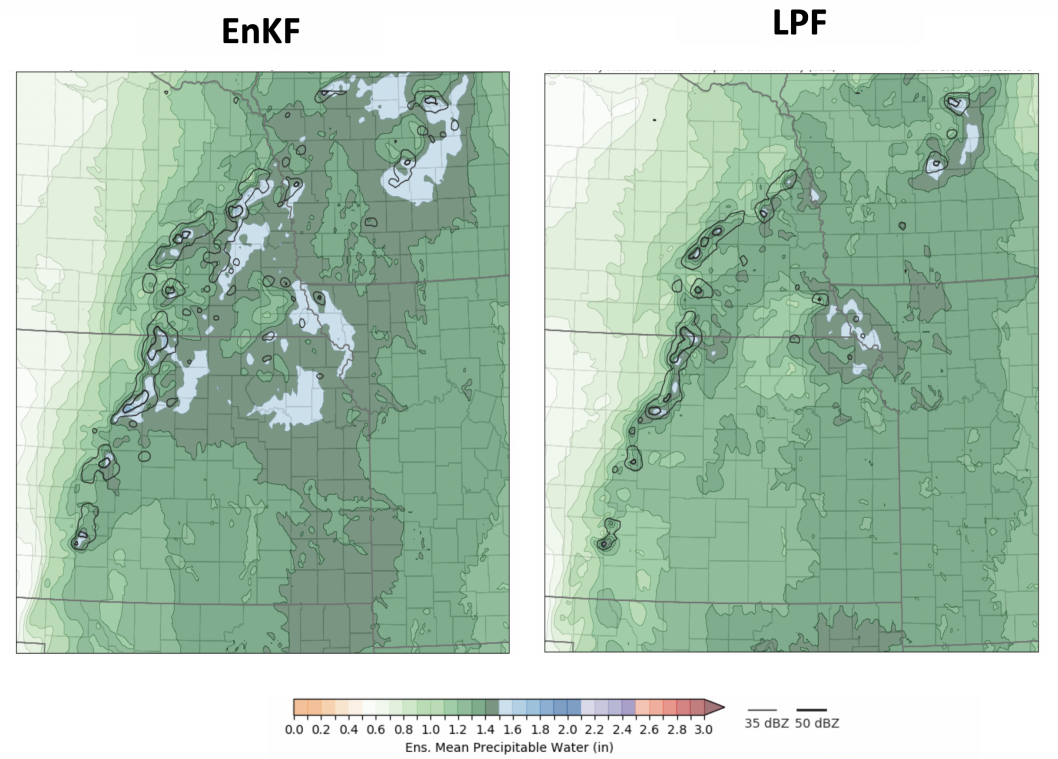

Figure 4.13: Plots of total column precipitable water content after 10 minutes of integration initialized at 2200 UTC for 1 May 2018. Left image resembles forecasted precipitable water plots of the EnKF model and right represents the LPF model.

CAPE are analyzed to establish its relationship to the lack of development of the LPF storms in comparison to the EnKF experiment (Fig. 4.14). Large differences in CAPE is evident ahead of the storms, especially across Kansas and southeast Nebraska. The lower amount of CAPE is a result of the drier environment within the LPF and may contribute to the early decay of storms.

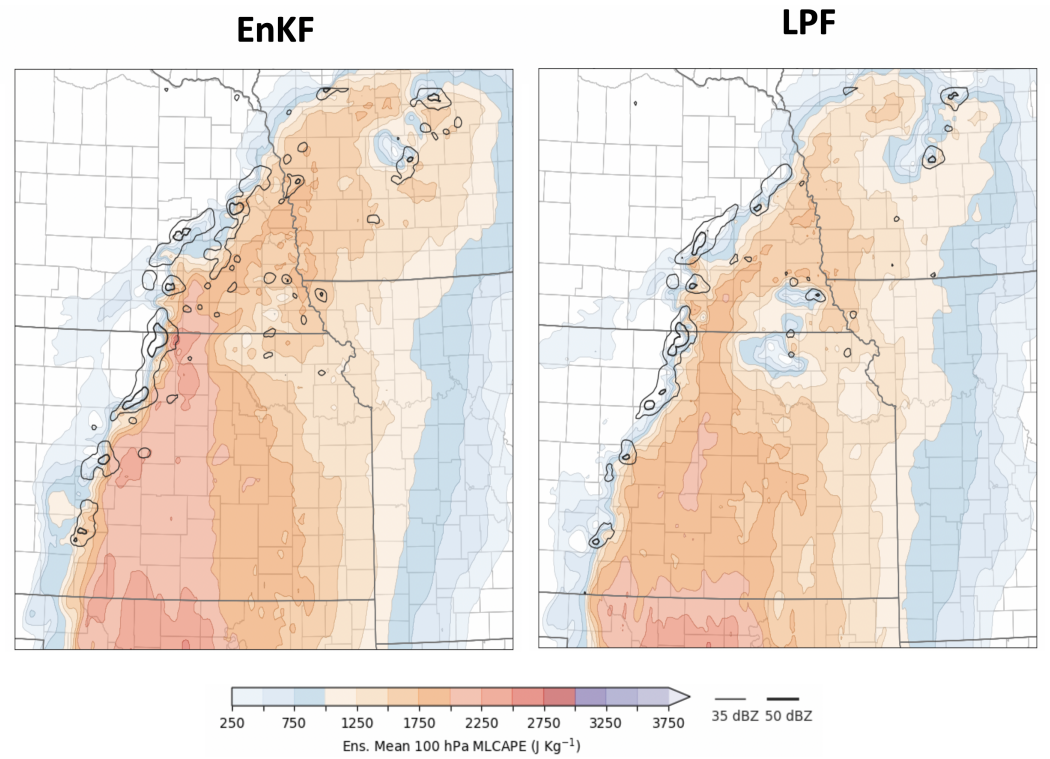

Figure 4.14: Plots of mean layer CAPE after 10 minutes of integration initialized at 2200 UTC for 1 May 2018. Left image resembles forecasted precipitable water plots of EnKF model, and right represents the LPF model.

4.1.4 Objective Verification

Performance diagrams (Roebber, 2009) exploit the relationship between the four statistical measures of forecast performance: probability of detection (POD), false alarm ratio, success ratio (SR; 1 – FR), bias and critical success index (CSI). Perfect forecasts will be aligned in the upper right corner of the diagram, indicating POD, SR, bias and CSI approaches 1. Deviations from the center line indicates differences in PODs and SR, which further leads to adjustments of bias and CSI. On the diagram, a shift along a 45° angle represents an optimal increase in accuracy, maintaining unbiased forecasts while simultaneously increasing the POD and success ratio (lower false alarm rate).

For this study, performance diagrams are created for reflectivity for the thirty minutes, one-hour, and two-hour forecasts from the first eighteen ensemble members of

each experiment (Fig. 4.15). Initially, the EnKF experiment is overpredicting the number of storms leading to a larger POD with a positive bias. A fewer number of storms in similar locations is forecasted by the LPF, yielding a lower bias and POD. In both forecasts the POD of the EnKF and LPF decreases at later forecast time as displacement errors increase between the forecast and the observed storm objects. As the storms within the LPF forecast decay between the one-hour and two-hour forecasts, both the SR and POD are decreasing. When averaged over the two-hour period, the EnKF forecasts have somewhat greater skill than the LPF forecasts. This suggests that if the drier environment in the LPF experiment could be eliminated so that it was closer to the environment in the EnKF experiment that the LPF storm-scale forecasts could have benefited from its less biased initial analyses and performed comparably or even better than the EnKF forecasts. In theory, more moisture will further lead to larger mean layer cape values, allowing the storms to continue to persist and possibly lead to greater POD and SR scores.

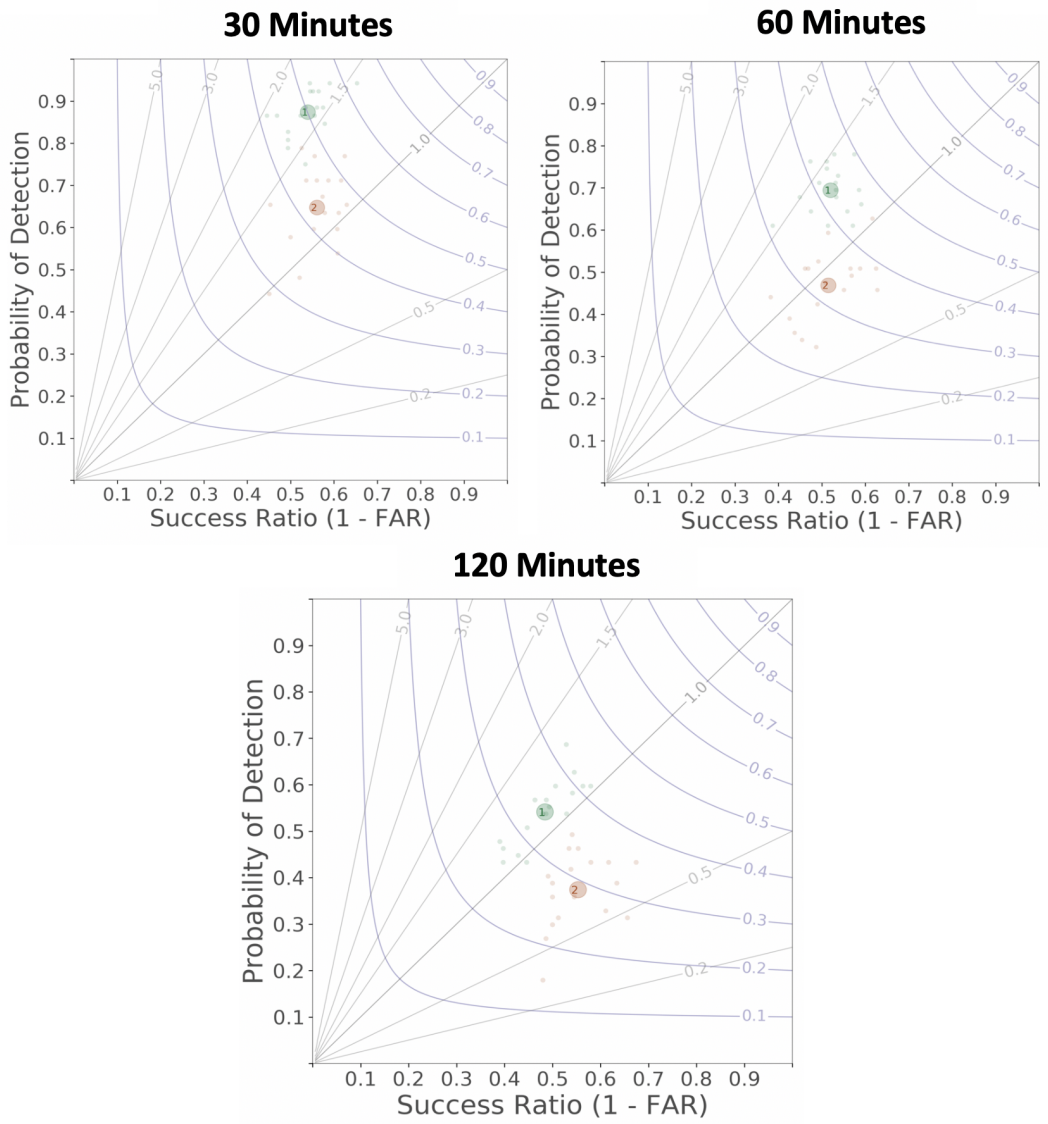

Figure 4.15: Performance diagrams of 30/60/120 minute forecasts for the 1 May case starting at 2100 UTC for reflectivity objects using the methodology from Skinner et al. (2018). Green dots represent the EnKF experiment and orange dots represent the LPF. Large dots are the ensemble mean, and small dots are the scores of the individual members.

4.2 2 May 2018 Case

4.2.1 Case Description

The second case of this study is the 2 May 2018 event. Supercell storms formed off the dryline along the western border of Oklahoma, leading to many storm reports spanning from southwestern Texas, across the plains towards Iowa, leading into Michagan. These convective cells initiated off a dryline, producing over a dozen tornadoes in central Oklahoma and hail greater than 2.5 inches. Most of the tornadoes were concentrated in southwestern Oklahoma and central Kansas. This case is focused within the region outlined in Fig. 4.16.

The convection in Oklahoma began around 1900 UTC. Observed MRMS composites reflect the hourly evolution of the storms in Figure 4.17. The storms in Kansas form into a linear system as they propagate to the east, whereas the convection in Oklahoma and Texas maintains their supercellular structure. According to the 1800 UTC Norman, Oklahoma sounding (Fig. 4.18), the environment was favorable for severe, given the moisture and wind profile. Moist air propagated from the Gulf of Mexico into Oklahoma and Kansas, leading to high dewpoints up to 20 degrees Celcius. Additionally, moderate veering vertical sheer was present within the environment to induce rotation.

4.2.2 Observation Space Statistics

Similar to the 1 May 2018 case, surface and WSR-88D radar observations are assimilated every 15 minutes. In addition to these observations, cloud water path from GOES-16 are also assimilated every 15 minutes.

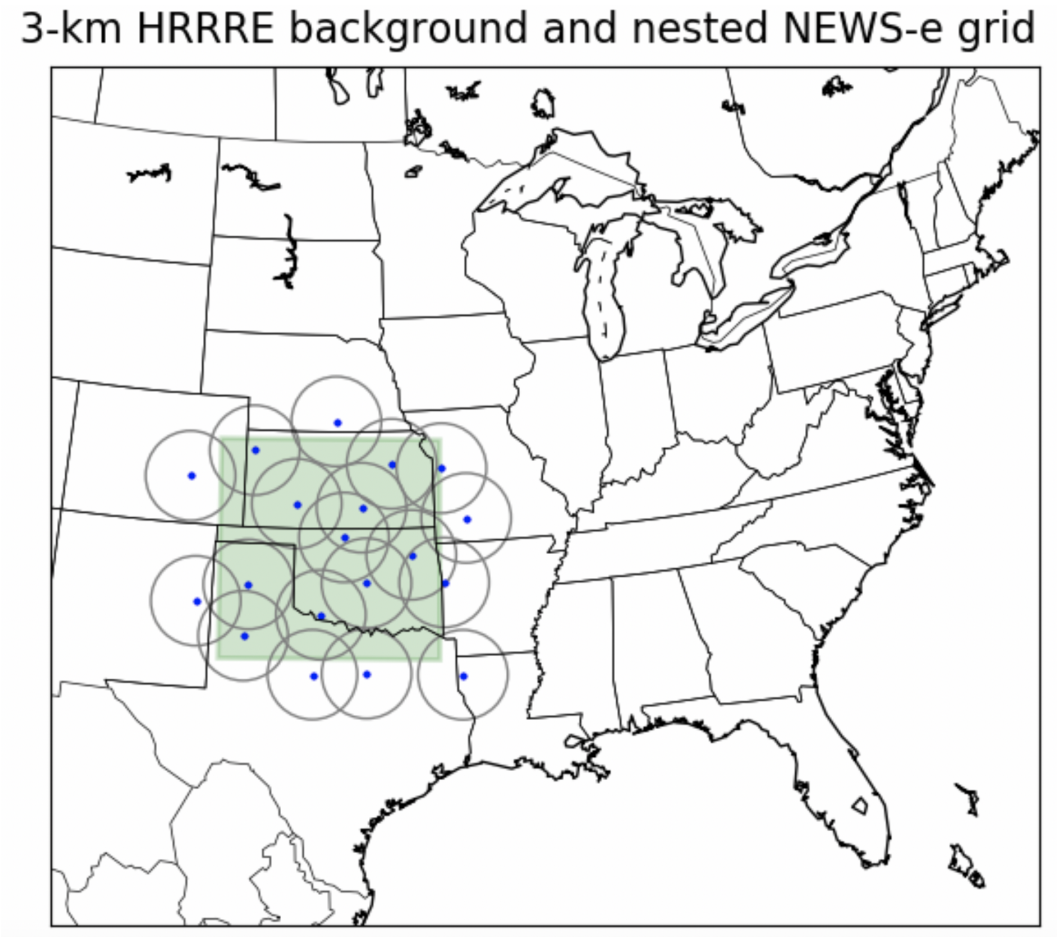

Figure 4.16: Domain of study for 2 May 2018 case. Green square indicates the region of study and blue dots indicate radar locations. The 150-km range rings around each radar depict the maximum range of observations used in the assimilation.

Radar observations are present throughout the assimilation cycles due to the prior convective initiation of the Kansas storm. Rapid adjustment of prior and posterior RMSE (Fig. 4.19) within the first few cycles is an outcome of the early available observations. Towards the end of the assimilation period the EnKF experiment displays a continual increase of RMSE whereas the LPF experiment RMSE remains nearly constant. This behavior is similar to the 1 May case. The ability of the LPF to assimilate reflectivity in a more consistent manner may be advantageous. Diagnostics from the assimilation of radial wind (Fig. 4.20) is also similar to the previous case in

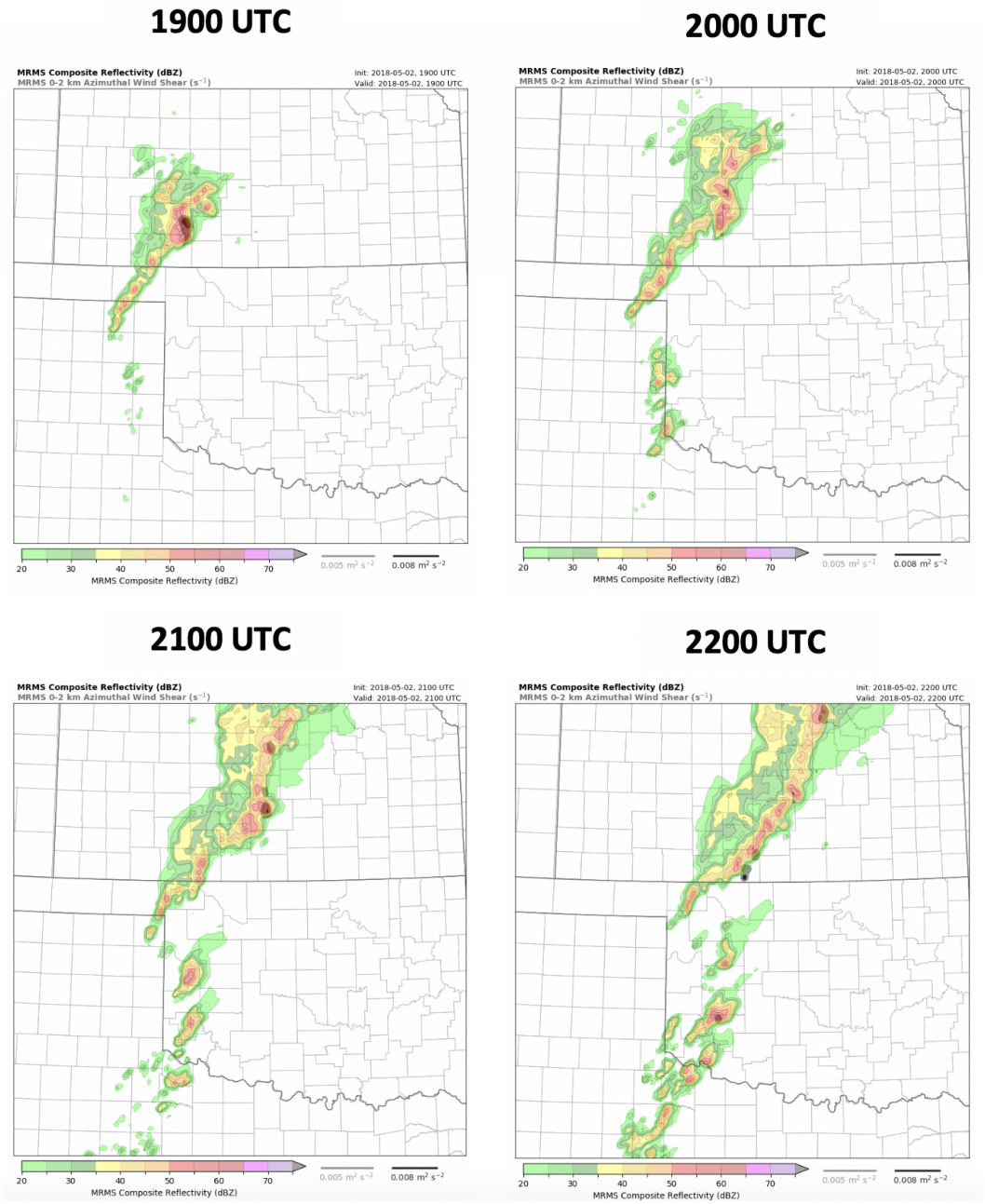

Figure 4.17: Hourly storm evolution for 2 May 2018, from 1900 UTC to 2200 UTC. Color plots are the MRMS composite reflectivity and the gray shaded regions depict regions of significant azimuthal shear during previous 5 minutes.

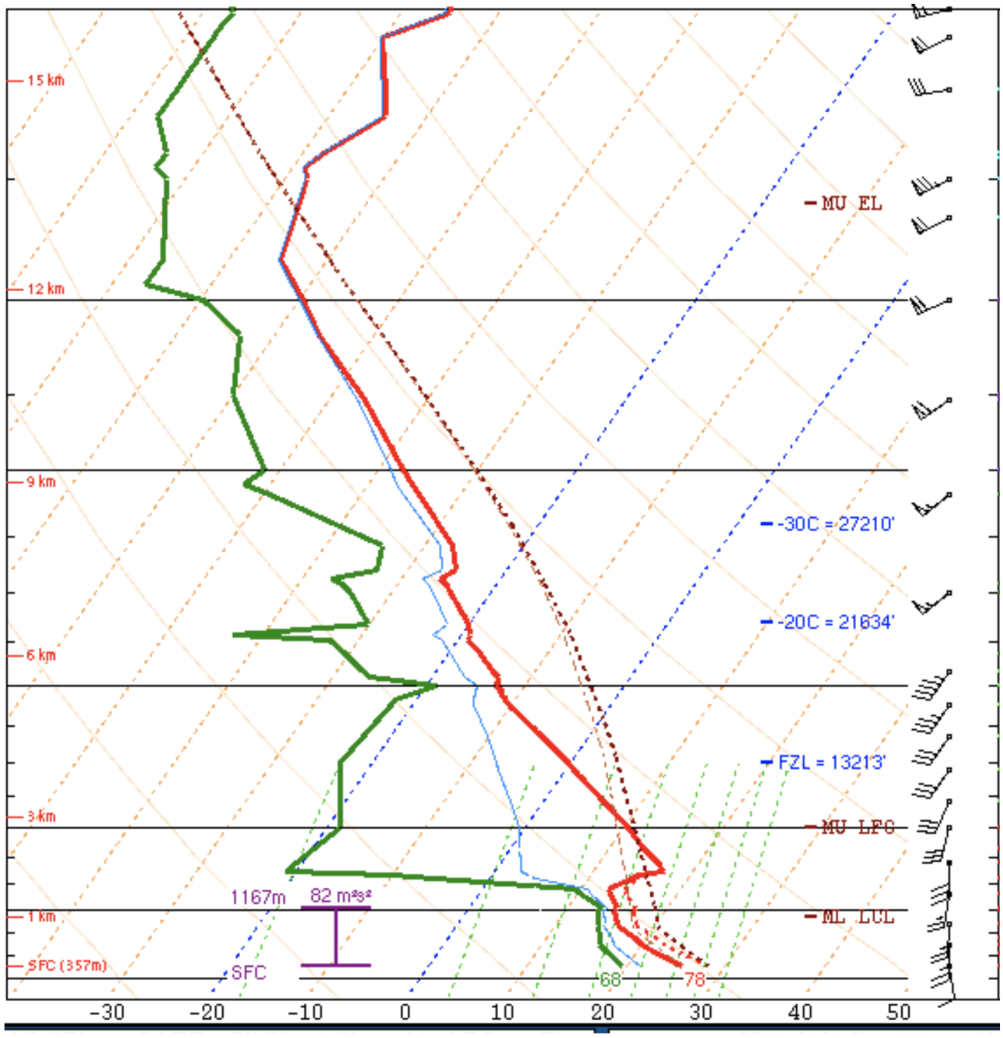

Figure 4.18: 1900 UTC Skew-T diagram at Norman, Oklahoma for 2 May 2018. Red line represents temperature, green line represents dewpoint temperature, and thin red dashed line represents the parcel path used to compute the CAPE.

which there are minimal differences between the two experiments, further suggesting that both experiments assimilate more linear variables at the same efficacy. The results are also similar for surface temperature and dewpoint measurements.

Cloud water path (Fig. 4.21) measures the total amount of water within a cloud along a vertical column of the atmosphere from the GOES-16 satellite. The WoFS only assimilates retrievals during daylight, therefore no observations are available after 0100 UTC. Overall the diagnostics from both experiments are similar. The LPF experiment maintains more spread throughout the assimilation cycling. Towards the latter half of the cycling, the LPF experiment has lower posterior RMSEs than the EnKF, inferring the LPF analysis is fitting the observations somewhat better.

4.2.3 Storm-Scale Forecast Analysis

Figure 4.22 shows the thirty- and sixty-minute forecast soundings from the 2100 UTC forecasts. Soundings will be shown from Norman, Oklahoma. Differences in the environment can lead to inconsistencies between the two experiment's forecasts. Overall, the shape of the sounding profiles are similar between the EnKF and LPF analyses. Most of the differences between ensemble members is noticed near the top of the boundary layer in the dewpoint temperature profiles. More uncertainty is present within the LPF than the EnKF for the thirty-minute and sixty-minute soundings, as more members stray towards a drier mid-level environment. Towards the latter forecast, the ensemble mean temperature for the LPF forecast is one degree (C) higher than the EnKF forecast at the surface. The surface LPF forecast mean dewpoint temperature is one degree (C) lower, indicating the predicted environment is drier within the LPF experiment.

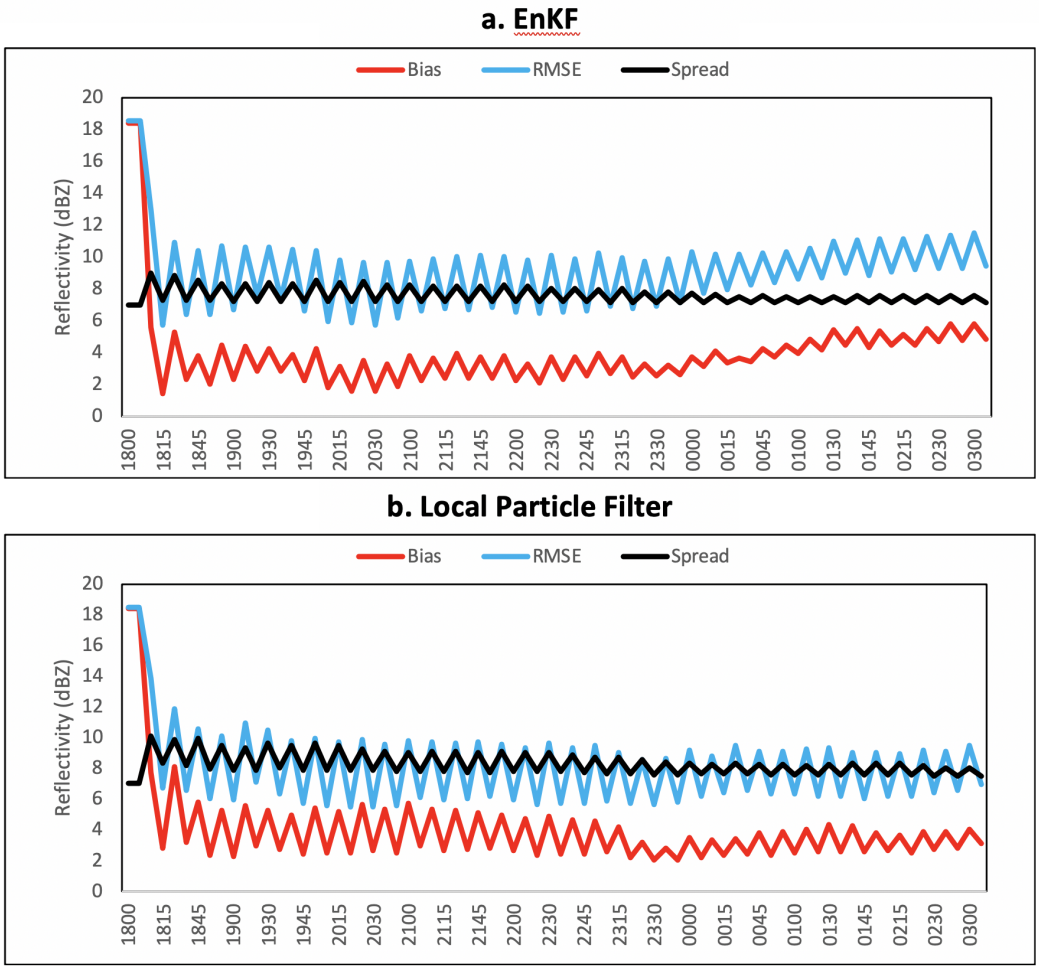

Figure 4.19: Observation-space diagnostic statistics for assimilated WSR-88D reflectivity for (a) the ensemble Kalman filter and (b) the local particle filter. Red line represents the bias, blue line represents the RMSE, and black line represents the total spread.

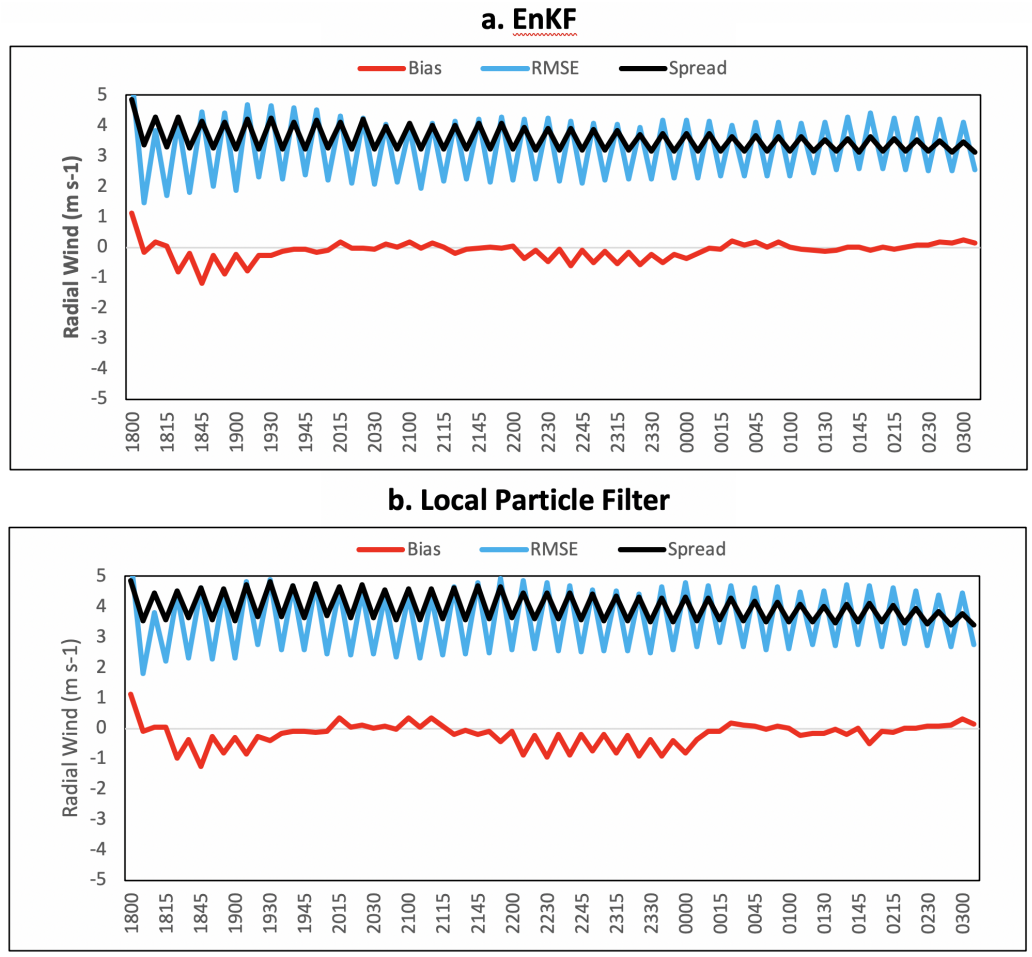

Figure 4.20: Observation-space diagnostic statistics for assimilated WSR-88D radial wind observations for (a) the ensemble Kalman filter and (b) the local particle filter. Red line represents the bias, blue line represents the RMSE, and black line represents the total spread.

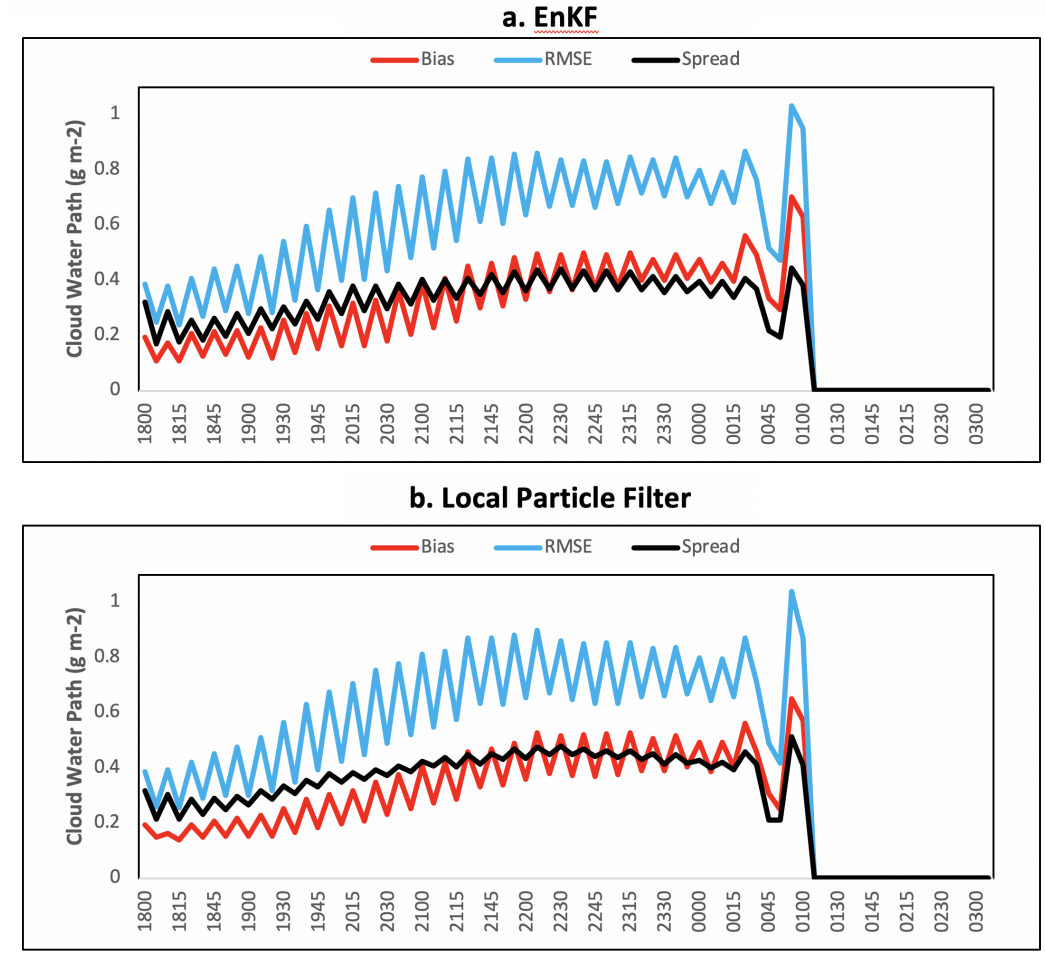

Figure 4.21: Observation-space diagnostic statistics for assimilated GOES-16 cloud water path observations for (a) the ensemble Kalman filter and (b) the local particle filter. Red line represents the bias, blue line represents the RMSE, and black line represents the total spread.

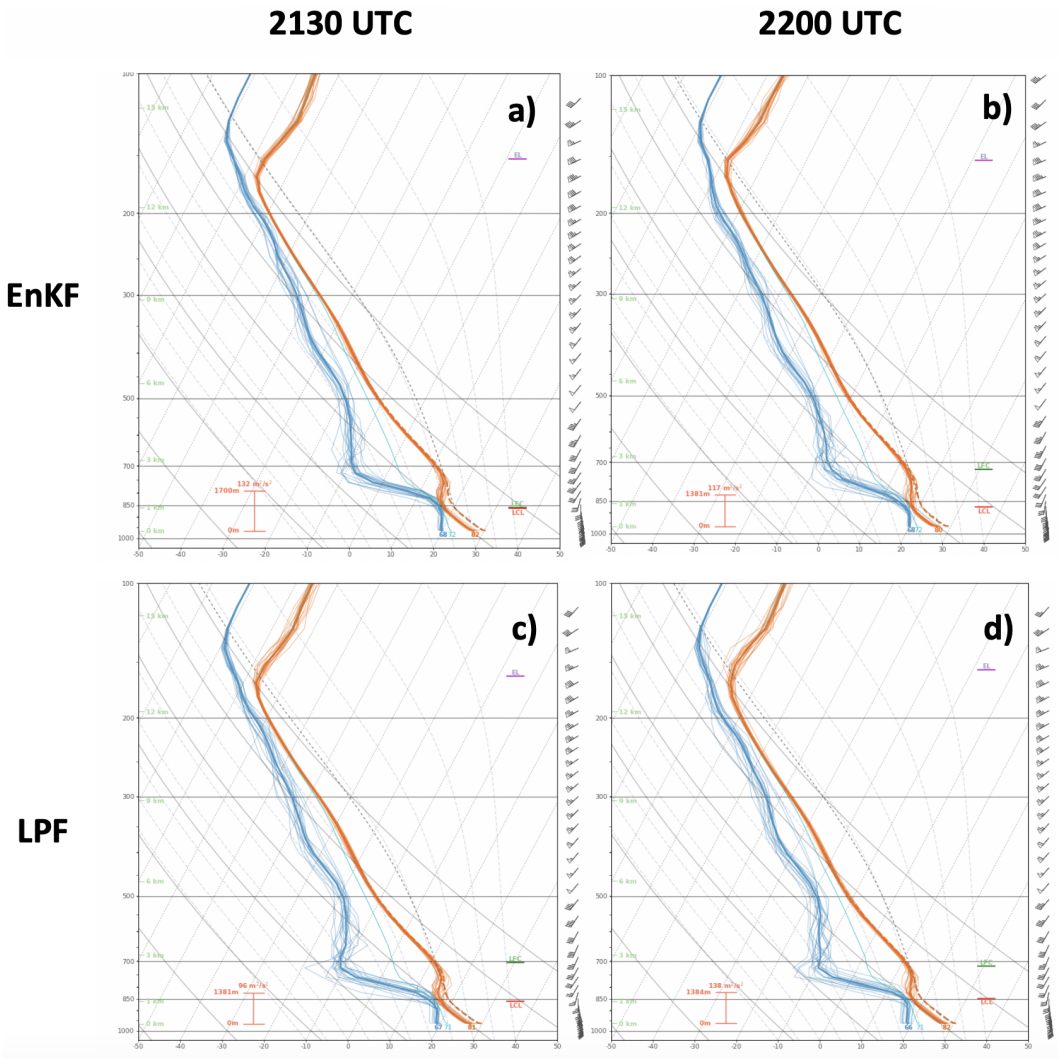

Figure 4.22: Skew-T plots of the forecast Norman, Oklahoma sounding initialized at 2100 UTC. Left column represents thirty minute forecast soundings and right column represents one hour forecasted soundings. Top (Bottom) row is respectively associated with the EnKF (LPF) model. Thick lines resemble the ensemble mean and the thin lines resemble individual ensemble members.

Hodographs show the vertical profile of horizontal winds for Norman, OK at 30 and 60 minutes into the 2100 UTC forecast (Fig. 4.23). Strong, veering vertical shear is present and conducive to severe storm development. For the thirty-minute forecast hodographs, the two experiments forecast similarly shaped hodographs, however the LPF experiment again has more spread in the winds, particularly at low- to mid-levels. By 60 minutes, the spread in LPF is even larger relative to the EnKF forecast. Moreover, the LPF forecasts show a smoother veering of the winds at the top of the boundary layer – perhaps associated with deeper mixing seen in the thermodynamic profiles. There are large differences in the mean-layer CAPE (Fig. 4.24) between experiments. The forecast CAPE from the EnKF is always between 2000-3000 $J\ kg^{-1}$ at 2130 UTC and between 1800-2500 $J\ kg^{-1}$ at 2200 UTC. The LPF forecasts (on average) lower CAPE (1500-2200 $J\ kg^{-1}$) at 2130 UTC, but by 2200 UTC the mean-layer CAPE is now spread between 1400-2500 $J\ kg^{-1}$. In both experiments the 0-1 km SRH is 100-120 $m^2\ s^{-2}$. Overall the LPF forecasts have a more diverse environment at the Norman OK location during this time period.

For this case, plots of forecast updraft helicity swaths and composite reflectivity initialized at 2100 UTC can be found within Figure 4.25. Both experiments failed to predict the southern extent of the storms along the Texas-Oklahoma border throughout the three-hour forecast period. The Kansas linear system was successfully maintained by the EnKF through the three-hour timeframe with significant mesocyclone signatures, however the system decayed with the LPF experiment after two hours. The other two remaining storm cells in Oklahoma are also predicted by both experiments. Observations show the northern cell to have weaker rotation than the southern cell. The EnKF forecasts these two cells to have similar rotation and structure, whereas the LPF forecast initially predicted that the northern cell had strong rotation (but in a

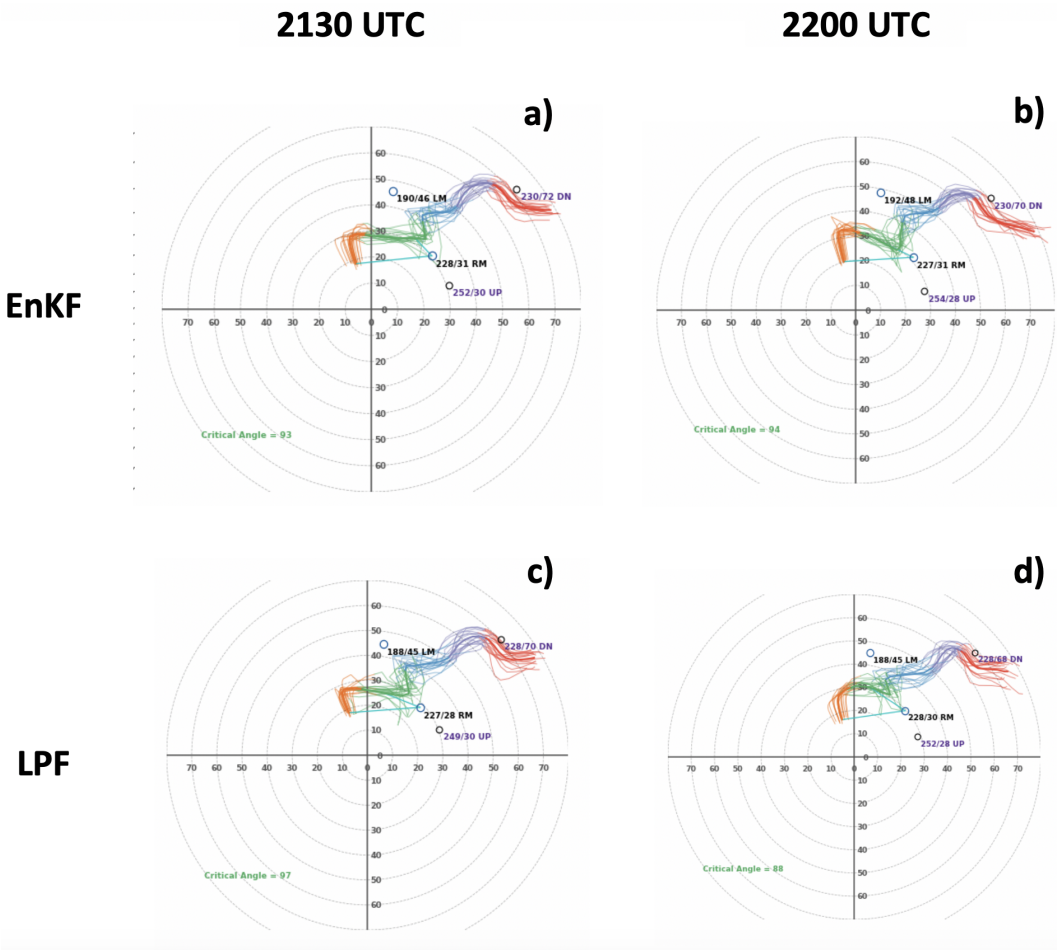

Figure 4.23: Forecasted hodograph plots of Norman, Oklahoma initialized at 2100 UTC. Left column represents thirty minute forecasted hodograph and right column represents one hour forecasted hodograph. Top (Bottom) row is respectively associated with the EnKF (LPF) model. Colors represent magnitude of winds at different heights, orange (lowest) and red (highest).

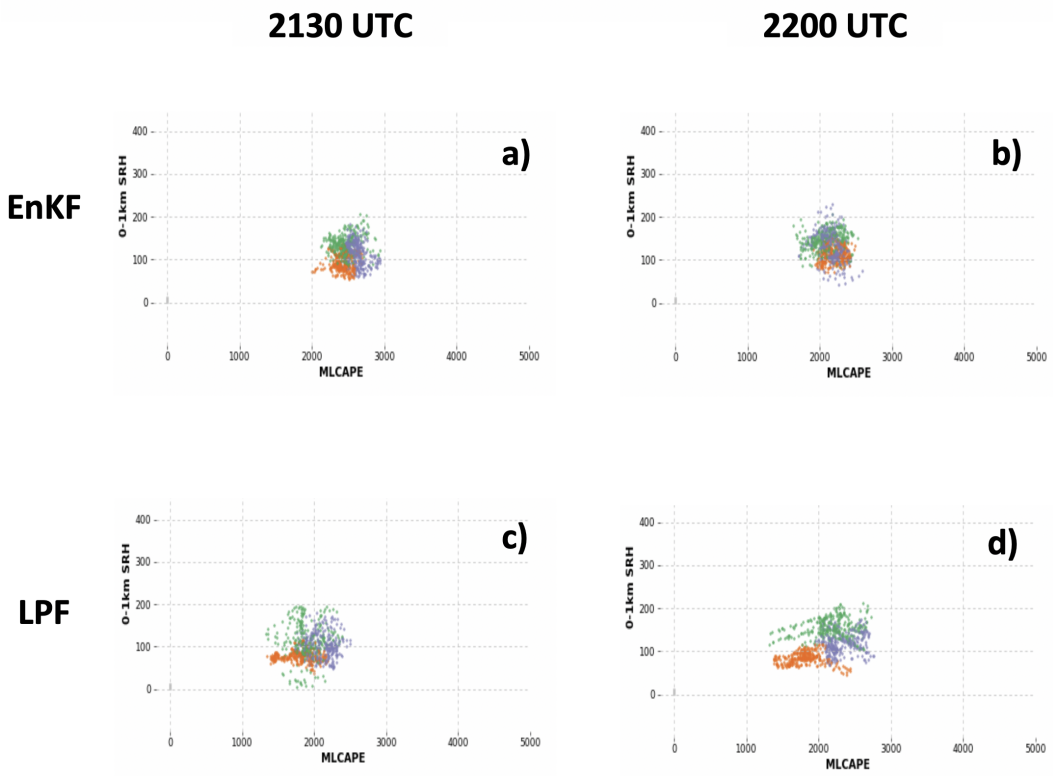

Figure 4.24: Forecast ensemble spread plots of Norman, Oklahoma soundings initialized at 2100 UTC. Mean-layer CAPE is plotted the abscissa and 0-1 km storm-relative helicity is plotted on the ordinate. The top (Bottom) row is respectively associated with the EnKF (LPF) model. Dots represent spread of a given planetary boundary layer scheme. Orange indicates YSU, green indicates MYJ and purple for MYNN.

wider path than the EnKF) at 2200 UTC. The EnKF forecasts preserved the structure of the two western OK storms through the three hour forecast, while the observations show only the southern storm maintains its structure and strong rotation. In the LPF forecasts the storms start to deteriorate after the first hour of the forecast. This is consistent with the large spread in forecasted instability represented in the Norman, OK forecast soundings.

To further diagnose why storms "die" in the LPF forecasts, Figure 4.26 shows plots of precipitable water after 10 minutes starting at 2200 UTC. As in the 1 May case previously discussed, the environment within the LPF experiment is drier (in the column) than the EnKF forecasts over all of Oklahoma. This similar result as in the 1 May case suggests that with respect to the mesoscale environment, the LPF needs further tuning.

Mean layer CAPE (Fig. 4.27) is also used to determine why the storms do not persist in the LPF experiment. As in the 1 May case, differences in CAPE is noticed within the environment ahead of the storm. The largest differences occur across central Oklahoma and south central Kansas. Overall, the EnKF experiment creates more CAPE than the LPF, like the prior case. To further reiterate, the lower levels of CAPE may be a result of the drier environment. The lack of moisture within the LPF experiment is hypothesized to be linked to the premature decay of the storms.

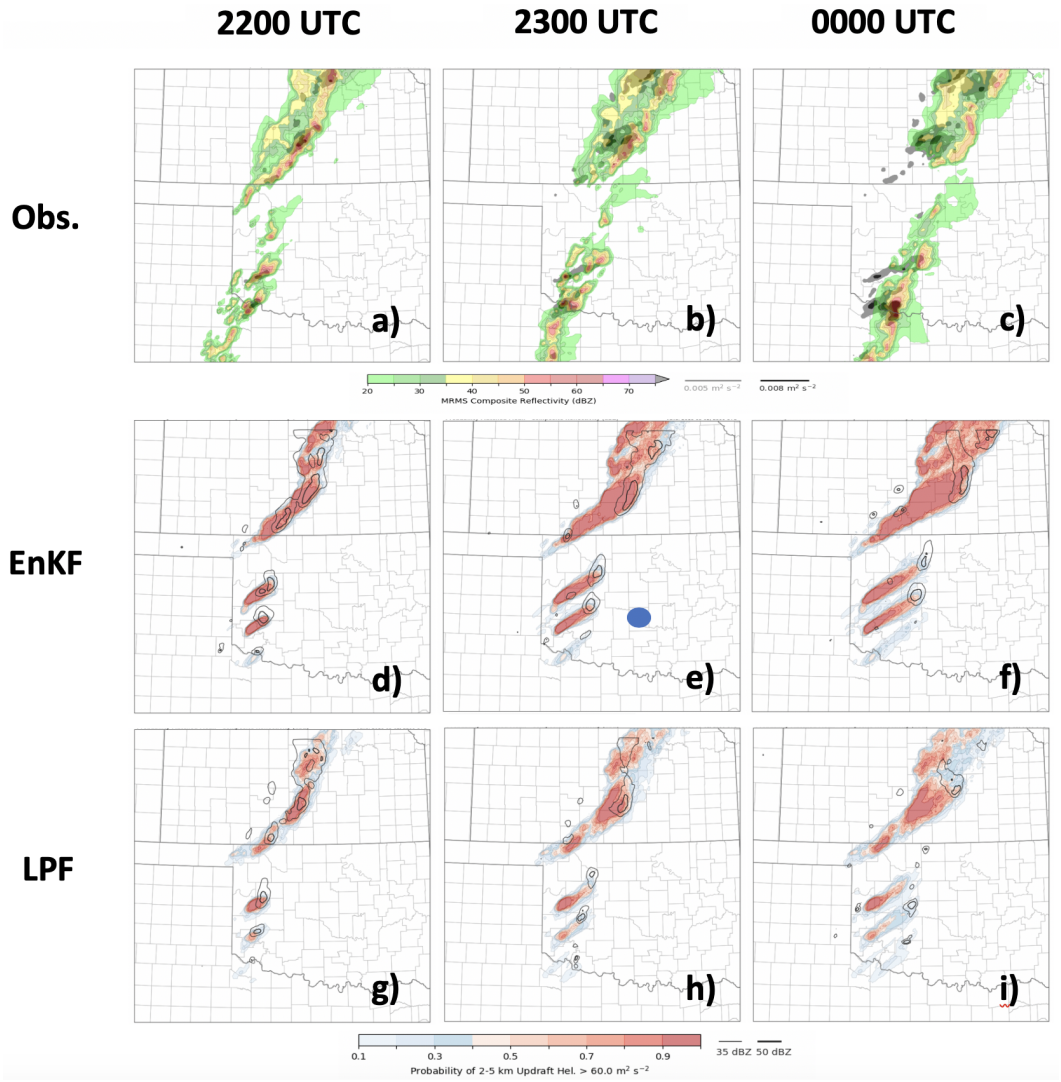

Figure 4.25: Top row is MRMS composites of reflectivity and thirty minute azimuthal shear. Center and bottom rows are forecasts of the probability of 2 – 5 km helicity exceeding 60 m^2s^2 and mean ensemble reflectivity shown with two black contours (25 and 45 dBZ, respectively). Forecasts are initialized at 2100 UTC. Left column represents one hour forecasts, center represents two hour forecasts and right column represents three hour forecasts. Blue dot is the Norman OK sounding location.

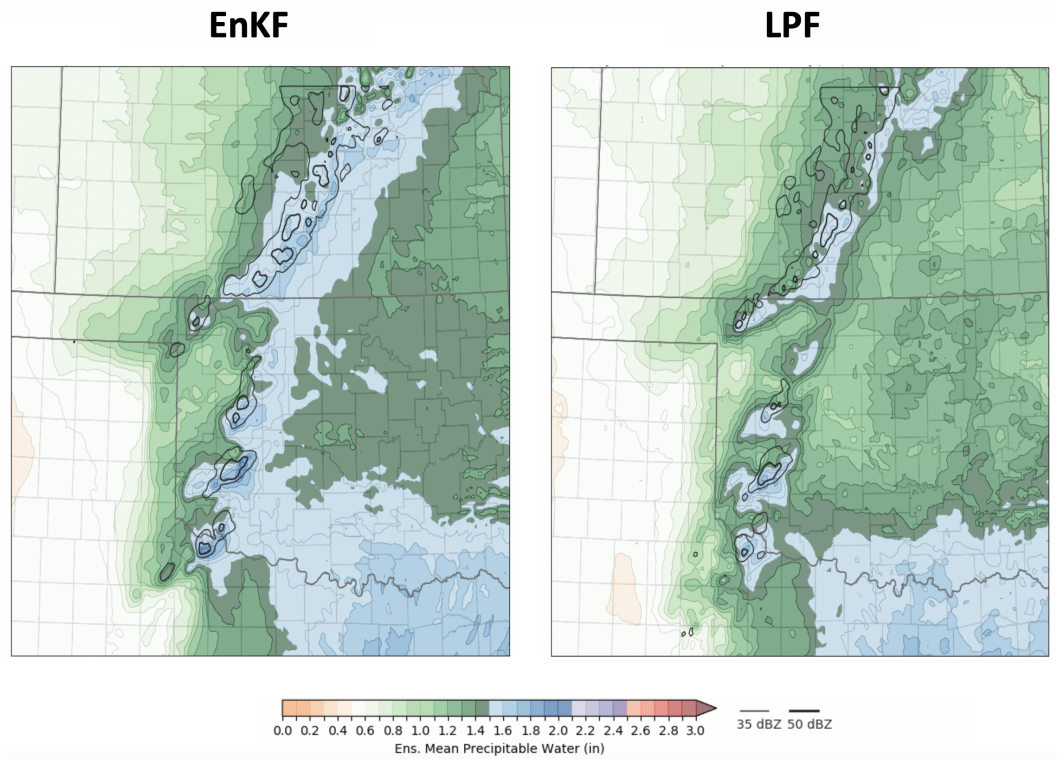

Figure 4.26: Plots of total column precipitable water content after 10 minutes of integration initialized at 2200 UTC for 2 May 2018. Left image resembles forecasted precipitable water plots of EnKF model, and right represents the LPF model.

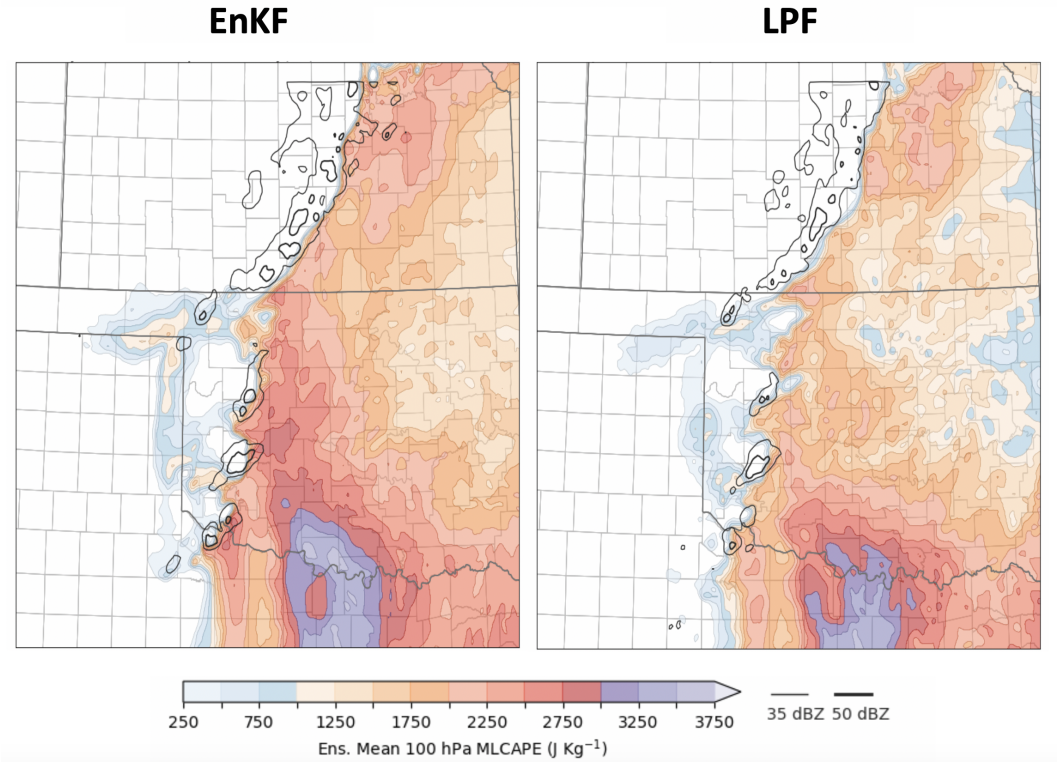

Figure 4.27: Plots of mean layer CAPE after 10 minutes of integration initialized at 2200 UTC for 2 May 2018. Left image resembles forecasted precipitable water plots of EnKF model, and right represents the LPF model.

4.2.4 Verification

Performance diagrams are used to verify the forecasts to the observations for reflectivity (Fig. 4.28) for 30, 60, and 120 minute forecasts of both experiments. Similar to the 1 May 2018 case, the EnKF and LPF are overpredicting the number of the storms, indicated by the positive bias. Overall, the LPF creates less storms than the EnKF, resulting in a lower POD. As the storms decay in the LPF forecast, a trend of decreasing POD and SR is established. Moreover, the EnKF forecast presents a greater skill score than the LPF. If the LPF had the ability to create a more moist environment, it would possibly lead to less bias in the latter forecasts and a greater POD and SR, leading to a more optimal CSI.

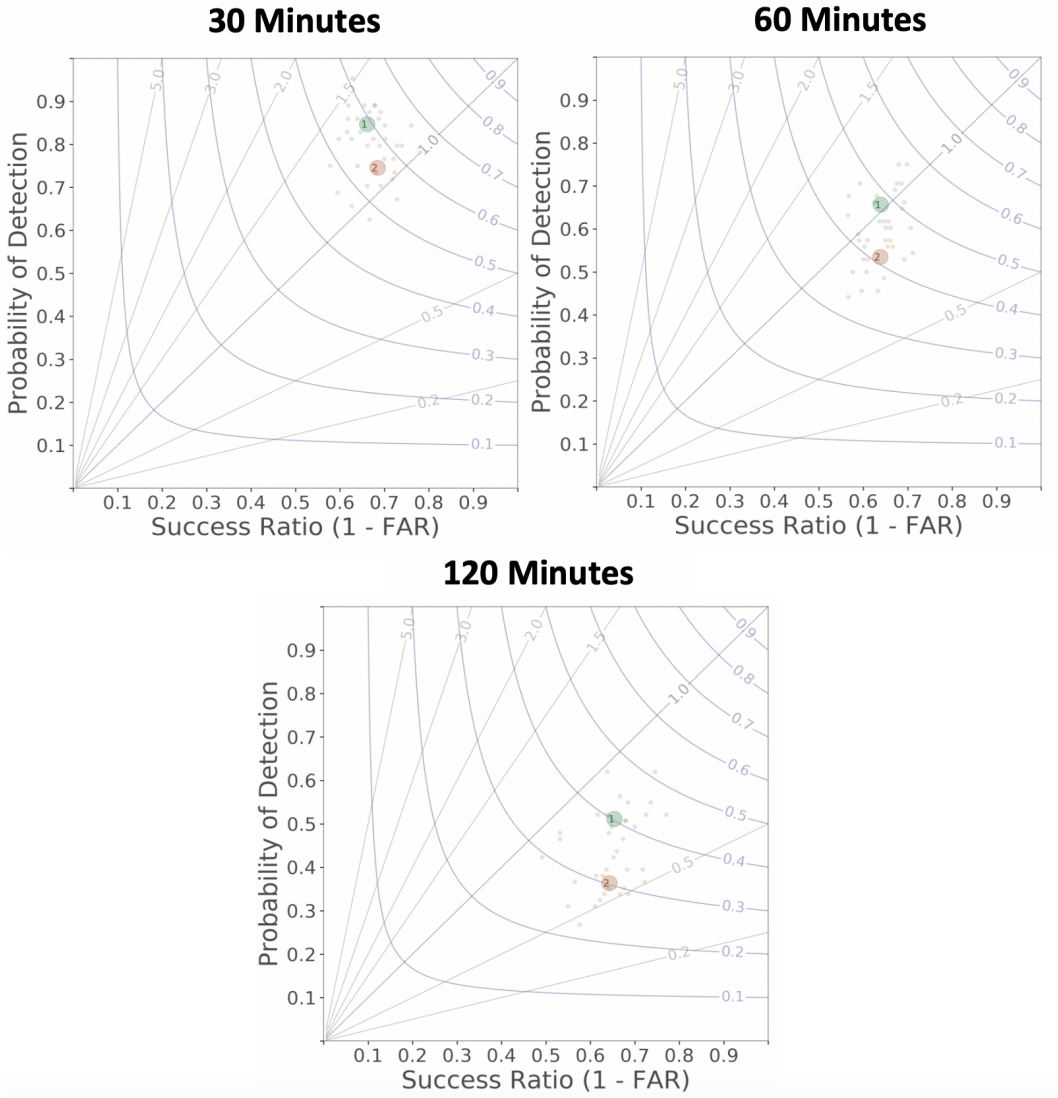

Figure 4.28: Performance diagrams of 30/60/120 minute forecasts for the 2 May case starting at 2100 UTC for reflectivity objects using the methodology from Skinner et al. (2018). Green dots represent the EnKF model and orange dots represent the LPF. Large dots are the ensemble mean, and small dots are the scores of the individual members.

4.3 Dry Bias Diagnostics

Results from the two cases show that the LPF cycling generates a tends to dry out the column moisture in pre-storm environment. This increases inhibition and reduces CAPE, leading to weaker storms and early decay compared to the EnKF experiment. By 2100 UTC, the reduced moisture within the LPF environment has already impacted the forecasts and analyses of the LPF. The diagnostics focus on earlier assimilation cycles to determine when the dry bias originates. To identify the source of the bias, posterior and prior precipitable water data were analyzed to detect any discrepancies between the two assimilation systems. The diagnostics will focus on the 2 May 2018 case.

Within the first few assimilation cycles of the 2 May 2018 case, the mean environment within the LPF posterior environment clearly is becoming drier than the EnKF's mean posterior environment (Figs. 4.29 – 4.31). For the discussion here the ensemble mean precipitable water content is used to represent the model's moisture fields. The two-dimensional field of precipitable water is used as a proxy for the model's three-dimensional vapor is validated by examining several layers of the vapor mixing ratio at low- to mid-levels. The results are very similar with the LPF analyses trending drier and drier as the analysis cycle is repeated. The two-dimensional precipitable water field simplifies the discussion while representing what is happening to the model's vapor mixing ratio fields.

Figures 4.29 – 4.31 show the ensemble mean precipitable water content and analysis increments for the EnKF and LPF from 1800 UTC to 1900 UTC. Only three of the five analysis cycles are shown. Outside of the convection in Kansas and the Texas Panhandle[1], the LPF difference fields (Figs. 4.29d-4.31d) are mostly blue, indicating a

[1]The large increment values in southeast Oklahoma are due to the assimilation of cloud water path observations in the LPF (figure not shown).

reduction of total precipitable water by the LPF scheme after assimilating the observations. Increments in those same regions are positive from the EnKF analysis, inferring that the scheme is slightly increasing the column moisture over much of the domain in western and central Oklahoma during the period.

To further examine how the moisture fields are being impacted, each member's prior and posterior total precipitable water values are plotted for individual locations in histogram form. Two locations were examined, Norman and Clinton OK. Both are similar, so only Clinton OK is shown. Shown are the individual member's precipitable water values and the difference histograms. Based on Figs. 4.29c,d - 4.31c,d, Clinton is located within a region where posterior precipitable water content is less than the prior after each analysis cycle. Figures 4.32 - 4.34 clearly show that trend seen in the horizontal plots in previous figures. The EnKF difference fields (Figs. 4.32c - 4.34c) show the density maximum at or near zero, indicating that the EnKF scheme is not significantly changing the moisture very much during the analysis. This is also shown by the overlapping counts in the prior and posterior fields (Figs. 4.32a - 4.34a). In contrast, the LPF histograms show and dramatic and consistent reduction. For the times shown, the LPF analysis is drying the column by 0.015-0.0175 inches for each cycle, and almost none of the members ever increase their moisture content.

It is now clear that the LPF analysis cycling leads to an overall drying of the environment when observations are assimilated. This is noticed within the first hour of the assimilation, and creates an unfavorable environment to sustain the storms during the remainder of the afternoon. This was seen in the 2100 UTC forecasts, as the weaker storms dissipate quicker than the EnKF experiment, further leading to lower POD and SR scores. Additional investigations are needed to determine why the LPF analyses

have this bias, but are outside the realm of this research. Clearly, further investigation and more tuning is needed before the LPF could be used for storm-scale NWP.

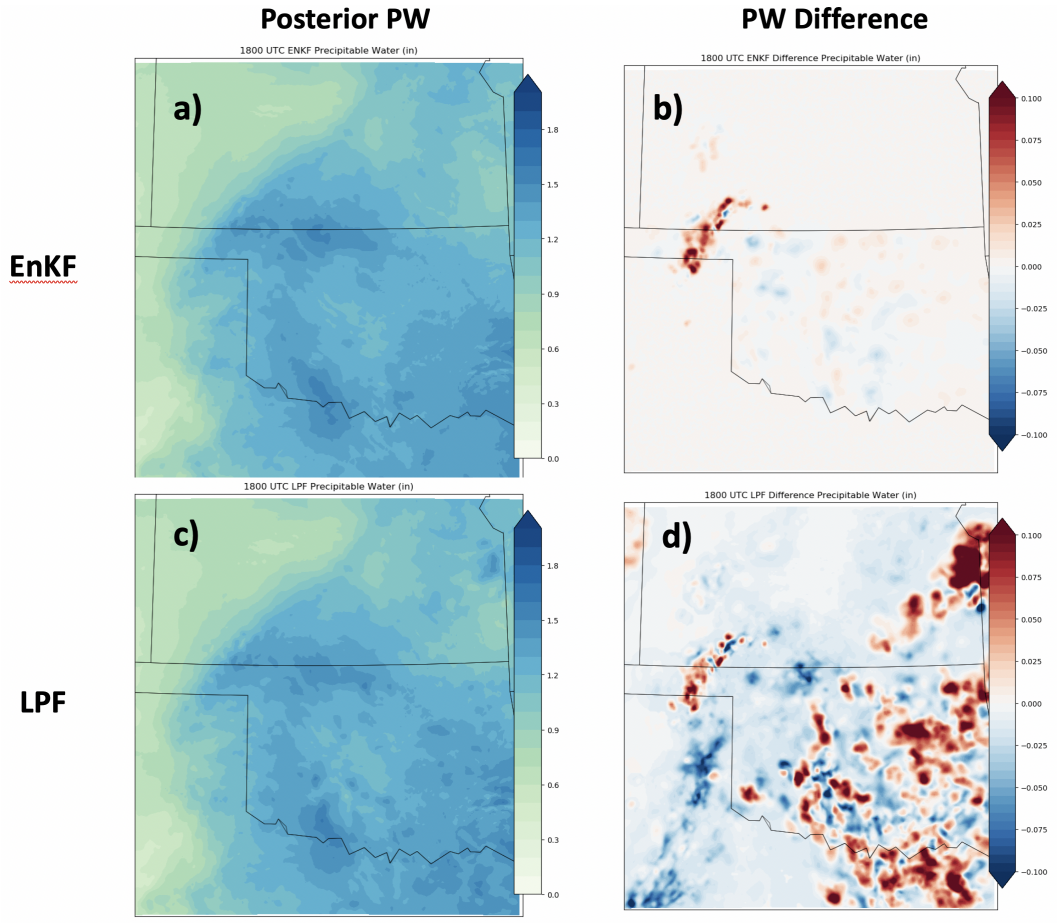

Figure 4.29: Panel of precipitable water information at 1800 UTC. Left column contains plots of precipitable water content (in) after observations are assimilated. Right column displays the increments of precipitable water after assimilation.

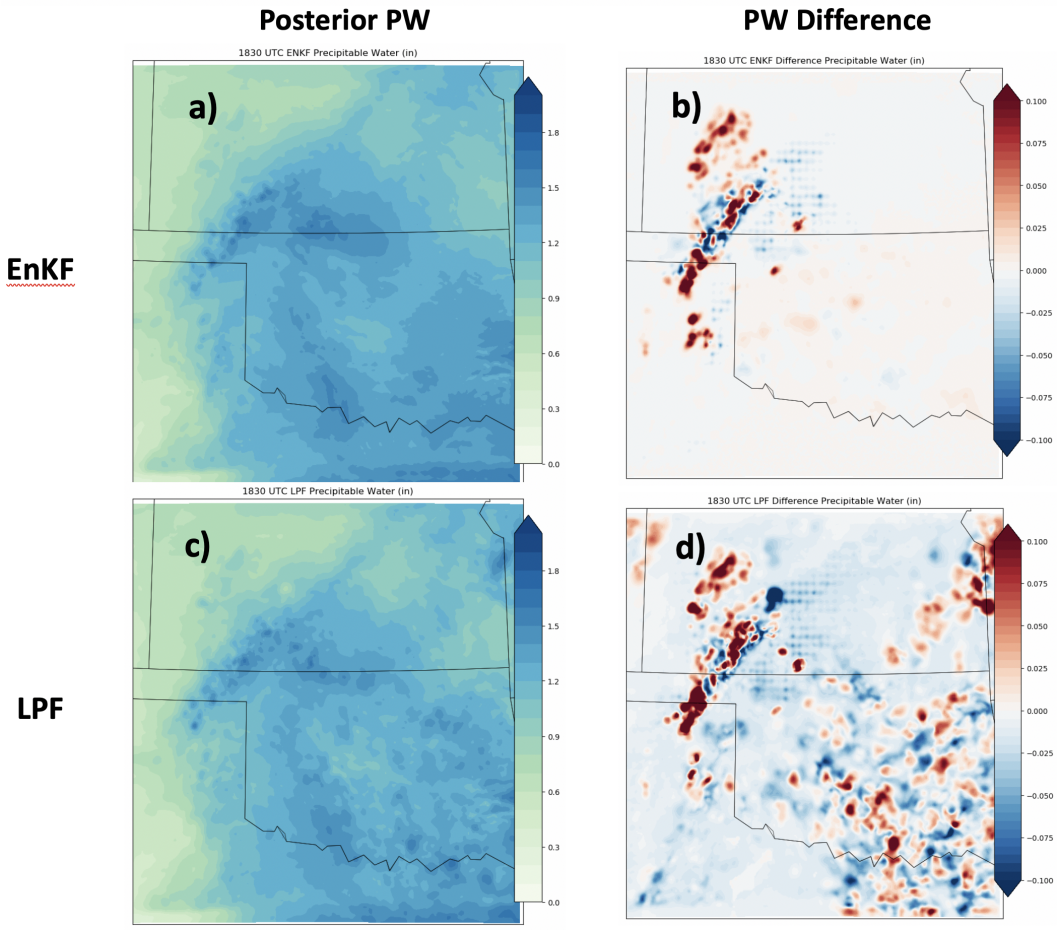

Figure 4.30: Panel of precipitable water information at 1830 UTC. Left column contains plots of precipitable water content (in) after observations are assimilated. Right column displays the increments of precipitable water after assimilation.

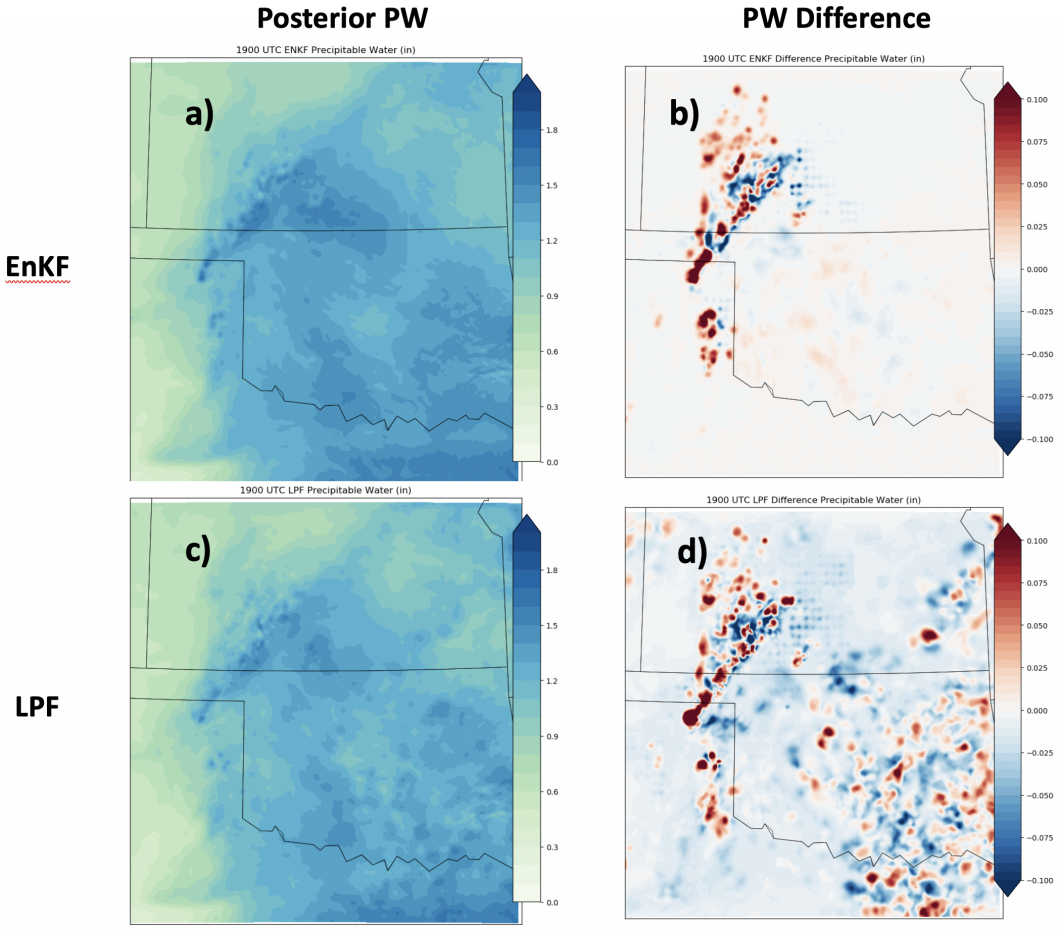

Figure 4.31: Panel of precipitable water information at 1900 UTC. Left column contains plots of precipitable water content (in) after observations are assimilated. Right column displays the increments of precipitable water after assimilation.

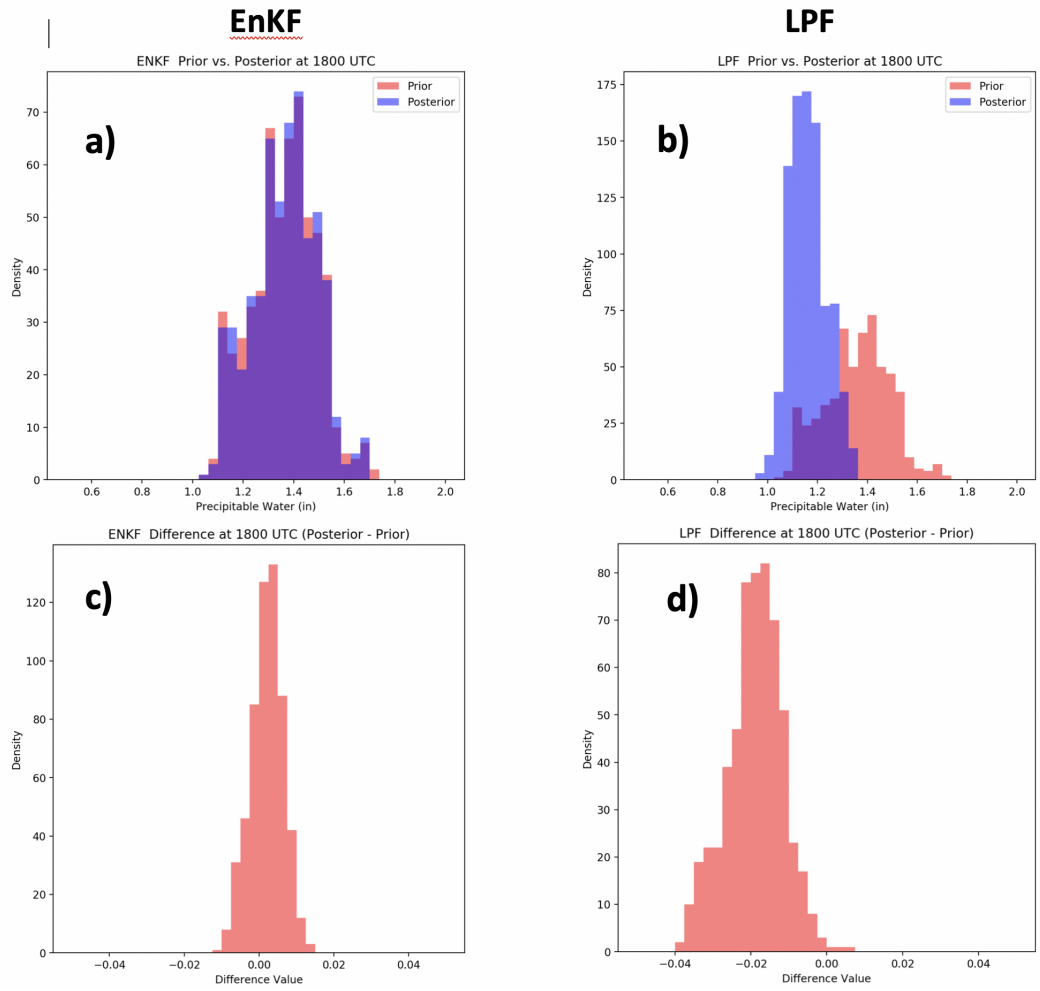

Figure 4.32: Panel of precipitable water information at 1800 UTC centered at Clinton, OK. Top row contains overlaid histograms of precipitable water content (in) before assimilation (red) and after assimilation (blue). Bottom row displays histograms of the increments in precipitable water content after assimilation.

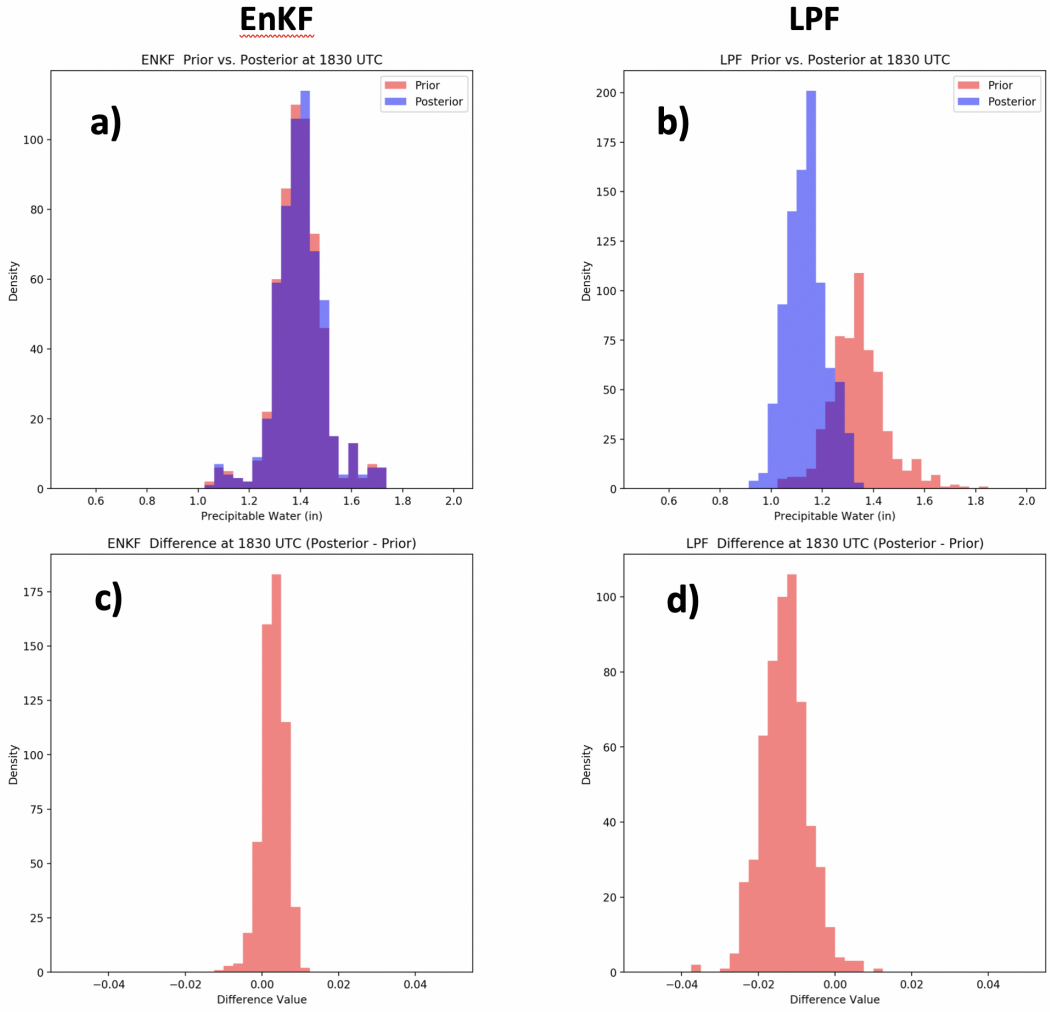

Figure 4.33: Panel of precipitable water information at 1830 UTC centered at Clinton, OK. Top row contains overlaid histograms of precipitable water content (in) before assimilation (red) and after assimilation (blue). Bottom row displays histograms of the increments in precipitable water content after assimilation.

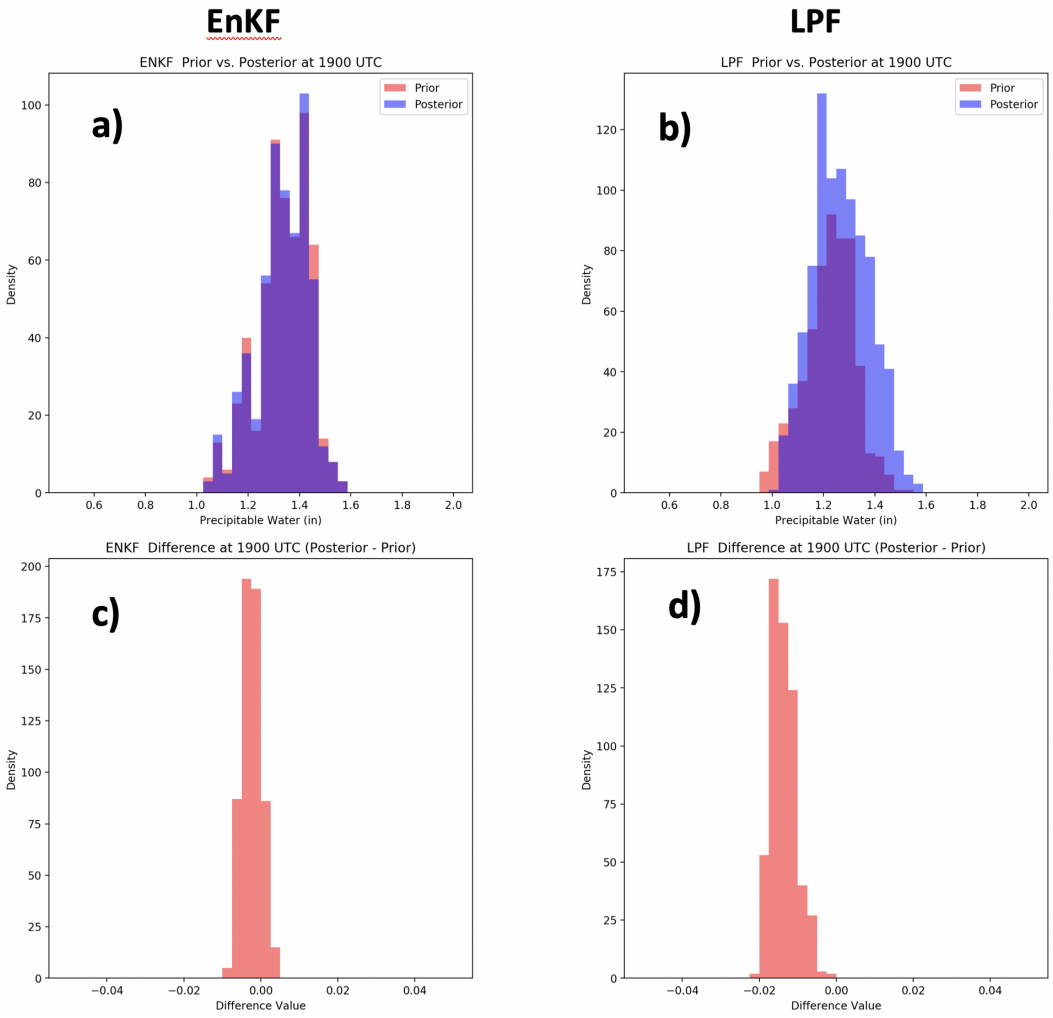

Figure 4.34: Panel of precipitable water information at 1900 UTC centered at Clinton, OK. Top row contains overlaid histograms of precipitable water content (in) before assimilation (red) and after assimilation (blue). Bottom row displays histograms of the increments in precipitable water content after assimilation.

Chapter 5

Summary and Future Work

In the study, radar reflectivity and radial velocity data, as well as surface measurements from Oklahoma mesonet stations and ASOS are assimilated into the WRF-ARW model using the renowned EnKF WoFS in comparison to the newly developed LPF. These data assimilation systems are incorporated into real-world cases, occurring on 1 May and 2 May 2018, to determine the performance of the LPF at the convective scale.

Previous studies have proven that the local particle filter outperforms the EnKF in assimilating highly nonlinear variables for idealized convective cases, and the ability to produce accurate storm forecasts. However, it is unknown how its performance will translate for real-world cases. The efficacy of the LPF WoFS is shown by comparing analyses and forecasts against the EnKF version of WoFS.

Results from the real-world cases indicate that the LPF assimilated non-linear variables (e.g. reflectivity) more optimally than the EnKF, presenting smaller posterior and prior RMSE. However, assimilation of more linear variables, such as radial wind and temperature, have shown minimal differences between the two experiments. Similar results were concluded in Poterjoy et al. 2017 in which the EAKF produced lower RMSEs for each variable except water vapor mixing ratio, a more nonlinear variable. Thirty-minute and one-hour forecast soundings are generated for both experiments to evaluate the storm environments. The LPF analysis generates more spread of dewpoint temperature in the mid- and upper-levels of the atmosphere compared to the EnKF analyses. Overall, the LPF creates a drier environment in both cases, leading

to storm decay after the first two hours of the forecast while the storms in the EnKF forecasts persist and maintain structure. In previous idealized study (Poterjoy et al., 2017), the ensemble forecasts initialized with the LPF are more accurate than forecasts initialized with the EAKF by 10-20 minutes. Lower values of mid-level moisture are present within the local particle filter for the real-time study. Performance diagrams of forecasts show that both experiments initially over-predict the number of storms, though the EnKF shows a greater bias than the LPF. The POD of both forecasts decreases through time due to displacement errors to the east, and the FAR of the LPF forecasts decreases towards the latter of the forecasts as storms decay. On average, the EnKF forecasts have a greater CSI skill score than the LPF forecasts across the thirty-, sixty-, and one-hundred and twenty-minute performance diagrams.

Although the LPF has been successful for simulated experiments and its ability to optimally assimilate highly nonlinear variables, more modifications and tuning would be ideal for real-world applications. The biggest disadvantage of the LPF is the dry bias it creates within the forecasts, primarily in the mid-levels. This occurs when the LPF generates negative water vapor mixing ratio values when the filter assimilates the observations, and was noticed within the first hour of the assimilation window. Though these values are set to zero, it is not physically realistic and leads to significant drying in the forecasts along with lower POD and SR scores. Eliminating the dry bias is optimal in order to generate more persistent storms. Furthermore, there is a possibility of creating a hybrid assimilation system which incorporates the LPF in assimilation of nonlinear variables while the EnKF system is applied to variables with more Gaussian-like properties.

Many unknowns still exist regarding the local particle filter; however, it is expected that the local particle filter will continue to contribute to the advancement of NWP.

Reference List

Anderson, J., 2007: Exploring the need for localization in ensemble data assimilation using a hierarchical ensemble filter. *Physica D: Nonlinear Phenomena*, **230 (1)**, 99 – 111, doi:https://doi.org/10.1016/j.physd.2006.02.011, data Assimilation.

Anderson, J., T. Hoar, K. Raeder, H. Liu, N. Collins, R. Torn, and A. Avellano, 2009: The data assimilation research testbed: A community facility. *Bulletin of the American Meteorological Society*, **90 (9)**, 1283–1296, doi:10.1175/2009BAMS2618.1.

Anderson, J. L., 2001: An ensemble adjustment kalman filter for data assimilation. *Monthly Weather Review*, **129 (12)**, 2884–2903, doi:10.1175/1520-0493(2001)129⟨2884:AEAKFF⟩2.0.CO;2.

Bengtsson, T., P. Bickel, and B. Li, 2008: *Curse-of-dimensionality revisited: Collapse of the particle filter in very large scale systems*, Collections, Vol. Volume 2, 316–334. Institute of Mathematical Statistics, Beachwood, Ohio, USA, doi:10.1214/193940307000000518, URL https://doi.org/10.1214/193940307000000518.

Bieringer, P., and P. S. Ray, 1996: A comparison of tornado warning lead times with and without nexrad doppler radar. *Weather and Forecasting*, **11 (1)**, 47–52, doi:10.1175/1520-0434(1996)011⟨0047:ACOTWL⟩2.0.CO;2.

Blumberg, W. G., K. T. Halbert, T. A. Supinie, P. T. Marsh, R. L. Thompson, and J. A. Hart, 2017: Sharppy: An open-source sounding analysis toolkit for the atmospheric sciences. *Bulletin of the American Meteorological Society*, **98 (8)**, 1625–1636, doi:10.1175/BAMS-D-15-00309.1.

Bouttier, F., and P. Courtier, 2002: Data assimilation concepts and methods.

Brooks, H. E., 2004: Tornado-warning performance in the past and future: A perspective from signal detection theory. *Bulletin of the American Meteorological Society*, **85 (6)**, 837–844, doi:10.1175/BAMS-85-6-837.

Cardinali, C., L. Isaksen, and E. Andersson, 2003: Use and impact of automated aircraft data in a global 4dvar data assimilation system. *Monthly Weather Review*, **131 (8)**, 1865–1877, doi:10.1175//2569.1.

Carpenter, J., P. Cliffordy, and P. Fearnhead, 2000: An improved particle filter for non-linear problems. *IEE Proc. Radar, Sonar Navig.*, **146**.

Chen, Z., 2003: Bayesian filtering: From kalman filters to particle filters, and beyond. *Statistics*, **182**, doi:10.1080/02331880309257.

Davis, C. A., B. G. Brown, R. Bullock, and J. Halley-Gotway, 2009: The method for object-based diagnostic evaluation (mode) applied to numerical forecasts from the 2005 nssl/spc spring program. *Weather and Forecasting*, **24 (5)**, 1252–1267, doi:10.1175/2009WAF2222241.1.

Doucet, A., N. Freitas, and N. Gordon, 2001: An introduction to sequential monte carlo methods. *Sequential Monte Carlo Methods in Practice. Springer, Berlin*, doi: 10.1007/978-1-4757-3437-9_1.

Dowell, D., A. Beck, B. Hu, T. Ladwig, K. Knopfmeier, P. Skinner, and D. Wheatley, 2016: Development of a high-resolution rapid refresh ensemble (hrrre) for severe weather forecasting. American Meteorological Society.

Dowell, D. C., and L. J. Wicker, 2009: Additive noise for storm-scale ensemble data assimilation. *Journal of Atmospheric and Oceanic Technology*, **26 (5)**, 911–927, doi: 10.1175/2008JTECHA1156.1.

Dowell, D. C., L. J. Wicker, and C. Snyder, 2011: Ensemble kalman filter assimilation of radar observations of the 8 may 2003 oklahoma city supercell: Influences of reflectivity observations on storm-scale analyses. *Monthly Weather Review*, **139 (1)**, 272–294, doi:10.1175/2010MWR3438.1.

Evensen, G., 1994: Sequential data assimilation with a nonlinear quasi-geostrophic model using monte carlo methods to forecast error statistics. *Journal of Geophysical Research: Oceans*, **99 (C5)**, 10 143–10 162, doi:10.1029/94JC00572.

Fujita, T., D. J. Stensrud, and D. C. Dowell, 2007: Surface data assimilation using an ensemble kalman filter approach with initial condition and model physics uncertainties. *Monthly Weather Review*, **135 (5)**, 1846–1868, doi:10.1175/MWR3391.1.

Gordon, N., D. Salmond, and A. Smith, 1993: Novel approach to nonlinear/non-gaussian bayesian state estimation. *IEE Proceedings F (Radar and Signal Processing)*, **140**, 107–113(6).

Hamill, T. M., J. S. Whitaker, M. Fiorino, and S. G. Benjamin, 2011: Global ensemble predictions of 2009's tropical cyclones initialized with an ensemble kalman filter. *Monthly Weather Review*, **139 (2)**, 668–688, doi:10.1175/2010MWR3456.1.

Houtekamer, P. L., and H. L. Mitchell, 1998: Data Assimilation Using an Ensemble Kalman Filter Technique. *Monthly Weather Review*, **126 (3)**, 796–811.

Houtekamer, P. L., H. L. Mitchell, G. Pellerin, M. Buehner, M. Charron, L. Spacek, and B. Hansen, 2005: Atmospheric data assimilation with an ensemble kalman filter: Results with real observations. *Monthly Weather Review*, **133 (3)**, 604–620, doi: 10.1175/MWR-2864.1.

Houtekamer, P. L., and F. Zhang, 2016: Review of the ensemble kalman filter for atmospheric data assimilation. *Monthly Weather Review*, **144 (12)**, 4489–4532, doi: 10.1175/MWR-D-15-0440.1.

Jazwinski, A., 1970: 9 approximate nonlinear filters. *Stochastic Processes and Filtering Theory*, A. H. Jazwinski, Ed., Mathematics in Science and Engineering, Vol. 64, Elsevier, 332 – 366, doi:https://doi.org/10.1016/S0076-5392(09)60378-7.

Johnson, A., and X. Wang, 2012: Verification and calibration of neighborhood and object-based probabilistic precipitation forecasts from a multimodel convection-allowing ensemble. *Monthly Weather Review*, **140 (9)**, 3054–3077, doi:10.1175/ MWR-D-11-00356.1.

Jones, T. A., K. Knopfmeier, D. Wheatley, G. Creager, P. Minnis, and R. Palikonda, 2016: Storm-scale data assimilation and ensemble forecasting with the nssl experimental warn-on-forecast system. part ii: Combined radar and satellite data experiments. *Weather and Forecasting*, **31 (1)**, 297–327, doi:10.1175/WAF-D-15-0107.1.

Jones, T. A., D. Stensrud, L. Wicker, P. Minnis, and R. Palikonda, 2015: Simultaneous radar and satellite data storm-scale assimilation using an ensemble kalman filter approach for 24 may 2011. *Monthly Weather Review*, **143 (1)**, 165–194, doi:10. 1175/MWR-D-14-00180.1.

Jung, Y., G. Zhang, and M. Xue, 2008: Assimilation of simulated polarimetric radar data for a convective storm using the ensemble kalman filter. part i: Observation operators for reflectivity and polarimetric variables. *Monthly Weather Review*, **136 (6)**, 2228–2245, doi:10.1175/2007MWR2083.1.

Kalman, R. E., 1960: A New Approach to Linear Filtering and Prediction Problems. *Journal of Basic Engineering*, **82 (1)**, 35–45.

Kalman, R. E., and R. S. Bucy, 1961: New Results in Linear Filtering and Prediction Theory. *Journal of Basic Engineering*, **83 (1)**, 95–108.

Kalnay, E., 2003: Atmospheric modelling, data assimilation and predictability. by eugenia kalnay. cambridge university press. 2003. pp. xxii + 341. isbns 0 521 79179 0, 0 521 79629 6. *Quarterly Journal of the Royal Meteorological Society*, **129 (592)**, 2442–2442, doi:10.1256/00359000360683511.

Lakshmanan, V., T. Smith, G. Stumpf, and K. Hondl, 2007: The warning decision support system–integrated information. *Weather and Forecasting*, **22 (3)**, 596–612, doi:10.1175/WAF1009.1.

Lorenc, A. C., 2003: The potential of the ensemble kalman filter for nwp—a comparison with 4d-var. *Quarterly Journal of the Royal Meteorological Society*, **129 (595)**, 3183–3203, doi:10.1256/qj.02.132.

Lorenz, E., 1995: Predictability: a problem partly solved. *Seminar on Predictability, 4-8 September 1995*, ECMWF, Shinfield Park, Reading, ECMWF, Vol. 1, 1-18, URL https://www.ecmwf.int/node/10829.

Mansell, E. R., C. L. Ziegler, and E. C. Bruning, 2010: Simulated electrification of a small thunderstorm with two-moment bulk microphysics. *Journal of the Atmospheric Sciences*, **67 (1)**, 171–194, doi:10.1175/2009JAS2965.1.

Maybeck, P., 1979: *Stochastic Models, Estimation and Control*, Vol. 1. Academic Press.

McGinnis, S., D. Nychka, and L. Mearns, 2015: *A New Distribution Mapping Technique for Climate Model Bias Correction*, 91–99. doi:10.1007/978-3-319-17220-0_9.

Miller, M. L., V. Lakshmanan, and T. M. Smith, 2013: An automated method for depicting mesocyclone paths and intensities. *Weather and Forecasting*, **28 (3)**, 570–585, doi:10.1175/WAF-D-12-00065.1.

Miyoshi, T., K. Kondo, and T. Imamura, 2014: The 10,240-member ensemble kalman filtering with an intermediate agcm. *Geophysical Research Letters*, **41 (14)**, 5264–5271, doi:10.1002/2014GL060863.

Miyoshi, T., and M. Kunii, 2012: Using airs retrievals in the wrf-letkf system to improve regional numerical weather prediction. *Tellus A: Dynamic Meteorology and Oceanography*, **64 (1)**, 18 408, doi:10.3402/tellusa.v64i0.18408.

Pan, S., 2017: Simultaneous assimilation of radar and satellite data for convective scale nwp using hybrid ensemble variational data assimilation approach. M.S. thesis, University of Oklahoma.

Poterjoy, J., 2016: A localized particle filter for high-dimensional nonlinear systems. *Monthly Weather Review*, **144 (1)**, 59–76, doi:10.1175/MWR-D-15-0163.1.

Poterjoy, J., R. A. Sobash, and J. L. Anderson, 2017: Convective-scale data assimilation for the weather research and forecasting model using the local particle filter. *Monthly Weather Review*, **145 (5)**, 1897–1918, doi:10.1175/MWR-D-16-0298.1.

Poterjoy, J., L. Wicker, and M. Buehner, 2019: Progress toward the application of a localized particle filter for numerical weather prediction. *Monthly Weather Review*, **147 (4)**, 1107–1126, doi:10.1175/MWR-D-17-0344.1.

Roebber, P. J., 2009: Visualizing multiple measures of forecast quality. *Weather and Forecasting*, **24 (2)**, 601–608, doi:10.1175/2008WAF2222159.1.

Skinner, P. S., and Coauthors, 2018: Object-based verification of a prototype warn-on-forecast system. *Weather and Forecasting*, **33 (5)**, 1225–1250, doi:10.1175/WAF-D-18-0020.1.

Snook, N., M. Xue, and Y. Jung, 2015: Multiscale enkf assimilation of radar and conventional observations and ensemble forecasting for a tornadic mesoscale convective system. *Monthly Weather Review*, **143 (4)**, 1035–1057, doi:10.1175/MWR-D-13-00262.1.

Snyder, C., T. Bengtsson, P. Bickel, and J. Anderson, 2008: Obstacles to high-dimensional particle filtering. *Monthly Weather Review*, **136 (12)**, 4629–4640, doi:10.1175/2008MWR2529.1.

Snyder, C., and F. Zhang, 2003: Assimilation of simulated doppler radar observations with an ensemble kalman filter. *Monthly Weather Review*, **131 (8)**, 1663–1677, doi:10.1175//2555.1.

Sobash, R. A., and D. J. Stensrud, 2015: Assimilating surface mesonet observations with the enkf to improve ensemble forecasts of convection initiation on 29 may 2012. *Monthly Weather Review*, **143 (9)**, 3700–3725, doi:10.1175/MWR-D-14-00126.1.

Stensrud, D., and Coauthors, 2013: Progress and challenges with warn-on-forecast. *Atmospheric Research*, **123**, 2–16, doi:10.1016/j.atmosres.2012.04.004.

Stensrud, D. J., and Coauthors, 2009: Convective-scale warn-on-forecast system. *Bulletin of the American Meteorological Society*, **90 (10)**, 1487–1500, doi:10.1175/2009BAMS2795.1.

Theis, S. E., A. Hense, and U. Damrath, 2005: Probabilistic precipitation forecasts from a deterministic model: a pragmatic approach. *Meteorological Applications*, **12 (3)**, 257–268, doi:10.1017/S1350482705001763.

Tong, M., 2006: Ensemble kalman filter assimilation of doppler radar data for the initialization and prediction of convective storms. Ph.D. thesis, University of Oklahoma.

Trapp, R. J., G. J. Stumpf, and K. L. Manross, 2005: A reassessment of the percentage of tornadic mesocyclones. *Weather and Forecasting*, **20 (4)**, 680–687, doi:10.1175/WAF864.1.

van Leeuwen, P. J., 2009: Particle filtering in geophysical systems. *Monthly Weather Review*, **137 (12)**, 4089–4114, doi:10.1175/2009MWR2835.1.

Wang, B., X. Zou, and J. Zhu, 2000: Data assimilation and its applications. **97 (21)**, 11 143–11 144, doi:10.1073/pnas.97.21.11143.

Wheatley, D. M., K. H. Knopfmeier, T. A. Jones, and G. J. Creager, 2015: Storm-scale data assimilation and ensemble forecasting with the nssl experimental warn-on-forecast system. part i: Radar data experiments. *Weather and Forecasting*, **30 (6)**, 1795–1817, doi:10.1175/WAF-D-15-0043.1.

Whitaker, J. S., and T. M. Hamill, 2002: Ensemble data assimilation without perturbed observations. *Monthly Weather Review*, **130 (7)**, 1913–1924, doi:10.1175/1520-0493(2002)130⟨1913:EDAWPO⟩2.0.CO;2.

Whitaker, J. S., T. M. Hamill, X. Wei, Y. Song, and Z. Toth, 2008: Ensemble data assimilation with the ncep global forecast system. *Monthly Weather Review*, **136 (2)**, 463–482, doi:10.1175/2007MWR2018.1.

Wu, W.-S., R. J. Purser, and D. F. Parrish, 2002: Three-dimensional variational analysis with spatially inhomogeneous covariances. *Monthly Weather Review*, **130 (12)**, 2905–2916, doi:10.1175/1520-0493(2002)130⟨2905:TDVAWS⟩2.0.CO;2.

Yi, S.-R., and J. Song, 2018: Particle filter based monitoring and prediction of spatiotemporal corrosion using successive measurements of structural responses. *Sensors (Basel)*, doi:10.3390/s18113909.

Yussouf, N., D. C. Dowell, L. J. Wicker, K. H. Knopfmeier, and D. M. Wheatley, 2015: Storm-scale data assimilation and ensemble forecasts for the 27 april 2011 severe weather outbreak in alabama. *Monthly Weather Review*, **143 (8)**, 3044–3066, doi:10.1175/MWR-D-14-00268.1.

Yussouf, N., E. R. Mansell, L. J. Wicker, D. M. Wheatley, and D. J. Stensrud, 2013: The ensemble kalman filter analyses and forecasts of the 8 may 2003 oklahoma city tornadic supercell storm using single- and double-moment microphysics schemes. *Monthly Weather Review*, **141 (10)**, 3388–3412, doi:10.1175/MWR-D-12-00237.1.

Zhang, F., C. Snyder, and J. Sun, 2004: Impacts of initial estimate and observation availability on convective-scale data assimilation with an ensemble kalman filter. *Monthly Weather Review*, **132 (5)**, 1238–1253, doi:10.1175/1520-0493(2004)132⟨1238:IOIEAO⟩2.0.CO;2.

Zhang, F., Y. Weng, J. A. Sippel, Z. Meng, and C. H. Bishop, 2009: Cloud-resolving hurricane initialization and prediction through assimilation of doppler radar observations with an ensemble kalman filter. *Monthly Weather Review*, **137 (7)**, 2105–2125, doi:10.1175/2009MWR2645.1.

Zhang, Y., F. Zhang, and D. J. Stensrud, 2018: Assimilating all-sky infrared radiances from goes-16 abi using an ensemble kalman filter for convection-allowing severe thunderstorms prediction. *Monthly Weather Review*, **146 (10)**, 3363–3381, doi:10.1175/MWR-D-18-0062.1.